Using light and electron microscopy to understand the replication of aphthoviruses

Pui Yiu Audrey Lai

Green Templeton College
Nuffield department of Clinical Medicine
Division of Structural Biology
University of Oxford

A thesis submitted for the degree of *Doctor of Philosophy*

Hilary term 2023

Acknowledgement

I would like to thank all my supervisors for their support. I am grateful to my supervisors across the three sites, Daniel Clare, Dave Stuart and Toby Tuthill, for their inimitable support and insights. Toby and Dave have always been extremely positive and provide constructive guidance to help my project in moving forward. I joined this project with no experience in microscopy and Dan has been extremely patient and supportive providing me with the knowledge to help me build up my foundation. I was fortunate to have been further supported by Liz Fry, Stephen Berryman, Pippa Hawes and Pranav Shah, who have guided me throughout my PhD and provided me with the basics skills and techniques to become a researcher. My project was joined across three sites, so I, firstly, would like to thank all the past and present members of the Picornavirus Structural group at the Pirbright Institute. Beamline-24 (B24) at Diamond Light Source and the eBIC team, especially Archana Jadhav, Maria Harkiolaki, James Gilchrist and Matt Spink. I could not have made much progress in microscopy work without their support through COVID-19. I had been extremely lucky to complete this project as it is the best project I could have ever imagined. It had also been a great pleasure to work with you all.

This project was supported by Diamond Light Source (proposals nt26538, nr21005 and bi27932), the Division of Structural Biology (STRUBI) in the Nuffield

Department of Clinical Medicine (NDM), the Doctoral Training Programme in the Mathematical, Physical, Life Sciences Division and the Pirbright Institute.

I would like to thank all my friends, especially Kim, Andrew, Chen, John and my cousin Carpio. Thank you for getting me through the ups and down over the past few years. Thank you for being so patient and welcoming a chat whenever I needed it. Thank you for having faith in me and encouraging me over the past years. And of course, other friends that I met throughout my DPhil, Connor, Sana, Yana, Shanzhi and Liangti could not be left out. Thank you all for your love and support.

Finally, I would like to thank my family. Firstly, my parents, Charles and Dorothy, they have given me the freedom to study the subject I like and pursue a career of my own will. My little brother, Bernard, is the gentlest boy in our family and has always been supportive and listened to me whenever I suffer. Thank you to all my other family members but a special thank you to my grandpa, Fuk Hong Lai. He is one of the greatest men I have seen and dedicated his life to his work for the family. The thesis is, therefore, dedicated to the loving memory of my grandpa (1930-2022) who has taught me love and kindness, courage and wisdom in life.

Impact of COVID-19

During the COVID-19 pandemic, laboratory access was restricted between 2020 to 2021 and suspended, between March and June 2020, in support of COVID-19 projects and distancing regulations. To comply with social distancing restrictions in laboratories, we were running experiments and access to laboratories on shift-based access from July 2020 until March 2021. In addition to that, we experience a second lockdown in November 2020 which further affected our progress. The first suspension of laboratory work in 2020 delayed our schedule to complete work at the Pirbright Institute and the transition of our work from Pirbright to the Diamond Light Source. I had limited access to the laboratory, and to fulfil social distancing requirements, our conventional TEM and cryo-EM training was affected. Moreover, I missed time from work due to self-isolations: (i) in April 2021 as my housemate was infected with COVID-19 resulting in our house lockdown at Oxford which I had to cancel my microscopy sessions at the Diamond Light Source and (ii) in December 2022 when I tested positive for COVID-19 which affected progress in data analysis. Access to microscopes was made difficult as there was a backlog of projects due to COVID-19.

Meanwhile, I was able to mitigate the impact by carrying out data analysis and reading literature. However, due to the significant laboratory time being lost, as my research project is laboratory-based, the scope of my project was significantly affected, especially with respect to electron microscopy work. Hence, a funding extension was sought and approved by Oxford’s COVID-19 Scholarship Extension Fund. Additionally, a thesis submission deadline was subsequently sought and approved.

Declaration of Work

I hereby declare that the work described in this thesis is my own, except as described below.

Chapter 3: GFP1-10 cell line was developed by Dr Joseph Newman and Connor Haywards at the Pirbright Institute. Sequencing of plasmids and viruses was performed by the bioinformatics and sequencing team at the Pirbright Institute.

Chapter 4: Electron microscopy sample preparation, specifically the cutting of resin blocks and staining, was completed in conjunction with the Bioimaging team at The Pirbright Institute. Data from high pressure frozen work was kindly provided by Prof Pippa Hawes at the Pirbright Institute.

Chapter 5: Plaque assay measuring ERAV titre was performed in conjunction with Dr Stephen Berryman and Dr James Kelly at the Pirbright Institute. ERAV virus stock was kindly prepared and aliquoted by Dr Joseph Newman and Dr Amina Yasmin at the Pirbright Institute.

Pui Yiu Audrey Lai
Green Templeton College,
University of Oxford

Abstract

Aphthovirus is a genus of the family *Picornaviridae* which includes Foot-and-mouth-disease virus (FMDV) and Equine rhinitis A virus (ERAV). FMDV is a highly contagious pathogen infecting cloven-hoofed animals and is hence economically important. FMDV replication takes place in the cytoplasm and induces massive rearrangement of the host cell membranes to facilitate virus replication. Rearranged membranes form structures providing the site of viral genome replication known as the replication organelle (RO). The understanding of the RO, viral proteins and site of virus assembly is not well established. This project applies various microscopy approaches to investigate details of *aphthovirus* replication in cells.

FMDV 3A protein is known to play a key role in viral replication machinery. We generated recombinant viruses of FMDV with various tags fused to this protein, subsequently allowing 3A to be detected in confocal microscopy. We developed a split-GFP system to study the dynamics of 3A protein *in vitro*. We showed that 3A signals appeared contiguous to the Golgi membrane signals suggesting that it potentially serve as a main source of membrane associated with viral replication. This approach was taken with the aim of facilitating the development of a correlative light electron microscopy (CLEM) system to unravel the localisation of virus proteins and their link to RO in cells. ERAV was used as a surrogate model to study FMDV replication in a lower containment laboratory using cryo-electron tomography (cryo-ET). Virus particles were observed associated with membrane structures with single membrane vesicles being more predominant than double membrane vesicles in infected cells. By sub-tomogram averaging, we reconstructed 3-dimensional (3D) models of intracellular ERAV full and empty particles which were compared with structures obtained for the virus purified from tissue culture and crystallized. Additional density was identified in the ERAV empty particles potentially corresponding to RNA contact sites inside the capsid.

Table of Contents

CHAPTER 4 ULTRASTRUCTURAL REARRANGEMENT IN FMDV AND ERAV ARE COMPARABLE

List of Figures

List of tables

Abbreviations

Å	Angstrom
°C	Degrees Celsius
µ	Micro
µL	Microlitre
µg	Microgram
µg/µL	Micrograms per microlitre
µm	Micrometre
Δ	Deletion
≤	Less than or equal to
2D	2-dimensional
$3C^{pro}$	3C protease
3D	3-dimensional
$3D^{pol}$	3D polyerase
BEV	Bovine enterovirus
BfA	Brefeldin A
BHK	Baby hamster kidney cells
CEMOVIS	Cryo-electro-microscopy of vitreous sections
CLEM	Correlative light-electron microscopy
COP	Coat protein complex
CPE	Cytopathic effect
cre	Cis-acting element
Cryo-EM	Cryo-electron microscopy

Cryo-ET	Cryo-electron tomography
CryoFIB	Cryo-focused-ion-beam
CryoFIB/SEM	Cryo-focused-ion-beam/scanning electron microscope
Cryo-SXT	Cryo-soft-X-ray-tomography
CTF	Contrast Transfer function
CVB3	Coxsackie B3
DAB	Diaminobenzidine
DDX	DEAD-box RNA helicases
DMV	Double membrane vesicle
DNA	Deoxyribonucleic acid
ER	Endoplasmic reticulum
ERAV	Equine rhinitis A virus
FBS	Foetal bovine serum
FMD	Foot-and-mouth disease
FMDV	Foot-and-mouth disease virus
GA	Glutaraldehyde
GFP	Green fluorescent protein
HA	Haemagglutinin
HCV	Hepatitis C virus
HEPES	N-2-hydroxyethylpiperazin-N’-2-ethanesulfonic acid
h	Hours
HA	Haemagglutinin

hpi	Hours post infection
HS	Heparan sulfate
IBV	Infectious bronchitis cirus
IgG	Immunoglobulin G
IRES	Internal ribosome entry site
IRF3	Interferon regulatory factor 3
k (prefix)	Kilo
kb	Kilobase
L	Litre
L^{pro}	Leader protease
LB	Luria-bertani
LC3	Microtubule-associated protein 1A/1B light chain 3
LD	Lipid droplets
LM	Light microscopy
M	Molar
MERS-CoV	Middle East Respiratory Syndrome coronavirus
m (prefix)	Milli
mg	Milligram
mg/mL	Milligram per millilitre
mm	Millimetre
mM	Millimolar
MOI	Multiplicity of infection
n (prefix)	Nano

ng	Nanogram
ng/mL	Nanogram per millilitre
nm	Nanometre
NSP or nsp	Non-structural protein
nt	Nucleotide
PBS	Phosphate buffered saline
PCR	Polymerase chain reaction
PFA	Paraformaldehyde
PFU	Plaque forming units
PFU/mL	Plaque forming units per millilitre
pi	Post infection
PI4P	Phosphatidylinositol 4-phosphate
PI4KIIIβ	Host type III phosphatidylinositol 4-phosphate β
PV	Poliovirus
RNA	Ribonucleic acid
RO	Replication organelle
SARS-CoV	Severe Acute Respiratory syndrome coronavirus
SAT	South African Territories
SMV	Single membrane vesicle
S.O.C.	Super optimal broth with catabolite repression
SPA	Single particle analysis
STA	Sub-tomogram averaging
TC	Tetracysteine

TEM	Transmission electron microscopy
U	Unit
ULK	Unc-51 like autophagy kinase
UK	United Kingdom
UTR	Untranslated region
VGM	Virus growth media
VPg	Viral protein genome linked
vRNA	Viral RNA
WT	Wildtype

Chapter 1 Introduction

1.1. Disease

Foot-and-mouth disease (FMD) is an economically important disease that affects the livestock industry. It is highly contagious and affects cloven-hoofed animals with varying morbidity and mortality (Brooksby, 1982). The incubation period is between 2 – 14 days. Clinical symptoms of the disease include high fever (pyrexia), lost in appetite (anorexia), reduction in milk production and vesicular lesions found on feet, mouth, nose, and teats. In young animals, it can also affect cardiac muscles as well hence mortality is higher (Brooksby, 1982; Grubman and Baxt, 2004). The pathogen, foot-and-mouth disease virus (FMDV), causing the disease is classified into seven serotypes: A, O, C, Asia-1, South African Territories (SAT)-1, SAT-2, and SAT-3.

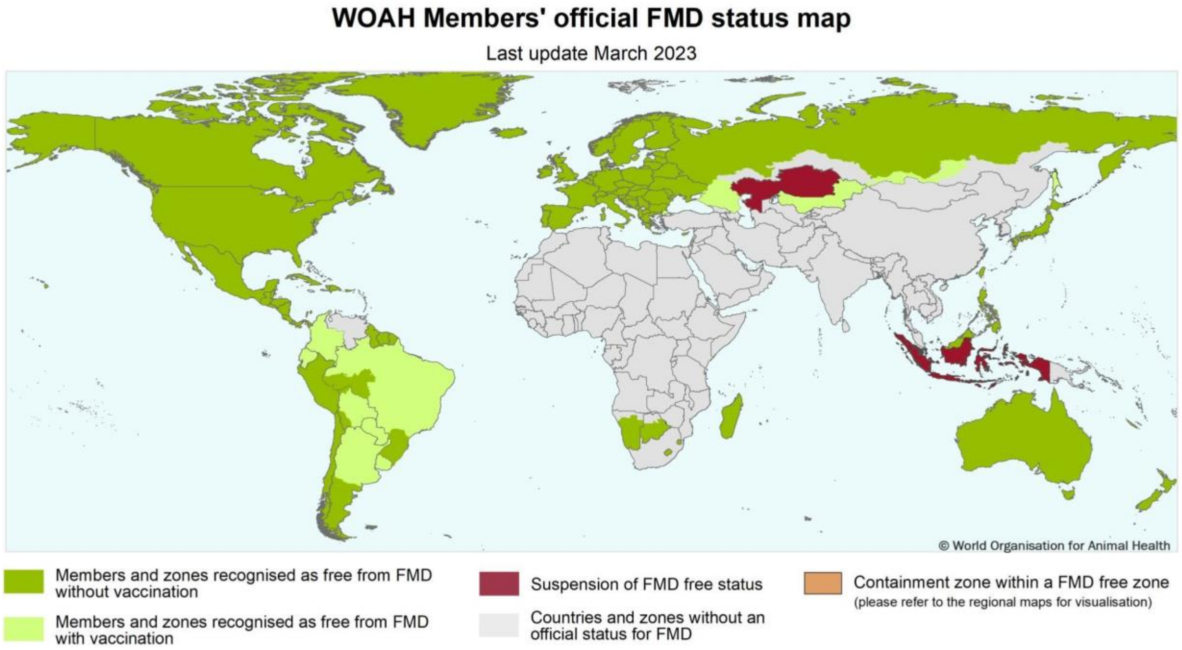

Figure 1.1: Map of global FMD status in 2023.

(Source from Foot and mouth disease - WOAH - World Organisation for Animal Health, no date)

The United Kingdom is classified as an FMD-free country, the most recent outbreak in 2001 caused the industry to lose £3.1 billion and approximately 10 million animals were culled. While the UK is considered FMD-free, Africa, Asia, the Middle East, and South America are considered as FMD endemic countries. Recognition of FMD-free status is managed by the World Organisation for Animal Health (WOAH, founded as OIE), which as a global intergovernmental organisation that is responsible for improving animal health and welfare (*WOAH - World Organisation for Animal Health*, no date). FMD-free countries are recognised under two categories: FMD-free status where vaccination is practiced, countries such as Brazil and Turkey are currently under this status (‘Recognition of the Foot and Mouth Disease Status of Members’, 2020). Another category is FMD-free status where vaccination is not practiced, such as Australia, Japan and New Zealand (‘Recognition of the Foot and Mouth Disease Status of Members’, 2020). In the case of an outbreak in an FMD-free country, the disease status would be immediately suspended, and export of livestock would be severely affected. The use of vaccination may induce immunological pressure leading to the development of a new variant (Belsham, 2020). Moreover, current available vaccines are inactivated virus, serotype-specific and only provide short-lived immunity (Golde *et al.*, 2005; Rodriguez and Grubman, 2009; Parida, 2014; Mahapatra and Parida, 2018). Hence, it is difficult to control and eradicate the disease.

1.2. Picornavirus Classification

The *Picornaviridae* is a large family of +ve strand RNA viruses that infect both human and animals (Figure 1.2). For example, enteroviruses are most well-known for carrying disease in humans and FMDV causes disease in several species of livestock.

Picornaviruses are non-enveloped and consist of an icosahedral capsid of ~30 nm in diameter. The capsid contains a single stranded, positive-sense RNA. The viral genome possesses a small virally encoded protein called viral protein genome linked (VPg) that is covalently linked to the 5’ end of the genome. The genome is approximately 8.4kb in length and serves as the mRNA to generate a polyprotein which is cleaved to form structural proteins and non-structural proteins (NSPs), the precursors for capsids and viral proteins respectively.

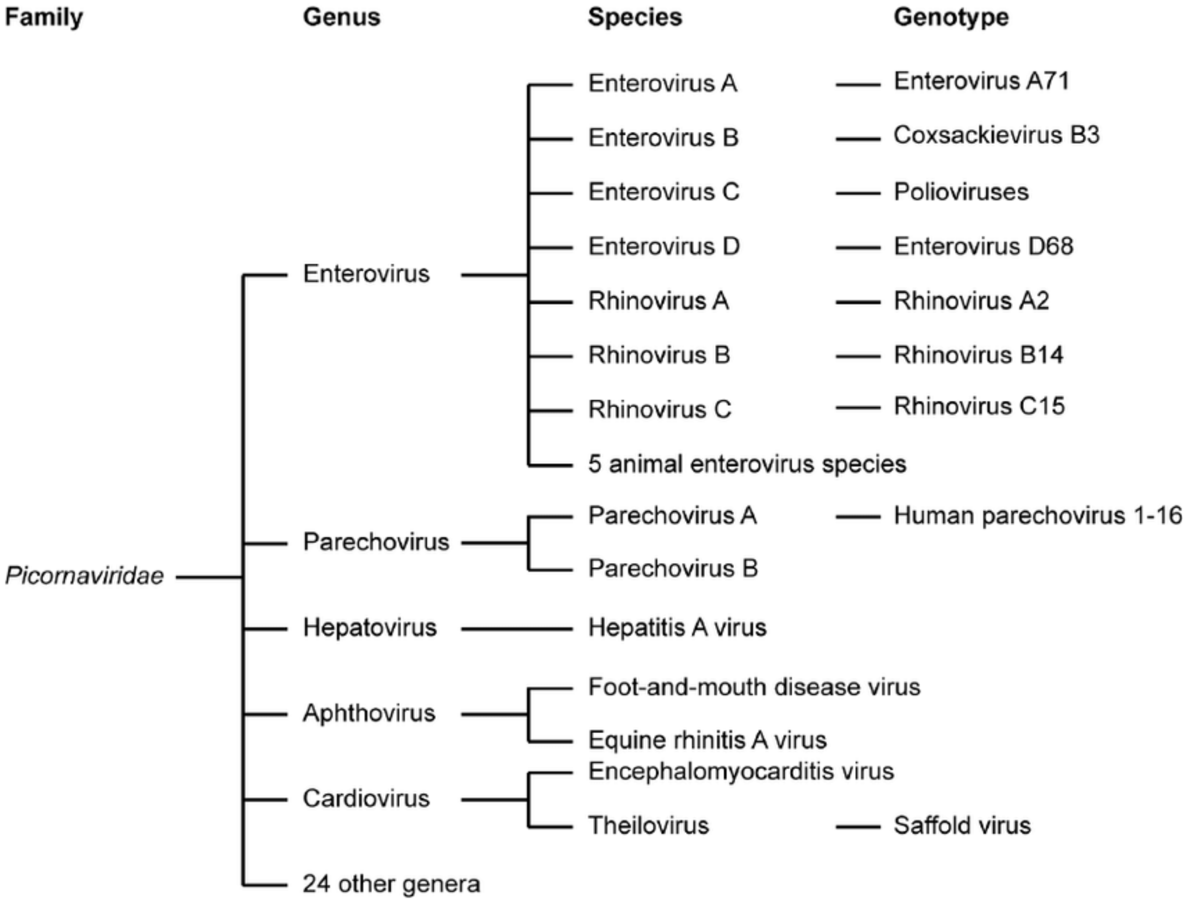

Figure 1.2: Classification of picornaviruses.

Clinically important picornaviruses are outlined in this classification of the virus family *Picornaviridae*. Figure adapted from (van der Linden, Wolthers and van Kuppeveld, 2015).

1.3. Aphthoviruses

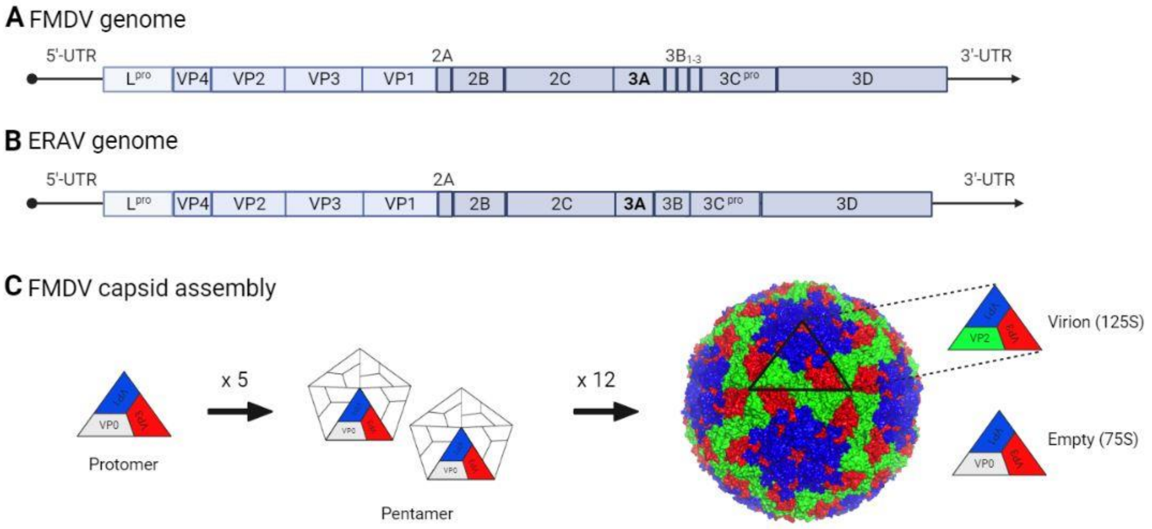

Figure 1.3: Genome organisation of FMDV and ERAV and schematic of FMDV capsid assembly.

Panel **A** and **B** are schematics of the genome organisation of FMDV and ERAV respectively. FMDV encodes 3 copies of 3B whilst ERAV only has one copy. **(C)** Represents a schematic of FMDV capsid assembly. VP0 (grey), VP1 (blue) and VP3 (red) form a protomer. 5 protomers then assemble to form a pentamers. 12 of these pentameric subunits then assemble to form a capsid. Virions are made up of 240 protein chains while the empty particle is formed of 180 protein chains since VP0 is cleaved into VP2 (green) and VP4 (internal) once RNA is packaged whilst VP0 remains uncleaved in the empty particle. (The FMDV virion is adapted from Malik et al., 2017. Created with Biorender.com).

Aphthovirus, a genus of the family *Picornaviridae*, infects several species of animals including horses and cloven-hoofed animals. Members of this genus are

FMDV, equine rhinitis A virus (ERAV), bovine rhinitis A virus (BRAV) and bovine rhinitis B virus (BRBV). In our study, we will be focusing on FMDV and ERAV. They share a similar structure and organisation of the genome (Stanway, 1990; Wutz *et al.*, 1996) (Figure 1.3A and B).

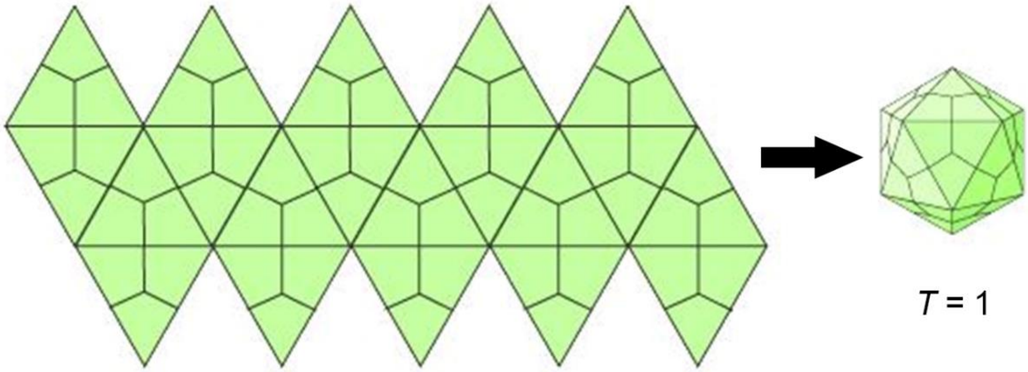

Figure 1.4 Schematic of virus symmetry from Caspar-Klug theory.

A T=1 model to build up an icosahedral capsid. A T=1 lattice is shown on the left-hand side comprising 20 triangles arranged on the same lattice sheet. These 20 triangles are formed from 60 identical capsid proteins which assemble into the T=1 capsid model next to the lattice. Figure taken from EXPASY, 2023.

The FMDV capsid comprises VP1-4; while VP1, VP2 and VP3 are exposed externally, VP4 is internal (Figure 1.3C). Atomic resolution structures of the FMDV capsid were first revealed by X-ray crystallography in 1989 (Acharya *et al.*, 1989). VP1, VP2 and VP3 each adopt an eight-stranded β-barrel. A major antigenic site of FMDV is found in the flexible GH loop, residues 140 to 160 of VP1 (Acharya *et al.*, 1989; Logan *et al.*, 1993; Han, Guo and Sun, 2015). Like other picornaviruses, the aphthovirus capsid is icosahedral showing a pseudo T=3 or P=3 arrangement. Icosahedral symmetry of viruses is classified by the Triangulation (T)-number based on the quasi-equivalence symmetry, and this theory originates from Caspar and Klug (Caspar and Klug, 1962). The T-number is defined by the formula: $T = h^2 + h.k + k^2$, where *h* and k are integers corresponding to the structure of the surface lattice, essentially related to the number of intervening pseudo 6-fold axes between adjacent 5-folds (Figure 1.4). In general, icosahedral capsid comprises of 60*T* asymmetric units, as it is arranged so that the pentamer sits on the vertex of the five-fold axis. In addition to the pentameric units, another morphological unit composes of six subunits arranged in a hexamer is also generated on the icosahedral lattice. An icosahedral capsid always contains 12 pentamers and in addition to that, according to the theory, $10(T-1)$ hexameric units are generated consequently. The 20 icosahedral faces and 30 edges on the capsid structure are delineated by the three-fold and two-fold respectively. The icosahedral asymmetric unit of FMDV comprises three similar viral proteins (VP1-3), arranged in a pseudo-T=3 arrangement.

1.4. FMDV Genome organisation

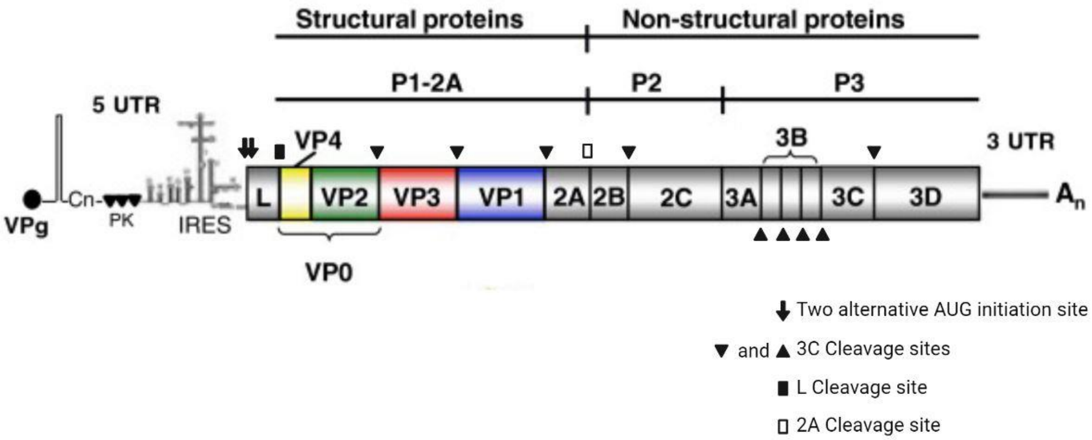

Figure 1.5 FMDV genome organisation and cleavage sites.

Figure adapted from Jamal and Belsham, 2013.

The FMDV genome is approximately ~8400nt in size and enclosed within the icosahedral proteinaceous capsid; it comprises three main elements, the 5' untranslated region (UTR), open reading frame (ORF) and the 3'UTR followed by the poly(A) tail attached at the end of the genome (Figure 1.5). The structural proteins VP1-4 are encoded by the N-terminal third of the ORF and ultimately assembly to form the capsid. The non-structural proteins are encoded in the C-terminal two thirds of the ORF, and they play an important role in different aspects of viral replication: 2B and 2C, together with their precursor 2BC, promote cellular membrane rearrangements required for replication. 3A plays a role in the recruitment of the viral replication machinery to these rearranged membranes while the three tandem 3B (VPg) copies act as primers for new RNA synthesis. The viral

3C protease ($3C^{pro}$) is involved in polyprotein processing while the RNA-dependent RNA synthesis of the new genome is mediated by the 3D polymerase ($3D^{pol}$).

1.4.1. The 5'UTR

The 5' UTR is 1300 bases in length and consists of elements involved in translation and replication. The main elements are the S-fragment (Clarke *et al.*, 1987), the poly(C) tract (Mellor, Brown and Harris, 1985) and pseudoknots, the *cis*-acting replication element (*cre*) and the internal ribosome entry site (IRES) (Belsham, 2015). These have been shown to play a role in viral translation and replication.

1.4.1.1. The S-fragment

The S-fragment is approximately 360 bases long and folds into an unusually large stem-loop structure (Newton *et al.*, 1985) and contributes to viral genome stability and replication (Kloc *et al.*, 2017). It is a highly base-paired structure and is thought to protect the viral RNA from host exonuclease digestion (Mason, Grubman and Baxt, 2003). It has been shown that the S fragment is vital for virus viability, although a small deletion in the upper S fragment can be tolerated to an extent (Kloc *et al.*, 2017). S-fragment deletions occur naturally and are isolated in O, C and A serotypes, and it was suggested that the length of the S fragment is closely related to the attenuation of infectivity and modulation of the innate immune response (Kloc *et al.*, 2017). The S fragment also interacts with proteins including host proteins (Serrano *et al.*, 2006) and the viral 3C protease (Lawrence and Rieder, 2009). Furthermore, RNA helicase A which plays a role in regulating some essential cellular processes such as transcription (Hong *et al.*, 2018) and translation (Singh *et al.*, 2020), plays a role in FMDV replication, as they were found to localised near viral 2C and 3A during viral replication. Both viral proteins are associated with assembly of replication complexes (Lawrence and Rieder, 2009) and interact with S-fragment (Lawrence and Rieder, 2009).

1.4.1.2. Poly(C) Tract and Pseudoknots (PKs)

Following the S-fragment is the polycytidine (poly(C)) tract of variable length between 150-200 bases. It is identified in aphthoviruses and cardioviruses within the picornavirus family (Brown et al., 1974; Mellor, Brown and Harris, 1985; Wutz et al., 1996). The poly(C) tract is located within the first 500nt of the 5'UTR. It has been suggested that the length of poly(C) tract is linked to genetic stability as long poly(C) tract favours a successful infection (Harris and Brown, 1977; Rieder et al., 1993; also reviewed in Penza, Russell and Schulze, 2021)**.**

At the end of the poly(C) tract follow the pseudoknots (PKs) which comprises two to four tandem repeats containing stem loop structure (Clarke *et al.*, 1987). However, the exact function of PKs is yet to be fully understood, it is believed they play a role in the virulence and pathogenicity of FMDV; deletions in this region attenuates FMDV infection in bovine cells and cattle but infection in pigs is unaffected (Zhu *et al.*, 2019). A recent study of the link between PKs and viral RNA replication revealed that the repeated copies of PKs are crucial for infectious virus production (Ward *et al.*, 2022).

1.4.1.3. Cis-acting Replication Element (*cre*)

The cis-acting replication element (*cre*), sometimes also referred to as the 3B uridylylation signal (*bus*) is a highly conserved region of 55 nucleotides in a stem-loop structure. The location of this structure varies between picornaviruses, for example it is located downstream of the PKs within the 5' UTR in FMDV (Mason, S. V. Bezborodova and Henry, 2002) but is located in the P1 region in human rhinivirus (HRV) (Mcknight and Lemon, 1998) and 2C in poliovirus (PV) (Goodfellow *et al.*, 2000).

The highly conserved "AAACA" motif is essential for viral genome replication; it serves as a template for VPg (3B) uridylylation by FMDV 3D polymerase, and the product generated is VPgpU(pU), which serves as a primer that initiates viral RNA synthesis (Mason, S. v. Bezborodova and Henry, 2002). Interestingly, replication of the virus is not affected by the location of *cre* (Mason, S. V. Bezborodova and Henry, 2002).

1.4.1.4. Internal Ribosome Entry Site (IRES)

Finally, the IRES is a highly structured region composed of five domains and multiple stem-loops of length around 450 bases downstream of *cre* (Pilipenko *et al.*, 1989). This structure is capable of recruiting ribosomes to initiate cap-independent translation of viral RNA, allowing translation of viral RNA to continue following virus-induced shut down of cap-dependent translation (Pilipenko *et al.*, 1989; Lozano and Martínez-Salas, 2015).

1.4.2. The virus-encoded polyprotein

The virus-encoded polyprotein is expressed as a single open reading frame (ORF) that is comprised of the following: the Leader protease (L^{pro}); P1 precursor proteins encoding the three structural protein precursors VP0 to VP3; and ten non-structural proteins encoded in the P2 and P3 region. These proteins are 2A, 2B, 2C, 3A, three tandem copies of 3B ($3B_{1-3}$), 3C protease ($3C^{pro}$) and 3D polymerase ($3D^{pol}$). $3C^{pro}$ is responsible for all cleavage events except the following three: L^{pro} auto-cleaves itself from the polyprotein, 2A is cleaved from the polyprotein through a ribosomal skipping mechanism and lastly, VP4 and VP2 exist initially as a precursor called VP0 which is cleaved by a proposed autocatalytic mechanism (Curry *et al.*, 1995) to form individual proteins upon capsid assembly and RNA packaging.

1.4.2.1. Leader (L) protease

L^{pro} is a papain-like protease that self-cleaves from the translating polyprotein. The L^{pro} encoding sequence contains two initiation AUG codons and two versions of the protein, L_{ab} and L_b are produced which is dependent on the AUG codons used (Sangar *et al.*, 1987). It is capable of rapidly degrading host translation initiation factor eIF4G which in turn inhibits cap-dependent host translation, allowing the cellular translation machinery to be used exclusively for viral translation.

1.4.2.2. 2A

FMDV 2A is an 18 amino acid peptide which induces a ribosomal skipping mechanism during translation that cleaves between the C-terminus of 2A and the N-terminus of the 2B region (Donnelly, Hughes, *et al.*, 2001; Donnelly, Luke, *et al.*, 2001).

1.4.2.3. 2B and 2C

FMDV causes rearrangement in cellular membranes (this will be explained in more detail in section 1.6). 2B is a viroporin which means it is a hydrophobic transmembrane protein. It can therefore create a pore in cellular membranes such as endoplasmic reticulum (ER) and Golgi membranes, enabling the traffic of small molecules through the membranes (Gladue *et al.*, 2018). It also regulates calcium homeostasis in cells; the presence of 2B increases the permeability of membranes and thus autophagy is induced in cells due to the increase in calcium content (Ao *et al.*, 2015), this eventually regulates apoptosis of infected cells (Aldabe, Irurzun and Carrasco, 1997; Campanella *et al.*, 2004).

FMDV precursor 2BC is capable of blocking the ER-to-Golgi pathway Moffat et al., 2005a). In infected cells, 2B has been shown to colocalise in ER and can insert itself into the membrane of ER (Ao *et al.*, 2015).

2C is a hexameric (Sweeney *et al.*, 2010), membrane-binding protein of the RO (Moffat *et al.*, 2007). It potentially plays a role helicase activity (Mahajan *et al.*, 2013), as it contains an ATPase domain that belongs to superfamily-3 helicases of the AAA+ family (Sweeney *et al.*, 2010). 2C was previously shown to co-localise with an autophagy marker, LC3 (O'Donnell *et al.*, 2011). It also binds to an autophagy regulator, Beclin 1 (Gladue *et al.*, 2012), which plays a key role during the autophagy process including the formation of double membrane structures. Moreover, guanidine hydrochloride (GuHCl) is an inhibitor of picornavirus replication (Nettleton, Davies and Rweyemamu, 1982; Pfister and Wimmer, 1999; Klein *et al.*, 2000) and yet, it was suggested that this inhibition of vRNA replication was associated with 2C (Pincus *et al.*, 1986; Pfister and Wimmer, 1999; Klein *et al.*, 2000). Thus 2C plays a critical role in modulating FMDV replication.

1.4.2.4. 3A

Alignments of 3A sequences from different picornaviruses shows that FMDV 3A has an extended C-terminal region therefore it is longer than the 3A in other picornaviruses, and the exact biological function is less well understood. However, 3A is involved in the host range, pathogenicity, and virulence of the virus (Pacheco *et al.*, 2003; Jackson and Belsham, 2021). There is various evidence for how 3A is involved, for example, attenuation of infectivity in cattle due to modification in 3A was previously reported (Beard and Mason, 2000). Recently, host DEAD-box RNA helicases (DDX) have been reported to have roles in FMDV translation and replication. DDX56 was reported to play a role in proliferating FMDV replication by interacting with 3A to promote the inhibition of interferon regulatory factor 3 (IRF3) (Fu *et al.*, 2019). Furthermore, 3A in other picornaviruses was shown to be associated with membrane rearrangement in infected cells (Suhy, Giddings and Kirkegaard, 2000). Co-expression of enterovirus 2BC and 3A results in the formation of membrane structures during replication (Suhy, Giddings and Kirkegaard, 2000; Limpens *et al.*, 2011). FMDV 3A also interacts with factors involved in the COPII pathway of membrane trafficking between ER and the Golgi during replication (Lee *et al.*, 2022), which collectively indicates 3A is an important viral protein that is closely associated with membrane rearrangements in infected cells.

1.4.2.5. 3B

3B, also known as VPg, is covalently linked to the 5' end of the positive- and negative-stranded RNA. In the presence of the 3D polymerase, the precursor 3CD and the *cre,* VPg is uridylylated into VPgpU(pU) using the *cre* as a template (Nayak, Goodfellow and Belsham, 2005). The uridylylated form of VPg then acts as a primer for RNA synthesis. The number of 3Bs varies amongst picornaviruses but most encode a single copy, FMDV uniquely encodes three nonidentical copies of 3B (Forss and Schaller, 1982). 3B is involved in determining the host range and virulence of FMDV (Pacheco *et al.*, 2003). More recent studies investigated the advantage of carrying three copies of 3B, and the number of 3Bs is potentially beneficial towards replication (Adeyemi *et al.*, 2021), and contributes to supporting FMDV immune suppression in the host cell (Zhang *et al.*, 2020).

1.4.2.6. 3C and 3D

3C^{pro} is responsible for processing the cleavage sites in the FMDV polyprotein except L^{pro} cleavage, 2A cleavage and the maturation cleavage of VP0. 3C^{pro} was previously reported to be involved in cleaving host translation factor eIf4G, which is primarily degraded by L^{pro} to inhibit host cell translation (Belsham, McInerney and Ross-Smith, 2000).

3D is an RNA-dependent RNA polymerase, and it is responsible for viral RNA synthesis (Ferrer-Orta *et al.*, 2004). 3D^{pol} requires uridylylated VPg to initiate the synthesis (Paul *et al.*, 2000; Nayak, Goodfellow and Belsham, 2005). The precursor protein 3CD has multiple functions, its major role is to act as an RNA-binding protein regulating translation and replication of the virus genome, it was reported that uridylyation of VPg is enhanced in the presence of 3CD (Nayak *et al.*, 2006). Poliovirus 3CD also perform protease activity during proteolytic processing of viral proteins (Ypma-Wong *et al.*, 1988; Parsley, Cornell and Semler, 1999), however, it does not retain polymerase activity even though it contains the entire amino acids of $3D^{pol}$ (Harris *et al.*, 1992).

1.4.3. 3'UTR

The 3' UTR possesses two stem-loops and the poly(A) tail and is crucial for genome replication and to maintain FMDV infectivity (Sáiz *et al.*, 2001). It was also shown that this region is capable of stimulating IRES activity (López De Quinto *et al.*, 2002) and that the stem loops in 3'UTR interact with the S-fragment (Serrano *et al.*, 2006).

1.5. FMDV life cycle

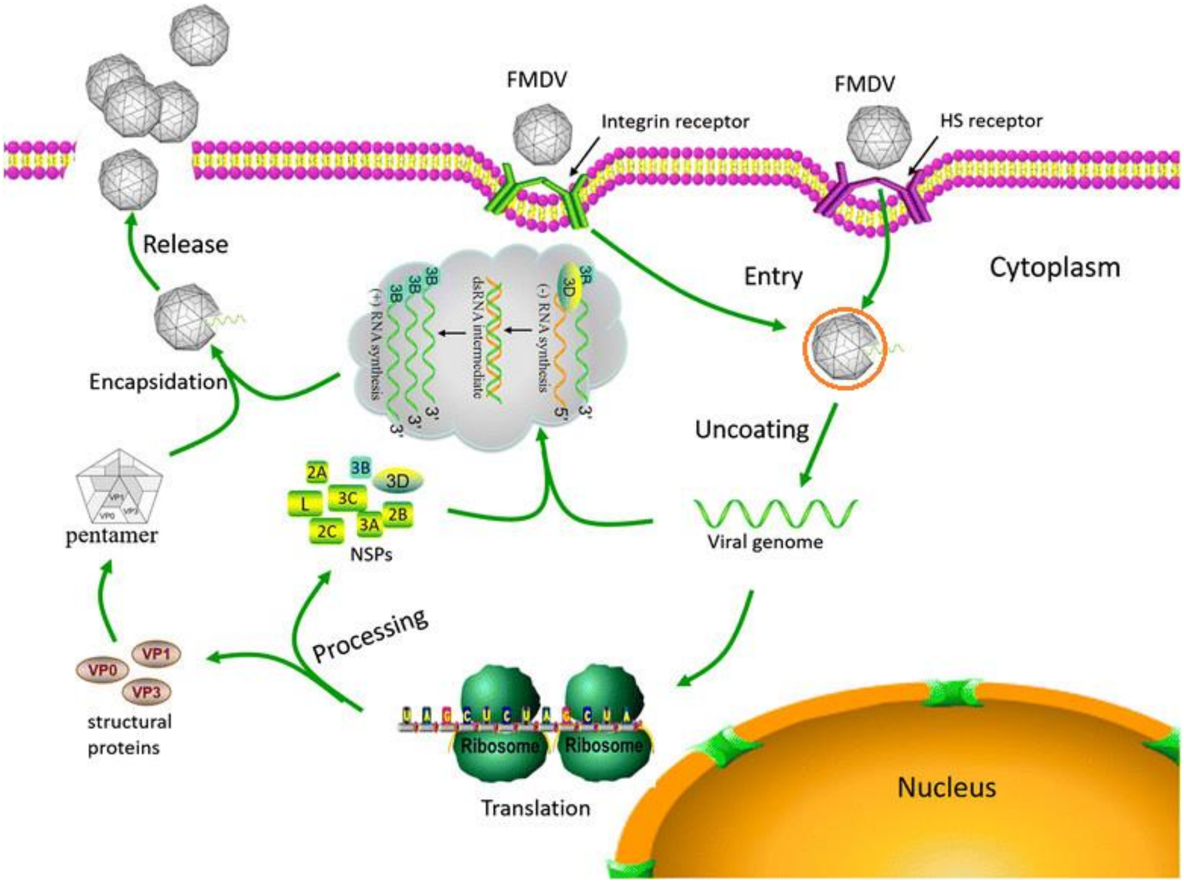

Figure 1.6 Schematic of FMDV life cycle.

FMDV entry is via attachment to either integrin receptor or heparan sulfate (HS) receptor. The capsid possesses a G-H loop that interacts with integrin receptors exposed on cell membranes which then initiate virus infection. The virus particle is internalised into an early endosome from which genome is first released into the cytoplasm and then capsid dissociated, due to the acidic environment, inside the endosome. The genome then undergoes translation producing the structural and non-structural proteins (NSPs). Then replication of the viral genome takes place in the cytoplasm at the rearranged host cell membranes in the cytoplasm. This is then followed by capsid assembly. Newly synthesised viral genome is then encapsidated, capsid precursor VP0 then cleaves into VP2 and VP4 forming an infectious virion. Newly formed virions are then released from the cell. Figure adapted from Gao, Sun and Guo, (2016).

1.5.1. Entry

FMDV enters the cell by receptor-mediated endocytic mechanisms (Figure 1.6). The receptors include RGD-dependent αv integrin receptors (αvβ-1, αvβ-3, αvβ-6 and αvβ-8) used by field isolates (Burman *et al.*, 2006; DiCara *et al.*, 2008) or heparan sulfate proteoglycans used by cell culture-adapted strains (Jackson *et al.*, 1996). Integrin receptors target the virus into clathrin-mediated endocytosis. Clathrin assembles on the cell surface forming a clathrin-coated pit (CCP), this then internalises the virus into the cytoplasm. This Clathrin-coated vesicle is then delivered to early endosomes where the acidification of the viral capsid releases the RNA into the cytoplasm. Alternatively, cell-culture adapted FMDV bind to heparan sulfate and enters cells via caveola-mediated endocytosis (O'Donnell, Larocco and Baxt, 2008). Another pathway is known as macropinocytosis where viruses trigger enzyme-linked receptor tyrosine kinases (RTKs) or integrin receptors, and further downstream trigger other signalling pathways. This ultimately results in the internalisation of the virus and the formation of macropinosomes (Han *et al.*, 2016).

Aphthovirus capsids are acid labile (Curry *et al.*, 1995; Tuthill *et al.*, 2009; Groppelli, Tuthill and Rowlands, 2010). They are internalised into early endosomes and upon entry, the acidic environment inside the endosome results in the dissociation of the capsid. Recent studies using ERAV have proposed a model whereby capsids undergo a slight conformational change protecting the genome from the acidic environment when being released into the cytoplasm (Tuthill *et al.*, 2009; Groppelli *et al.*, 2017). In a matured virion, VP0 was cleaved into VP2 (external) and VP4 (internal) (Curry *et al.*, 1995). In the proposed model, the altered capsid expose VP4 externally and interact with the endosomal membrane forming a pore enabling genome delivery into the cytoplasm.

1.5.2. Translation

After the genome is released into the cytoplasm, the next stage is the translation of viral proteins. Host cell translation is cap-dependent via the 43S ribosomal subunits recognising the cap structure located at the 5' end of the mRNA initiating translation (Shatkin, 1985). FMDV possesses an IRES in the 5' UTR, which initiates translation in a cap-independent manner. FMDV L^{pro} induces cleavage of eIF4G inactivating the cap-dependent complex (Devaney,' *et al.*, 1988). The cleaved eIF4G, which is still associated with the 43S ribosomal translation initiation complex, enables IRES binding. This then initiates the translation of the viral genome.

1.5.3. RNA replication

Following the translation of the viral RNA genome, replication of the RNA then takes place at replication complexes. These are the sites of viral replication that involve both host and viral components in a replication organelle (RO), which derives from rearranged host cell membranes that act as a platform for viral genome replication (please refer to section 1.6 for details). It is believed to originate near the cis-Golgi, which is the cisternae face of the Golgi membrane nearest the endoplasmic reticulum (ER) receiving vesicles from the ER, during early infection forming a vesicle which increases in complexity over time. This is described in more detail in section 1.6.

The single-stranded positive-sense viral genome is first involved in the initial production of negative-sense RNA genome. This negative-sense strand is then used as a template to produce more positive-sense RNA genome. For the synthesis of the genome, primers are required. VPg is therefore uridylylated. The uridylylation of 3B requires *cre*, 3Dpol and precursor 3CD (Nayak, Goodfellow and Belsham, 2005). The uridylylated VPg binds to the 5’ end of the positive- and negative- strand RNA acting as a primer for 3D^{pol} to synthesise RNA. VPg then binds to RNA binding cleft of polymerase thus initiating genome replication (Ferrer-Orta *et al.*, 2006). However, RNA translation and replication cannot take place simultaneously therefore, a switch between translation and replication has been proposed (Gamarnik and Andino, 1998). In polioviruses, viral protein precursor 3CD was shown to play a role in this inhibition (Gamarnik and Andino, 1998).

As mentioned above, viral replication then leads to formation of a replication complex associated with massive membrane rearrangement in host cell. The extensive rearrangements of host cell membranes is an important feature in picornavirus replication as it creates an environment facilitating the replication of viruses. A typical example of a replication organelle is the double membrane vesicle (DMV), which is considered a hallmark of FMDV viral replication. Details of the RO will be introduced in section 1.6 in this chapter.

1.5.4. Capsid assembly

Capsid assembly and packaging then take place following translation and replication. The capsid precursors are encoded by the P1 region: precursor VP0 (1AB) will be cleaved into VP4 and VP2 upon maturation, VP1 (1D), and VP3 (1C). The precursor protein is first cleaved by $3C^{pro}$ into VP0, VP1 and VP3. These monomeric subunits will then assemble into a pentamer (Chow *et al.*, 1987). After proteolytic cleavage of L^{pro}, myristoylation of VP4 is followed. It has been shown that a myristate moiety is covalently linked to VP4 and its precursor protein VP0 and P1. In polioviruses, this is found to be extended from VP4 and clustered near the five-fold axis suggesting that it plays a role in pentamer formation and stabilisation (Chow *et al.*, 1987). Twelve pentamers then self-assemble into a capsid structure; a 75S empty capsid, lacking the RNA genome with VP0 intact. Alternatively, a pro-virion containing VP0 will first be assembled. The viral RNA is covalently linked to VPg at the 5’ end and self-organises into an FMDV virion.

Upon RNA entry, the maturation or cleavage of VP0 is automatically triggered, resulting in the presence of VP2 and VP4 at the final stage. The assembly of capsids can fall into two pathways; one generates the virion and the other results in the formation of empty capsids (Rweyemamu, Terry and Pay, 1979; Curry *et al.*, 1995, 1997) (Figure 1.3C).

1.6. Site of replication

All +strand RNA viruses recruit and utilise host cell membranes for viral replication. The replication complex is where virus-induced rearrangement fuses host cell membranes and concentrates cellular organelles to shield the viral proteins from the host immune system for successful viral replication. The formation of a replication complex involves different complex interactions and signalling pathways between viral proteins and host factors. These collectively create a specialised compartment where viral replication and capsid assembly occur.

1.6.1. +RNA virus replication organelle

All +strand RNA viruses utilise host cell membranes to form a replication platform, termed the replication organelle (RO). The RO formed in response to different families of viruses can include single-membrane vesicles (SMV), double-membrane vesicles (DMV), spherules and complex interlinked membranous networks (Figure1.6).

The biogenesis of RO such as DMV is not well understood but details have slowly been revealed following the advances in 3D ultrastructural analysis. RO membranes are derived from intracellular organelles, such as the ER (Suhy, Giddings and Kirkegaard, 2000; Romero-Brey and Bartenschlager, 2016; Hackstadt *et al.*, 2021) and the Golgi (Hackstadt *et al.*, 2021; Nguyen-Dinh and Herker, 2021) and from components of the secretory pathway (Patarroyo, Laliberté and Zheng, 2013). Most of these virus-induced structures are vesicles delineated by either single- or double-membranes, i.e., SMV or DMV respectively. The type of RO induced is dependent on the viruses. Two major groups of ROs induced by +RNA viruses are as follows: the first group comprises spherical membrane vesicles which form a network with interlinked structures. Coronaviruses, including severe acute respiratory syndrome (SARS)-coronavirus (SARS-CoV) (Knoops *et al.*, 2008), Middle East respiratory syndrome (MERS)-coronavirus (MERS-CoV) (Snijder *et al.*, 2020), induce such ROs (Figure 1.7A), and infectious bronchitis virus (IBV) also induces spherules that are connected to zippered ER while a small proportion of DMVs are also connected to the ER (Maier *et al.*, 2013, 2014). It was shown that virus induced DMVs and spherules are conserved across genera such as IBV and SARS-CoV2. Recent work showed that the viral RNA synthesis takes place in the DMVs (Doyle *et al.*, 2021). The second group of ROs is virus-induced compartments where DMVs are a representative of this group (Figure 1.7B). DMVs are typically ~100 to 300nm in size. They are hallmarks of viral infection including picornavirus infection (Suhy, Giddings and Kirkegaard, 2000; Limpens *et al.*, 2011;

Belov *et al.*, 2012), norovirus (Doerflinger *et al.*, 2017) and Hepatitis C virus (Romero-Brey *et al.*, 2012; Neufeldt *et al.*, 2013). Although more details on their formation over the infection timecourse and types of RO structure detected in infected cells have been elucidated over past years, the source of membrane origin for ROs lacking connections is still difficult to identify.

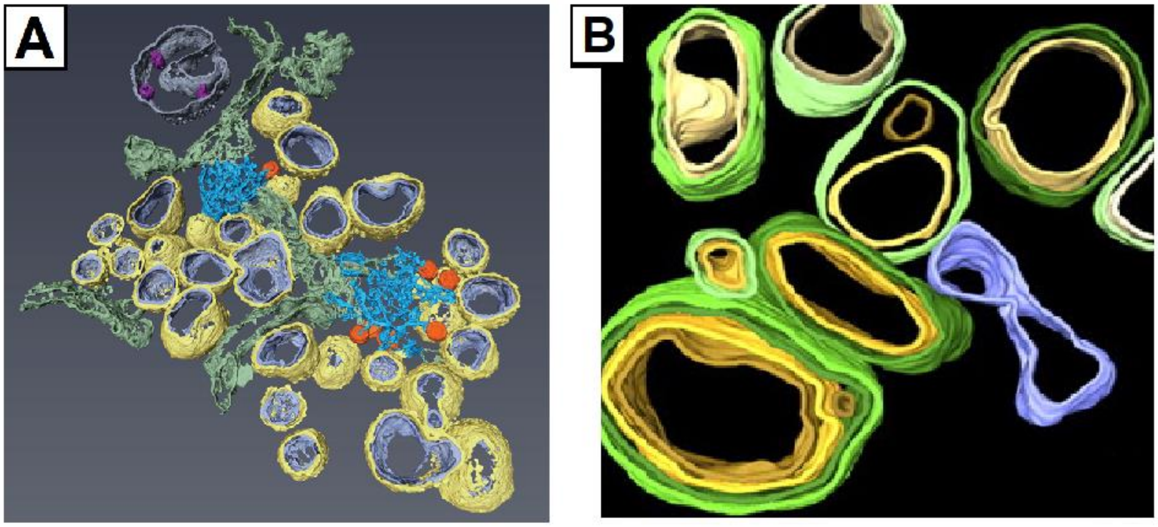

Figure 1.7 Reconstruction of replication complexes of coronavirus and poliovirus. Panel A is the 3D reconstruction of cryo-ET of Middle East respiratory syndrome (MERS) coronavirus induced replication model. The inner and outer membrane of DMVs are coloured lilac and yellow respectively. The replication complex includes the DMVs induced by coronavirus and is interconnected with the green ER and the blue convoluted membranes. Panel adapted from Snijder et al., (2020). Panel B is a 3D reconstruction of cryo-ET of poliovirus. The virus induces single membrane structures (blue) and double membrane structure (inner membrane and outer membrane are coloured yellow and green

respectively) that are separate compartments lacking connections to each other. Panel adapted from Belov et al., (2012).

Apart from the secretory pathway, the autophagy pathway can also be used by viruses for the remodelling of membranes to form DMVs. Autophagy is an important intracellular degradation process that maintains cellular homeostasis. Autophagy can be summarised into five stages: induction, nucleation, elongation, fusion, and degradation. Phagophores are formed originally as crescent-shaped vesicles and engulf, or segregate, extracellular pathogens and dysfunctional proteins or organelles. After phagophores expand and engulf the cytoplasmic content, the membrane continues to grow and ultimately fuses together forming the DMV, which is also known as an autophagosome. The outer membrane of the autophagosome then fuses with the lysosome forming autolysosomes, where all contents inside will be degraded including the inner membrane of the autophagosome. There are different variations of canonical autophagy which undergo similar processes as above but differ slightly. Canonical pathway initiation is dependent on the unc-51 like autophagy activating kinase 1 (ULK1) complex which then triggers the downstream events. Microtubule-associated protein 1A/1B-light chain 3 (LC3) is a soluble protein found in cells. During autophagy, the cytosolic form of LC3 (LC3-I) is conjugated to phosphatidylethanolamine. The conjugated LC3-phosphatidylethanolamine (LC3-II) is recruited to autophagosomes; therefore, it is commonly used as a marker for autophagy (Tanida, Ueno and Kominami, 2008). Autophagy markers LC3 have been shown to colocalise with various viral proteins during replication. We will discuss the evidence supporting how picornaviruses could potentially utilise the autophagy pathway in the next section (section 1.6.2). Hepatitis C virus (HCV) induces autophagy that facilitates viral replication. HCV induces the formation of a phagophore from the ER, where RNA replication was identified, the phagophore then progressed to the formation of autophagosomes (Wang *et al.*, 2017). Interestingly, HCV nuclear pore complex proteins have previously been reported to be associated with viral replication (Neufeldt *et al.*, 2013, 2016; Levin *et al.*, 2014), where these proteins were localised within the HCV replication complex, termed membranous web, and suggested that they play a role in regulating transport of host and viral protein to the membranous web.

1.6.2. Picornavirus RO

Picornaviruses induce both single and double membrane vesicles. Enteroviruses are the most extensively studied picornaviruses regarding RO. During poliovirus infection, small clusters of single membrane vesicles were first observed. This cluster of vesicles then eventually transformed into more complex single membrane structure, which then evolve into DMVs later in infection (Belov *et al.*, 2012). Another well studied picornavirus is coxsackie B3 (CVB3), which also induces both single and double membrane vesicles. Both poliovirus and CVB3 replication progresses in a similar fashion; firstly, the complexity of virus induced vesicles increases as infection progresses (Limpens *et al.*, 2011; Belov *et al.*, 2012;

Romero-Brey and Bartenschlager, 2014). Secondly, both have evidence suggesting that the Golgi might serve as a major source of membrane for the biogenesis of RO (Romero-Brey and Bartenschlager, 2014).

As described above, viruses can also utilise the autophagy pathway to facilitate viral replication. There is various evidence that picornaviruses also utilise this pathway in association with membrane rearrangement to facilitate viral replication. In polioviruses, 2BC and 3A are required for modification of LC3, which generates the viral replication platform DMVs (Suhy, Giddings and Kirkegaard, 2000; Jackson *et al.*, 2005; Taylor and Kirkegaard, 2007). A recent study revealed a detailed cryo-electron tomography (ET) study of poliovirus particles assemble on replication membranes, and yet virus-induced autophagy pathway plays a role in the secretion of infectious virions (Dahmane *et al.*, 2022). Collectively, this indicated the close association between autophagy and viral replication.

Another feature of enterovirus RO is the recruitment of lipid droplets (LDs) to the RO (Laufman, Perrino and Andino, 2019). Lipid droplets are important in lipid metabolism. Enteroviruses 2C recruits lipid droplets during the formation of RO. This redirects the host lipolysis pathway to provide a source of fatty acids to sustain phospholipid synthesis required for the formation of RO, thus contributing to viral replication. Recent studies have suggested that FMDV might recruit lipid droplets in a similar fashion to enteroviruses (Zhang *et al.*, 2022). Therefore, this increases the interest in investigating an association between lipolysis and viral replication.

1.6.3. Aphthoviruses RO

Membranes of RO might derive from different membranes depending on the virus. PV-induced vesicles derive from the ER early in infection (Suhy, Giddings and Kirkegaard, 2000) while various other sources such as the Golgi membrane disperse to form these vesicles later in infection (Sandoval and Carrasco, 1997; Suhy, Giddings and Kirkegaard, 2000; Rust *et al.*, 2001) . COPI and COPII are two coat protein complexes that are responsible for the membrane trafficking between the ER and the Golgi. Vesicles budding from the ER are coated in COPII, fusing with other pre-existing vesicular-tubular clusters. COPI binds to and coats these vesicles, and then travels to the Golgi. An important difference in picornavirus replication is indicated by their sensitivity to brefeldin A (BfA), an inhibitor of membrane trafficking between ER-to-Golgi via COPI. COPI coat is regulated by a GTPase ARF1, and this can be blocked by BfA thus preventing the formation of COPI-coated vesicles (Maynell, Kirkegaard and Klymkowsky2, 1992; E. V. Gazina *et al.*, 2002; Hsu *et al.*, 2010). Picornaviruses such as poliovirus and bovine enterovirus (BEV) are sensitive to BfA whereas FMDV and EMCV are independent of BfA (O'Donnell *et al.*, 2001; E. v Gazina *et al.*, 2002). Previously, FMDV was shown to be highly associated with the COPII pathway to form ROs (Midgley *et al.*, 2013), a recent study further revealed that COPII factors are associated with

FMDV 3A to remodel host ER into vesicles for replication (Lee *et al.*, 2022). Furthermore, RO induced by PV, Coxsackievirus B3 (CVB3) and enterovirus 71 (EV71) was shown to be enriched in phosphatidylinositol 4-phosphate (PI4P) lipid. Also, an increase in 3A proteins during replication induces selective recruitment of host type III phosphatidylinositol-4-kinase β (PI4KIIIβ) to the replication organelles (Hsu *et al.*, 2010). FMDV on the other hand is independent of PI4P and PI4K (Berryman *et al.*, 2016). FMDV infected BHK (hamster) cells previously demonstrated virus-induced membrane rearrangement over time using microscopy (Monaghan *et al.*, 2004). An accumulation of ribosomes, and fragmentation of ER, Golgi and vesicles were concentrated in the perinuclear region where the newly synthesised vRNA was localised (Monaghan *et al.*, 2004). This feature is not observed in other picornavirus infected cells and hence makes the FMDV replication site distinct from other picornaviruses. As mentioned earlier, picornaviruses interfere with the autophagy pathway during replication and this is a potential source of membrane for formation of RO. FMDV infection triggers ER-stress response and autophagy, and details on the regulation between the virus and host cell response by autophagy have been revealed over past years (Sun *et al.*, 2018; Yang *et al.*, 2020; Wu *et al.*, 2021). Autophagy can be triggered by UV-inactivated FMDV (Berryman *et al.*, 2012; Sun *et al.*, 2018) and empty capsids (Berryman *et al.*, 2012). Yet, autophagy could be beneficial towards infection as knockout of autophagy results in decrease in infectious titre (Berryman *et al.*, 2012). Furthermore, FMDV VP1 was shown to colocalise with LC3 (Berryman *et al.*, 2012) while VP2 interacts with heat shock protein family B (small) member 1 (HSPB1) to activate the EIF2S1-ATF4 pathway (Sun *et al.*, 2018). Nevertheless, the FMDV RO is less well understood compared to other picornaviruses.

1.6.4. Relationship between aphthovirus ROs and assembly

The link between capsid assembly and replication site is poorly understood but it was reported that defects in PKs region would hamper the production of infectious virions (Logan *et al.*, 2018; Ward *et al.*, 2022). The replication complex offers a site for virus replication and unpublished data from our lab has shown that assembled capsids appear next to replication sites (FMDV 3A). It is theorised that capsid assembly and viral replication should both take place within the site prior to release of infectious virions.

1.7. Conventional electron microscopy and cryo-electron tomography (cryo-ET)

Electron microscopy (EM) is an important tool that can be used to understand intracellular ultrastructure of biological samples. Conventional transmission EM uses relatively aggressive methods to fix samples. For example, chemical fixation requires dehydration of cells as water or liquid contents are not compatible with the vacuum found in the TEM. The fixed and dehydrated sample is then embedded in a resin block which will then be sectioned into thin slices before imaging. (Steps of conventional EM sample preparation will be described in Chapter 4.1). Biological samples have a low contrast leading to increased difficulty in analysis and interpretation of the samples. The addition of heavy metals at various stages throughout the preparation procedure via osmium tetroxide, uranyl acetate and lead citrate increase the number of electron scattering events, thereby increasing contrast in the TEM. This fixation method disrupts the native state of the biological sample, leading to potential artefacts in the cellular structures and thus complicating analysis. There are alternative methods to conventional fixation such as high pressure freezing. High pressure freezing cryo-preserves the sample in a vitreous ice state due to the high cooling rate. This provides a much better preservation of cellular ultrastructure. Even though the sample is preserved in a native state, the post-processing stage still requires the use of heavy metal stains and resin, which means that the native conformation may not be maintained.

Contrary to conventional TEM, cryo-electron microscopy (cryo-EM) and cryo-electron tomography (cryo-ET), use cryopreservation methods which preserve the cells in a near-native state (Mielanczyk *et al.*, 2014). By tilting the frozen sample at discrete angles and collecting a series of images, a 3-dimentional (3D) map of the target object can be reconstructed at a high resolution, i.e. near-atomic resolution can be achieved in some cases. In the first step biological specimens such as cells or virus suspensions are either grown or deposited on a carbon coated gold EM grid. Then excess liquid will be blotted away with filter paper leaving a thin film on the grid which is plunged into cryogen, such as liquid ethane, that is cooled by liquid nitrogen. This rapid cooling of the water molecules in the sample leads to specimen being vitrified in amorphous ice (vitreous ice), preserving biological specimens in their aqueous environment for EM analysis. Samples must be handled and stored at low temperature to prevent devitrification which results in the formation of ice crystals. In addition, vitreous ice does not discretely scatter the electron beam in the microscope which is crucial in data acquisition. Most importantly, staining, or chemical fixation is not required hence there is minimal disruption to the sample, and thus there are no chemical fixation artefacts that would complicate data interpretation.

Cryo-ET data acquisition involves tilting of samples over a range of angles at defined steps, re-aligning and focusing post tilt followed by the final exposure. A dose-symmetric scheme is used to collect cryo-ET data, the general principle is to start data collection at low tilt, where sample is thinnest and contain high resolution information, then alternating between negative and positive tilts to increasingly high tilt angles (Hagen, Wan and Briggs, 2017; Danev, Yanagisawa and Kikkawa, 2019). This scheme aims to minimise radiation damage that affects the high-resolution information that could be extracted from samples at the lower tilt angles.

The 3-dimensional (3D) scattering matter (i.e. objects of interest) in the specimen is projected in the 2-dimensional (2D) images acquired in the microscope. The absence of staining agents in cryo-ET specimens result in the low amplitude contrast in the images, as such the images have very little contrast. Therefore, contrast in cryo-ET images is dependent on phase contrast. When the sample in the microscope is in focus, electrons pass through specimen resulting in almost no intensity difference across the specimen. In order to increase contrast in the images, the objective lens in the microscope is defocused deliberately, meaning that we are imaging out of focus. The defocus increases the relative phase difference between the un-scattered and scattered electrons creating contrast in the images. The Contrast Transfer Function (CTF) is a fundamental concept in TEM that mathematically describes the modification of images based on the spherical aberrations of the objective lens, the defocus, electron scatter and the partial coherence of the beam (Erickson and Klug, 1970, 1971). Images generated in the electron microscopes are projection of the 3D objects modified by CTF on the objective lens. Other factors that affect CTF include are sample thickness and the partial coherence of the beam. Therefore, in order to obtain an accurate interpretation of the structure of the specimen, CTF estimation and subsequent correction must be performed using software such as RELION (Scheres, 2012b), WARP (Tegunov and Cramer, 2019) and IMOD (Kremer, Mastronarde and McIntosh, 1996). Reconstruction of tilt series into tomograms requires various computational processes to extract high resolution 3D information from the raw data, this includes tilt series alignment to refine the following parameters: tilt-axis angle, tilt angle, image shifts and beam-induced deformation during acquisition.

Single particle analysis is another approach, other than cryo-ET, for 3D structural analysis. SPA collects projections of objects that have different orientations within the layer of vitreous ice. Images are then aligned and averaged to reconstruct a 3D structure at a near-atomic resolution (Danev, Yanagisawa and Kikkawa, 2019). This method requires molecules, complexes, or viruses to be isolated, and requires objects to be more homogenous while cryo-ET is more suitable to analyse heterogenous samples such as pleomorphic objects and cells. Cryo-ET collects projections at different angles generating a series of tilted images. This tilt series is then used for 3D reconstruction. Therefore, cryo-ET is preferred over SPA to study in-situ structures and biological processing, from a whole cell to sub-cellular organelles, even virus assembly in cells, as it enables the analysis of pleomorphic viruses, virus-cell interactions, and virus structures in cells. Sub-tomogram averaging (STA) is a processing involving the alignment of objects in 3D. The aligned objects are then averaged (i.e. enhancing signal-to-noise ratio), improving resolution of structure obtained. Therefore, STA of cryo-ET data enables *in-situ* structure determination.

Thickness of samples is one of the limitations of EM. In cryo-ET, there have been various methods developed over past years to overcome this issue. One method is the sectioning of cells at cryogenic temperatures. Cryo-EM of vitreous sections (CEMOVIS) uses a diamond knife to cut sections in a dedicated cryo microtome, for subsequent imaging in the microscope. This method has various limitations such as cutting artefacts including knife marks, crevasses, chatter, and compression (Al-Amoudi *et al.*, 2004; Al-Amoudi, Norlen and Dubochet, 2004; Al-Amoudi, Studer and Dubochet, 2005). Interpretation of volume data is complicated by the artefacts induced during sectioning. Thus, the chance of obtaining good quality thin sections for cryo-ET imaging is difficult reducing throughput of this method. Cryo-focused ion beam (cryo-FIB) milling is a more recent technology and is still being developed with respect to sample quality and throughput. Cryo-FIB milling can generate cell sections, known as lamella, to around 150 – 250nm using the ion beam, meaning that it is free from compression (Rigort *et al.*, 2010; Zhang, 2019). The location of milling in a cell is highly controlled by the user and thus sites of interest are more accessible, with a higher chance of imaging areas that elucidate useful information. Remaining challenges such as contaminations from the redeposition of removed cellular materials on the sample surface and ice contamination due to storage and transfer of samples across microscopes need further improvement. Nevertheless, this method has been greatly beneficial in improving our understanding virus life cycle and its interaction with host cells.

1.8. Research aim

The understanding of aphthovirus induced RO, localisation of viral proteins, assembly of the capsid and the site of replication in cells is still not well established. Therefore, our project aims to explore these details using microscopy. We hypothesise that replication organelles derived from rearranged membranes, sites of genome replication and assembly of new virions are all located in proximity within the infected cell.

Our objectives are, firstly, designing recombinant FMDV where 3A encodes a tag that can be visualised by microscopy. This enables us to develop a correlative light-electron microscopy (CLEM) system for aphthovirus replication studies (Chapter 3). Then, we aim to compare the ultrastructure of FMDV and ERAV-infected cells using conventional TEM in Chapter 4. This provides insight into using ERAV as a surrogate model in a low-containment facility. Lastly, using advanced cryo-EM imaging, we aim to understand the details of ERAV replication by visualising the virus and its connections with the rearranged membranes in cells. Collectively, this will contribute to a better understanding of the replication cycle of aphthoviruses using microscopy.

Chapter 2 Materials and Methods

2.1. Production of recombinant viruses

2.1.1. Construction of infectious copy plasmids encoding tagged FMDV 3A protein

Plasmid constructs containing a fragment of synthetic DNA, i.e. the sequences of tags described in Chapter 3.2 (Table 3.1), with a new restriction site AscI in FMDV 3A were ordered from GeneArt.

2.1.2. Restriction enzyme digests

Plasmids were digested using restriction enzymes, AscI (NEB), BlpI (NEB) and MfeI (NEB). 5 µg of plasmid was digested with 1 µL each of the two appropriate restriction enzymes (10 units) and 2 µL of 10x rCutsmart Buffer (to a final concentration of 1x) to insert tags into FMDV 3A (details of the two-stage cloning will be described in Chapter 3.2.1). The reaction was made up to a final volume of 20 µL with nuclease-free water. Reaction was then incubated at 37°C for 1 hour before running on 0.8% agarose gel (please refer to section 2.1.3).

2.1.3. DNA dephosphorylation

Vector DNA plasmids that were digested with enzymes, were then dephosphorylated using rAPid Alkaline phosphatase (Roche) following manufacturer’s protocol. Each reaction contains 1 μg of DNA, 1x rAPid Alkaline Phosphate buffer, which is supplied in 10x concentration within the kit, and 1 unit of rAPid Alkaline Phosphatase. Each reaction is made up to a final volume of 20 μL with nuclease-free water. Reaction was then incubated at 37°C for 15 minutes followed by inactivation of rAPid Alkaline Phosphatase for 3 mins at 75°C.

2.1.4. DNA ligation

Ligation was performed following manufacturer’s protocol. DNA fragments were ligated using T4 DNA ligase (Promega). Ligation reaction was made up of vector DNA and insert DNA in a 3:1 molar ratio. In addition, 1 μl of Ligase from ligase 10x buffer and 1 U of T4 DNA ligase. Nuclease-free water was added to the mixture to a final volume of 20 μL. Reaction was then incubated at room temperature for 3 hours.

2.1.5. DNA electrophoresis

Agarose (Sigma) was mixed in 1x Tris-acetate EDTA (TAE) buffer (1x TAE diluted from 50x TAE solution containing 2.0M Tris Acetate and 100mM EDTA from Flowgen Bioscience) to 0.8% w/v agarose. Mixture was heated up in the microwave to dissolve the agarose powder. Once, agarose was dissolved, it was left to cool down slightly and ethidium bromide was added (5 μL ethidium bromide/100mL TAE w/v agarose). Once the solution was mixed, it was poured into a tray with an appropriate comb. This was then allowed to set at room temperature. Once the agarose gel was set, it was placed in a tank with 1x TAE. 24 µL of DNA marker, which was 1kb ladder (NEB), was loaded into the well. Each sample was mixed with 6x blue loading dye (Promega) in a 1:5 (loading dye:sample) ratio. Gel was then run at 100V for 40 mins. Agarose gel containing the DNA was then imaged in a UV transilluminator (Biorad).

2.1.6. Gel extraction

DNA was run on a 0.8% agarose gel (protocol described in section 2.1.5.). For each reaction 2 µL DNA was mixed with 1 cutsmart buffer (NEB), and appropriate restriction enzymes. The mixtures were then made up with water to a final volume of 10 µL. Extraction and purification of DNA was performed following manufacturer's protocol (GE healthcare) using the illustra GFX PCR DNA and gel band purification kit. In general, a capture buffer supplied in the kit was added to dissolve the agarose. Dissolved sample was then added to a GFX column and centrifuged; DNA would then bound to the silica membrane inside the column. The membrane, where DNA was bound to, was washed with ethanol buffer to remove any residuals of contaminants. DNA was then eluted in the Tris-hydrochloride (Tris-HCL) elution buffer (EB buffer). All buffers were supplied in the kit.

2.1.7. Transformation

DH5α bacteria were used routinely for sub-cloning. DNA plasmid concentration was recorded to be approximately 50 µg/µL. Therefore, the general protocol to transform bacteria was as follows: aliquots of 50 µL competent bacteria were thawed and 1 µl of plasmid DNA was added. This was immediately followed by a 30 mins incubation on ice. Then, competent bacteria, with DNA, were placed in a 42°C water bath for 50 seconds and immediately removed and placed on ice for 2 minutes. 250 µl of super optimal broth with catabolite repression (S.O.C.) medium (Invitrogen) was added after incubation on ice. The mixture was then placed in a shaker at 37°C for one hour. Either 270 µl (90%) or 30 µl (10%) was spread on agar plates containing the corresponding antibiotics based on the antibody resistance gene encoded in the plasmid backbone (50 µg/mL Kanamycin or 100 µg/mL Ampicillin; Central servicing unit (CSU), The Pirbright Institute). Plates were then incubated at 37°C.

Individual colonies were picked and transferred into 5mL of Luria-Bertani (LB) broth with the corresponding antibiotic for small scale plasmid prep. Bacterial cultures were then placed in shaker at 37°C overnight. For large scale plasmid prep, 1mL of bacterial culture would be transferred to 500mL LB with corresponding antibiotic and incubated at 37°C overnight.

2.1.8. Plasmid purification

Plasmid DNA was purified from bacterial cultures using a QIAprep spin miniprep kit (Qiagen) for small scale plasmid prep or QIAprep maxiprep kit (Qiagen) for large scale plasmid prep following the manufacturer's protocol. Specific conditions or volumes were followed according to manufacturer's protocol, but the generic protocol was as follows: bacterial cells were harvested by pelleting through centrifugation. The pellet was resuspended in resuspension buffer and alkaline lysate. This was then neutralised with neutralization buffer containing potassium acetate, resulting in the precipitation of bacterial DNA, proteins and cell debris leaving behind the plasmid in solution. Precipitates were then centrifuged and pelleted, the supernatant containing the plasmids was then transferred to a QIAGEN-tip. The bound plasmid DNA was washed with a washing buffer containing 70% ethanol. DNA was then eluted in nuclease-free water.

2.1.9. DNA quantification

DNA was quantified using Nanodrop 2000 Spectrophotometer (Thermo Scientific). Prior to measuring DNA concentration, 1 µL appropriate elution buffer (EB buffer for DNA extracted from gels or TE buffer for DNA from miniprep or maxiprep) was placed on pedestal and absorbance of 260nm was used to take reading. This step would calibrate the machine. Then 1 µL DNA was placed on pedestal and readout represents the concentration of DNA in ng/µL.

2.1.10. RNA

The DNA plasmids then underwent in vitro transcription using MEGAscript T7 kit (Invitrogen) into RNA following manufacturer's protocol. 1 µg of DNA was digested with restriction enzyme and the linearised DNA was then used in subsequent reaction. For each reaction, 1 µg of linearised DNA, 2 µL of enzyme mix, 7.5 mM each of ribonuclease solution (ATP, CTP, GTP and UTP solutions), 2 µL of 10x Reaction Buffer, which were supplied with the kit, and nuclease free water to make up to a 20 µL reaction. The reaction was assembled and incubated at 37°C for 2 – 4 hours.

MEGAclear kit (Invitrogen) was used to purify RNA from in vitro transcription reaction. Typically, a reaction with RNA transcript was first assembled with elution solution to 100 µL. This was then mixed with 350 µL binding solution concentrate. Following that, 250 µL of 100% ethanol was mixed to the sample and applied to the filter (supplied with the kit). This was centrifuged to remove liquid and bind RNA to the filter inside the column. The filter was then washed twice in 500 µL of wash solution and supernatant was removed by centrifugation. RNA was then eluted in nuclease-free water. Concentration of RNA was quantified using a Qubit Fluorometer and the Qubit RNA BR Assay kit (Invitrogen) according to manufacturer's protocol. BR reagent and BR buffer (provided with the kit) was assembled in a 1:200 (BR reagent:BR buffer) ratio. For each measurement, 1 µL of RNA was added to 199 µL of the BR regent-BR buffer mixture for analysis in the Qubit Fluorometer. Readout was calculated according to manufacturer's protocol in ng/µL. After concentration of RNA was measured, samples were then run on 1.5%

agarose gel following the same protocol in section 2.1.5. to make up agarose gel. Sample assembled contains RNA and loading buffer (supplied in Megascript) in equal volume and diluted in nuclease-free water before loading onto gel.

2.1.11. Recovery of 3A-tagged virus from infectious copy plasmid

BHK cells were seeded in a T25 flask (Thermofisher Scientific) with appropriate media. Media was replaced with virus growth media (VGM; recipe will be described in section 2.2.). Cells were then transfected with RNA using Lipofectamine 2000 (Invitrogen). mRNA boost and Transit reagent was mixed in a 1:1 ratio at room temperature and vortexed before use. 6.5 µg of RNA was mixed with 650 µl Opti-MEM, then the mRNA boost and transit reagent mix were added to the mixture. It was then incubated at room temperature for 5 mins allowing the RNA-Opti-MEM complex to be formed. This mixture was then added to cells and incubated at 37°C for 24 hours. Flasks were then freeze at -20°C until being aliquoted.

To recover the viruses, cells were infected with transfection supernatant with appropriate media, i.e. VGM. Once development of cytopathic effect (CPE) was observed, flasks would be freeze at -20°C.

Frozen flask of transfected cells or infected cells were thawed. Supernatant, containing cell debris, were then transferred to a 15mL or 50mL falcon tube. These were then centrifuged at 3000rpm for 10 minutes at 4°C. Supernatant was then aliquoted and stored at -80°C.

2.1.12. Sanger Sequencing

Virus lysates were inactivated, and RNA extracted using an RNeasy mini kit. Virus lysate was added to RLT buffer in an equal volume to deactivate the virus. 1 volume of 70% ethanol was added to the mixture and transferred to a spin column. Samples were then centrifuged and flow-through was discarded. This was repeated first with 700 µL of buffer RW1, then with 500 µL of buffer RPE twice. Spin column was then transferred to a collection tube and eluted in RNase-free water.

First strand synthesis of RNA was completed using the Super Script First Strand synthesis (Thermofisher Scientific) following manufacturer's protocol, the end products from this stage was cDNA. Typically, each reaction was assembled with 1x SSIV buffer, 0.5 mM each of the 10 mM dNTP mix, 5 µg of RNA, 2 µM of forward and reverse gene-specific primer and DEPC-treated water was added to make up a final volume of 10 µL reaction at room temperature. cDNA was then processed using the Platinum Tag High Fidelity kit (Thermo fisher Scientific). In brief, a PCR master mix was prepared with 10x High Fidelity PCR buffer to a final concentration of 1x concentration, 10mM dNTP mix to a final concentration of 0.2mM each and 50 mM of Magnesium sulfate to a final concentration of 2 mM and

1 U of platinum Tag DNA High Fidelity polymerase which was supplied at 5 U/µL. Then, for each reaction, 0.2 µM each of the forward and reverse primers were added to cDNA and the PCR mix. Distilled water was added to a final volume of 50 µL reaction. This was then amplified in PCR machine. Initial denaturation was performed at 94°C. Then, sample underwent 30 cycles of denaturation at 94°C for 15 sec, annealing at 55°C for 30 seconds and extended at 68°C for 1 minute was performed. Samples were hold at 4°C until purification. PCR products were then extracted and purified using GE healthcare kit similar to protocol described in section 2.1.6 following manufacturer's protocol. Purified PCRs were then eluted in nuclease-free water.

Sequencing reaction was prepared according to the BigDye Terminator v3.1 Sequencing kit (Applied Biosystems). For each reaction, 500 ng of PCR product was assembled with 2 µL of 5x sequencing buffer, 0.25 µL of bigDye Terminator v3.1, forward or reverse primer at 1pmol and deionised water to make up a final volume of 10 µL. Reactions were then amplified in a PCR machine, at 96°C for 1 minute and 30 cycles of the followings: 96°C for 1 min, then 96°C for 10 sec followed by 50°C for 5 sec and 60°C for 4 min. Sequencing mixtures were then ethanol precipitated. For each reaction, 5 µL of 0.25M of ethylenediaminetetraacetic acid (EDTA) was added to the sequencing reaction. 60 µL of absolute ethanol was used for the first wash, plate containing samples was sealed and vortex for 15 sec to mix sample with EDTA and ethanol. Samples were left in dark for 15 mins then centrifuged at 1870x g for 30 mins. Then plate was pulsed for 7 sec, upside down to remove liquid. Then it was washed with 70% ethanol. After washing with ethanol, 60 µL of 70% ethanol was then added to each reaction and centrifuged at 1870x g for 15 mins. After discarding supernatant, plate containing sequencing sample was vacuum dried for 30 mins. The sequencing reaction was resuspended in 20 µL Hi-Di Formamide (Applied Biosystems) and run on an ABI 3730 DNA analyser (Applied Biosystem, Plowright Building, the Pirbright Institute).

Table 2.1 Primers used for first strand synthesis and PCR.

Primer	Sequence
FMDV 3A For	TGGCAAACATTGTGATCATG
FMDV 3A Rev	GCTCTCACTTTCAGAGGTTTC

2.2. Cell culture

Baby hamster kidney (BHK) cells was obtained from the central services unit (CSU) at The Pirbright Institute for cell culture experiments and preparation of viruses and virus titrations. BHK cells were cultured in Glasgow's minimum essential media (GMEM, Merck) and supplied with 10% (v/v) sterile foetal bovine serum (FBS, Life Science Production), 2mM L-Glutamine, 100 units/L penicillin (Life Technologies), 100 µg/L streptomycin (Life Technologies) and 5% tryptose phosphate broth (Gibco).

Vero cells (from CSU) and PK-15 cells (a gift from Professor Jurgen Hass, University of Edinburgh) were cultured in Dulbecco's Modified Eagle Medium (DMEM) supplemented with 10% (v/v) sterile foetal calf serum (FCS) and 100 µg/L penicillin, 100 µg/L streptomycin at 37°C and 5% CO_2. PK-15 transduced with the GFP1-10 cell line was generated by Connor Haywards and Dr. Joseph Newman (Pirbright Institute). Cells were transduced with pQxIP BDR GFP1-10. This cell line was cultured in the same media as described, with the addition of blasticidin at the concentration of 10mg/ml.

SK-RST (gift from Professor Jurgen Hass, University of Edinburgh) was cultured in DMEM supplemented with 10% FCS, 1% P/S and 1% L-Glutamine. SK-RST was first reported to be a porcine cell line, however, later revealed to be a hamster cell line.

For virus infection, VGM was used, which contained the same components but was supplemented with 1% FBS for FMDV infection; VGM for ERAV infection contains an addition of 25 mM HEPES (Gibco).

2.3. FMDV plaque assay titration analysis

PK-15 cells were seeded in 6-well plates and incubated until confluent. Prior to infection, cells were washed with PBS and infected with 100 µl of 10-fold serial virus dilutions. Infected cells were incubated at 37°C for 15 minutes. 4mL of warm Eagles overlay containing 0.6 g agarose (indubiose), 1% FBS, and 1% P/S was added and set aside at room temperature. This was then incubated at 37°C for 48 h and stained with 4 mL/well of methylene blue overnight. Overlay and the excess stain were then washed off and plaques were manually counted to calculate the virus titre in plaque forming units per mL (PFU/mL).

2.4. ERAV time-course plaque assay titration analysis

Vero cells were seeded in 12-well plates and when confluent, cells were infected with 400 µl virus lysate. The plate was then returned to the incubator at 37°C and incubated for 1 h. Acid wash was made up of 0.1M citric acid and 0.2M Sodium Phosphate Dibasic to pH 5.2. After 1 h of virus absorption, virus lysate was removed, and infected cells were washed with acid in 1 mL. Then it was washed twice in acid for approximately 2 minutes per wash followed by two washes with higher volume, 2 mL, VGM and then one 1 mL wash in VGM. Fresh VGM was added, and the plate returned to the incubator until the desired time points at 1h, 4h, 8h, 10h, 12h, 16h and 24h post-infection. At the harvesting time point, cells were scraped off the plate and transferred to a fresh Eppendorf tube together with the lysate. The supernatant was then stored at -20°C until the end of the experiment and transferred to -80°C prior to titration.

The plaque assay titration procedure was followed as described in section 2.3. but with Vero cells seeded in 6-well plates, 200 µl virus dilution was used for infection and cells were incubated with virus supernatant for 30 minutes. The overlay was incubated at 37°C for approximately 70 h for plaques to develop before staining.

2.5. Incucyte

Cells were seeded in a 96-well plate (Thermofisher) until ~70% confluency was reached. 5 wells were then trypsinised for cell counting. Prior to infection, cells were washed with VGM, infected with 50 µl per well and incubated at 37°C for 1 h. After 1 h of virus incubation, the lysate was removed, and cells were washed in 200 µl of VGM. 200 µl fresh VGM was then added to each well and the plate was analysed in Incucyte.

2.6. Coverslips preparation

Cells diluted to the desired density in cell culture medium were seeded on 13mm glass coverslips (VWR) in a 24-well plate. Cells were incubated at 37°C for 24 hours. Prior to infection, each coverslip was washed with 800 µl of VGM. These were then infected with 300 µl of virus lysate diluted in VGM for 1 hour at 37°C. After 1 h of virus absorption, the virus inoculum was removed and washed with 800 µl of VGM, which was then replaced with fresh 800 µl of VGM for further incubation at 37°C until fixation. At the fixation timepoint, cells were fixed in 4%

paraformaldehyde (PFA) in PBS for 45 mins. This was then washed twice in PBS and stored in fresh PBS at 4°C until immunofluorescence labelling.

2.7. Transient transfection of GFP1-10

Near 50% confluent cell monolayer grown on coverslips was transfected with plasmid pQxIP BDR GFP1-10 expressing GFP1-10 protein using Lipofectamine 2000 reagent (Life technologies). The two mixtures were prepared separately: DNA was diluted in Opti-MEM (Gibco) to a final concentration of 0.8 µg/50 µl and Lipofectamine 2000 (Invitrogen) reagent was diluted in Opti-MEM to 2 µl/50 µl. The two mixtures were incubated at room temperature for 5 mins before mixing equal volumes of lipofectamine-opti-MEM solution and DNA-opti-MEM solution and incubated at room temperature for a further 20 mins enabling the formation of DNA-lipofectamine complexes. Meanwhile, media was removed from the coverslips and replaced with 500 µl fresh cell culture medium. 100 µl of DNA-lipofectamine complex-containing mixture was added to each coverslip and then returned to the incubator at 37°C for 17 to 24 hours.

2.8. Immunostaining

Infected cells stored at 4°C or after the fixation step following the protocol mentioned in section 2.5 were permeabilised with 0.1% Triton-X100 for 15 mins. This was then followed by three 5-mins PBS wash. Cells were then blocked with blocking buffer PBS/Bovine Serum Albumin (PBS/BSA; Sigma) for 30 mins. After the blocking buffer was removed, coverslips were then incubated with 200 µl primary antibody diluted in PBS/BSA for 60 mins. This was washed in PBS as described above. After the PBS washes, cells were then incubated with 200 µl secondary antibody diluted in PBS/BSA for 45 mins. Cells were washed twice in PBS as above and stained with DAPI, diluted in sterile water (1:10000) for 8 mins. Immunolabelled coverslips were then stored in PBS until mounted with vectashield (Vector laboratories) on glass slides. Slides were then stored at 4°C until image acquisition.

2.8.1. Tetracysteine (Re-Ash) protocol

This protocol was adapted from the Re-Ash detection kit (Life Technologies) manufacturer's protocol. Refer to section 2.5 for the set-up of coverslips and infection procedure, and section 2.6 for GFP1-10 transfection for the split-GFP system. At the fixation timepoint, VGM was removed, and cells were washed twice in 1ml Opti-MEM. Coverslips were then incubated with 250 µl Re-Ash (1:800 in Opti-MEM), and covered in dark foil, for 30 mins at room temperature. This was followed by two 5-minute BAL washes (dilution 1:100 in Opti-MEM) supplied within the kit at room temperature. Prior to fixation, they were washed with 800 µl PBS. After fixation, they were directly stained with DAPI.

2.8.2. ER tracker protocol

Red BODIPY TR Glibenclamide (ER tracker; Invitrogen) protocol was adapted from the manufacturer's protocol. Typically, ER tracker was diluted in appropriate buffer, such as HBSS, or cell-culture media (DMEM) to 1 µM concentration and warmed up at 37°C. Cells were seeded on coverslips in a 24-well plate, as described in section 2.6, and supplied with GFP1-10 following the split-GFP protocol described in section 2.7. Prior to staining, cells were washed with appropriate buffer prior to addition of ER tracker. 300 µL ER tracker was added to each coverslip and incubated at 37°C for 30 mins. Stain was removed and washed in VGM. Infection was performed as described in section 2.6 and fixed with 4% PFA. After PFA was removed, cells were washed in PBS and directly stained with DAPI and mounted on slide.

2.8.3. Golgi tracker

Following coverslips set-up and infection protocol, or transfection of plasmid in the split-GFP system, described in sections 2.6 and 2.7 respectively, this protocol was adapted from the manufacturer's protocol and Bakrač et al. (2010). 5 µM of BODIPY TR ceramide (Golgi tracker; Invitrogen) was prepared from stock in HBSS. Cells were washed twice in DMEM-HBSS mixture in equal volume. 300 µL of 5 µM Golgi tracker for 30 mins at 4°C. After incubation with the Golgi tracker, cells were washed in DMEM-HBSS at 37°C for 30 mins. After incubation, cells were washed in VGM twice and infect following protocol described in section 2.6.

2.8.4. ERAV 3A-antisera

Anti-sera against ERAV 3A was produced in rabbits (purchased from Mologic) was used in validating infection of ERAV at a dilution of 1/1000 (Table 2.3). They are designed so that both peptides subsequently cover the whole 3A sequence, where peptide 1 covers ERAV 3A amino acid 1-35 and peptide 2 covers amino acid 26-30 in the 3A region (Table 2.2).

Table 2.2 ERAV polyclonal anti-sera amino acid sequence.

ERAV anti-sera	Amino acid
Peptide 1	Amino acid 1-35 SWSDLFKKCSTDEEQKMLQFLIDNKDSEILRAFVS
Peptide 2	Amino acid 26-60 ERSILLHEEYLKWESYMTRRAKFHRLAADFAMFLS

2.8.5. Antibody dilution

Immunostaining of cells following the protocol described in section 2.8. Antibodies were used at dilutions listed in Table 2.3.

Table 2.3 List of antibodies used for immunolabelling.

Antibody	Supplier	Dilution in PBS/BSA	Primary/Secondary antibody	Comment
Anti-HA Mouse Monoclonal	Sigma-Aldrich	1/500	Primary	Primary antibody labelling HA-tagged FMDV

Anti-FLAG Mouse Monoclonal	Sigma-Aldrich	1/300	Primary	Primary antibody labelling FLAG-tagged FMDV
2C2 Mouse Monoclonal	Emiliano Brocchi Iszler	1/1000	Primary	Primary antibody labelling FMDV 3A.
IB11 Mouse Monoclonal	Pirbright Institute	1/300	Primary	Primary antibody labelling FMDV capsid proteins.
M170 Llama Monocloncal (VHH antibody)	Merial S.A.S, Netherlands	1/400	Primary	Primary antibody labelling FMDV intact capsids only.
Anti-ERAV 3A Peptide 1 Rabbit Polyclonal	Mologic	1/1000	Primary	Primary antibody labelling ERAV 3A amino acid 1-35.
Anti-ERAV 3A Peptide 2 Rabbit Polyclonal	Mologic	1/1000	Primary	Primary antibody labelling ERAV 3A amino acid 26-60.
Alexa Fluor 546 goat anti-rabbit	Thermo Fisher Scientific	1/500	Secondary	-
Alexa Fluor 568 goat anti-mouse IgG (H+L)	Thermo Fisher Scientific	1/2000	Secondary	-
Streptavidin Alexa 488	Thermo Fisher Scientific	1/200	Secondary	-

2.9. EM sample preparation

2.9.1. Conventional fixation

A phosphate buffer was made up as a vehicle for glutaraldehyde by combining two phosphate solutions to pH7.2 and adding sucrose to balance the osmolarity. Initially, 2.722g sodium dihydrogen orthophosphate (Sigma-Aldrich) was dissolved in 100mL distilled water. Then 0.8g sodium hydroxide was dissolved in another 100mL of distilled water. In a fresh bottle, 58mL of sodium dihydrogen orthophosphate was added to 46mL of sodium hydroxide, resulting in a 0.2M EM buffer stock solution. When needed to prepare the working fixative solution, this was then further diluted to a concentration of 0.05M in water in a 1:3 (0.2M EM buffer: water) ratio.

To make up the working fixative, 8mL of 25% glutaraldehyde (Sigma-Aldrich) was added to 0.05M EM buffer mixture to make up to a final volume of 100 mL 2% glutaraldehyde. To balance the osmolarity between the fixative solution and the cell (approximately 300mOsm), 1.71g/100mL of sucrose was added to the fixative at this stage. The fixative solution was then aliquoted and stored at -20°C. Aliquots were thawed and warmed up to room temperature prior to fixation, as needed.

Cells were seeded on 13mm round NUNC thermanox plastic coverslips (Thermofisher) overnight at 37°C. The infection protocol was followed as above. At the fixation timepoint, 2% glutaraldehyde was used to fix infected cells at room temperature for 1 hour. This was followed by fixation/staining with aqueous 1% osmium tetroxide (Agar Scientific) at room temperature for 1 hour. This was replaced with 70% ethanol for 30 mins, then 90% ethanol for 15 mins, and then three stringent 10 mins washes with 100% ethanol. Medium hardness resin was made up of 36g Agar 100 eproxy resin (Agar Scientific), 24g of dodecenyl succinic anhydride (DDSA; Hardener; Agar Scientific), 15g methyl nadic anhydride (MNA; Hardener; Agar Scientific), and 2.25g of benzyl dimethylamine (BDMA; Accelerator; c. 3%; Agar Scientific) in a plastic bottle. After ethanol dehydration of samples, coverslips were transferred to solvent-resistant moulds (TAAB) before the cells were infiltrated gradually with resin. They were first washed in propylene oxide (to remove any ethanol) for 10 mins, then in propylene:resin in 50:50 ratio for 45 mins. This was completed with a final infiltration in resin for 1 hour at room temperature. After this, the resin was replaced with fresh resin and coverslips were polymerised in an oven at 60°C overnight. Finally, plastic coverslips were peeled off from the polymerised resin block, leaving the cells embedded at the hardened resin surface. Blocks were cut en face to ensure similar orientation (in Z direction) of all cells (Bioimaging team, Pirbright). After grid staining with uranyl acetate and lead citrate sections were analysed in the TEM.

2.9.2. Cryofixation for ERAV

R2/2 Au300 gold grids were dipped in 70% ethanol, then washed in HBSS (Gibco), and incubated with filtered FBS in a 6-well plate (Thermofisher) prior to use. Cells were then seeded on grids in a fresh 6-well plate (Thermofisher) at 1 x 10^5 cells/well. Vero cells were then infected with ERAV and incubated with virus supernatant diluted in 1% DMEM, 1% P/S and 25mM HEPES at 37°C. Infected cells were then plunge-frozen in liquid ethane at 8h, 9h or 11h post-infection using a Leica GP2 plunge freezer (Leica Microsystems) at -170°C, 70% humidity and blot time 8 s.

2.10. Microscopes

2.10.1. Confocal (Pirbright and Diamond)

Confocal images were taken using microscopes at The Pirbright Institute (Leica SP8 CLSM using x63 oil immersion lens) and the Research Complex at Harwell. Images were resized using Adobe Photoshop.

2.10.2. TEM (Pirbright)

Cells prepared by conventional chemical fixation (section 2.9.1) were viewed on a Tecnai T12 TEM (FEI) at 100kV. Images were acquired using a TVIPS F214 2Kx2K camera and FEI TIA software.

2.10.3. Cryo-soft-X-ray

Data acquisition was carried out at B24, Diamond Light Source and collected in conjunction with the B24 team using a Fresnel zone plate with an outermost zone width of 25nm. Cells were acquired at 500eV, detector pixel at 10nm and the resolution at approximately 25nm. Tilt series were collected from -60° to +60° at the increment steps at 0.5° and 1°.

2.10.4. Focused ion beam milling

Grids were clipped into autogrid rims (Thermo Scientific). Clipped grids were then loaded into the Scios DualBeam system (Thermo Scientific) or the Aquilos DualBeam system (Thermo Scientific). Grids were coated with a layer of platinum using a gas injection system built-in the microscope. Milling was then performed using a 30-kV Ga ion beam. Cells were milled using beam currents 300, 100 and 30pA in a stepwise manner to generate a lamella with a final thickness of approximately 150 to 200nm. Milling progress was monitored using a 3-5 kV beam and 25pA beam current through a scanning electron microscope. Auto-milling was performed through the same settings using the AutoTEM program from Thermo Scientific. The procedures followed as above.

2.10.5. Cryo-ET data acquisition

Tilt series were collected using a Titan Krios electron microscope (Thermo Scientific) located at eBIC (Krios III). The microscope was operated at 300 keV with a selectris-X filter and falcon 4 camera. Tilt series were collected at a magnification of 42K, and defocus range of -5 to -2 microns; pre-tilt of 13° was used to compensate for the milling angle and a tilt range of ±50° with 2° increment and an electron dose of 2.06 e^-/A^2/tilt.

2.11. Cryo-electron tomography data processing

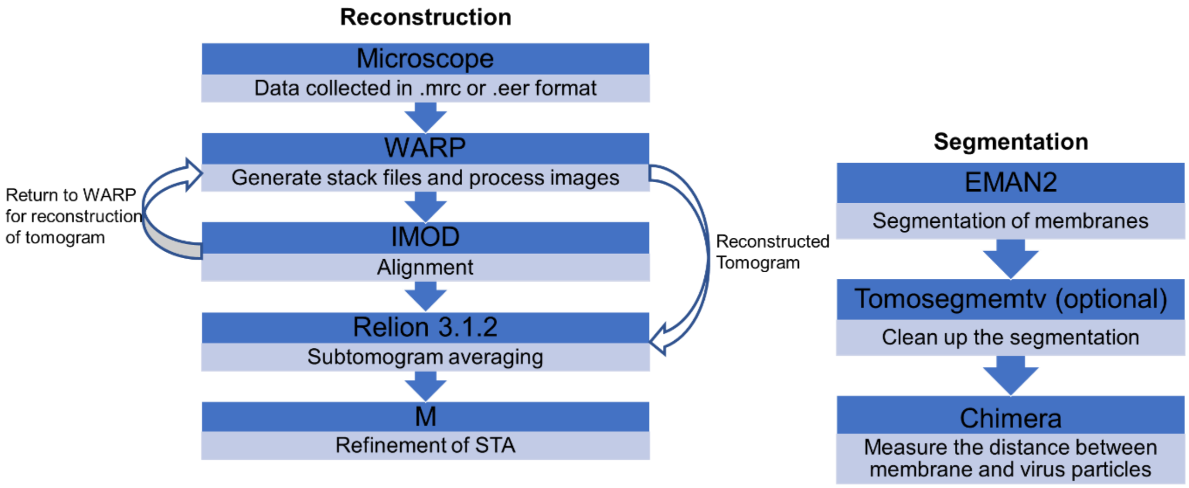

Figure 2.1 Schematic workflow of cryo-electron data processing.

Tilt series collected from cryo-EM. Tilt series were then imported into WARP program for pre-processing. This then generate tilt series for alingment using IMOD. The alignments were then imported into WARP for tomogram reconstruction. Tomograms were reconstructed at a pixel size of 15Å/px to enable manual virus picking using IMOD. The resulting particle centroids were used to extract subtomograms at a pixel size of 15Å/px using Warp. Subtomograms generated from Warp were then imported into RELION 3.1.2 to perform subtomogram averaging (STA) of virus particles. Virus maps were further improved through an iterative refinement M. Separately, reconstructed tomograms were segmented using EMAN2. The segmentation model was then used for further analysis to measure the distance between membrane and virus particles in UCSF ChimeraX.

2.11.1. WARP reconstruction of tilt series

The data processing pipeline was presented in Figure 2.1. Data were collected from the Titan Krios in MRC or Electron Event Representation (EER) format. Tilt series collected in EER format were gain-reference corrected and then motion corrected in RELION 4.(Scheres, 2012a, 2012b; Zivanov *et al.*, 2018; Kimanius *et al.*, 2021). These were then imported into WARP for reconstruction. Tilt series collected in MRC format were imported into WARP (Tegunov and Cramer, 2019) directly for processing. The contrast transfer function (CTF) and defocus were estimated in WARP for each tilt. The individual raw frames could be reviewed in WARP and outliers were deselected before proceeding to alignment in IMOD (Kremer, Mastronarde and McIntosh, 1996). Semi-automated IMOD alignment was performed using in-house python wrappers around IMOD function calls. Residual error and mean were tracked and refined to ≤1.5nm, if values were bigger than stated, raw frames were revisited and revised in WARP or tilt series were excluded for further processing. The alignments were imported into WARP for tomogram reconstruction. Tomograms were reconstructed at 15 Å/px.

Tomogram denoising was performed by splitting the tilt movie frames into even and odd sets during the pre-processing steps as inputs for training the denoiser program implemented in Warp (v.1.0.9). Denoising via Noise2Map.exe installed in the WARP directory uses the noise2noise (Lehtinen *et al.*, 2018) principle to train a denoising neural network. To execute the training process, folders containing half sets were specified, with a pixel size of 15Å, batch size of 16 and iterations value of 10000; additional parameters including -dont_flatten_spectrum and -

dont_augment were set. Denoised tomograms were then segmented in EMAN2 (please refer to section 2.11.3, Tang et al., 2007) and particles were manually picked from these tomograms in IMOD. This was followed by sub-tomogram averaging of ERAV particles (please refer to section 2.11.2.).

2.11.2. Sub-Tomogram averaging of ERAV particles

Virus particles were manually picked across several tomograms in IMOD. Particles were centred and manually picked. The coordinates were extracted and a STAR file containing this information was generated using a script provided by Dr Pranav Shah. Sub-tomograms were exported from WARP at pixel size 2.91Å. In RELION 3.1.2 (Scheres, 2012b, 2012a; Zivanov *et al.*, 2018), files containing coordinate information and a 3D reference model (PDB ID 1HXS) were imported into the programme. The algorithm requires an initial model that is strongly low-pass filtered in order to bootstrap the optimal orientation and translation parameters. Therefore, a similar sized poliovirus reference model was chosen due to its similar size to ERAV but also structurally distinct from it, thus minimising the chances of reference bias. The poliovirus model used was generated using a previously determined crystal-structure of poliovirus (PDB ID 1HXS; Miller, Hogle and Filman, 2001) using the molmap function in ChimeraX. The resulting map was resampled and reboxed to the sampling rate and box size of the ERAV subtomograms. In RELION, an initial round of 3D classification was performed to separate the manually picked particles into self-similar classes. Icosahedral symmetry was imposed at each iteration. Classification was performed for 40 iterations with T=0.1. 3D classification of assembling viral particles predominantly yielded two particle types which were subsequently refined using, in RELION 3.1.2, the gold-standard method of splitting the data into two independent half-sets.

Subsequently, the virus STA map from RELION was then imported into M for further refinement. Refinement was completed in a stepwise approach and improvement in the resolution was monitored at the end of each stage. The number of parameters to refine was iteratively increased as the resolution of the maps increased. Thus, refinement was started with 3 x 3 image warp grid, and particle poses, and then in each step of refinement, the following parameters were added respectively: stage angles, volume warp grid 3 x 3 x 2 x 10, then the following three parameters, anisotropic magnification, defocus, and grid search could be selected in the same round, eventually the range in image warp grid and volume warp grid could be increased.

2.11.3. Membrane segmentation using EMAN2

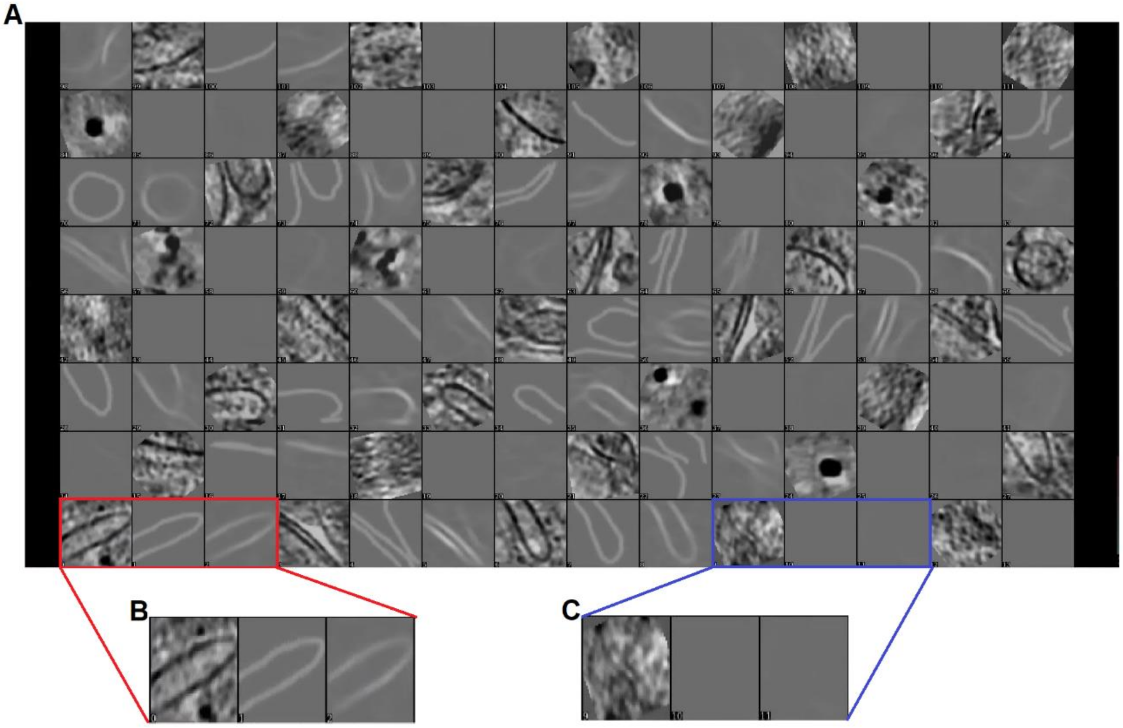

Figure 2.2 2D stack of training network in EMAN2.

This is an example of a neural network training to segment the tomogram. The red box highlights an example of membranes identified and blue box represents an example of non-membrane context identified of the training network (Magnified view in B and C). The left-hand panel represent 2D slices from the denoised tomogram, the middle panel represents the training, which is manual drawing over membranes, and the right-hand panel is the outcome from the training set, which is structures that the program identifies as a membrane.

In EMAN2 (Tang *et al.*, 2007; Chen *et al.*, 2017) only the segmentation function was used. Previously denoised tomograms (see section 2.11.1.), were used to segment membranes. Several batches of 2D slices from the tomograms were manually annotated to train the convolutional neural network in EMAN2 (Chen *et al.*, 2017). Training of the network was performed with default parameters. Following inference, the results of the training were manually compared on small patches of 2D slices (Figure 2.2) before segmenting the full volume.

2.11.4. Analysis of membrane structures and virus particles

In order to analyse the distance between the assembling virions and the membrane scaffolds they were opposed to, the denoised tomograms together with the segmented membranes generated from the previous step and the particle centres following refinement in RELION were imported and analysed in ChimeraX (Pettersen *et al.*, 2021). Distance measurements of the particle centres to the membranes were manually performed using the marker tool in ChimeraX.

Chapter 3 Recombinant FMDV for developing a CLEM system

3.1. Introduction

Correlative light and electron microscopy (CLEM) employs light and electron microscopy; the former provides spatial information, while the latter elucidates information at a higher resolution. CLEM correlates the imaging data from both types of microscopy allowing the detail of cellular ultrastructure revealed by EM to be overlaid onto fluorescent microscopy images showing the location of specific target proteins (Ellisman *et al.*, 2012). Hence, it means that CLEM is beneficial to users to have the best from both techniques providing more complete information to relevant biological question. The advantages of inserting live cell tags are that: (i) small tags were chosen to be inserted so there would be minimal interruption to the property of the protein of interest (ii) they are highly specific and enhances signal-to-noise ratio, reducing interference to data interpretation and analysis (iii) they enable *in vitro* study of the dynamics of proteins in cells and can be monitored over time using an appropriate microscopy method. In addition, if antibody is required for visualisation of viral proteins for light microscopy (LM), then fixation and/or permeabilisation of cells is necessary. Reagents such as fixatives have a detrimental effect in cellular structure which affects interpretation within EM analysis (as described in Chapter 1.7 and will also be discussed in Chapter 4). Therefore, inserting a live cell tag allows us to first localise the replication sites in LM, then correlate relevant information in EM. By utilising this approach, we aim to understand details of viral replication inside the cell such as the relationship between FMDV capsid assembly, viral proteins involved in replication and rearranged intracellular membranes.

The target for the CLEM signal is the FMDV 3A. This is a non-structural protein (nsp) that plays an important role in viral RNA (vRNA) replication and the host range of FMDV (reviewed in Jackson and Belsham, 2021). During replication, 3A is associated with membrane interactions and recruitment of other components of the replication machinery. FMDV utilises a slightly different mechanism for replication as compared to other picornaviruses. For example, FMDV 3A does not disrupt the endoplasmic reticulum (ER)-to-Golgi pathway (Moffat *et al.*, 2005b), whereas poliovirus 3A plays a role in diverting the membranes in the ER-to-Golgi pathway from forming replication complexes. Therefore, the association between this nsp and cellular membrane highlights its potential in investigating the connection between viral proteins and membrane rearrangement in cells via microscopy.

3A can influence host range by tolerating deletions, which reduces pathogenicity in cattle without affecting its replication in pigs (Li *et al.*, 2014). In addition, a site in the C-terminus of 3A, that can tolerate small insertions has been identified (Herod *et al.*, 2015). The identification of these sites, that tolerate genetic modification in 3A contributed to our design for the recombinant viruses with the insertion of different tags into 3A (Figure 3.1) for our microscopy study. The details will be explained later in this chapter.

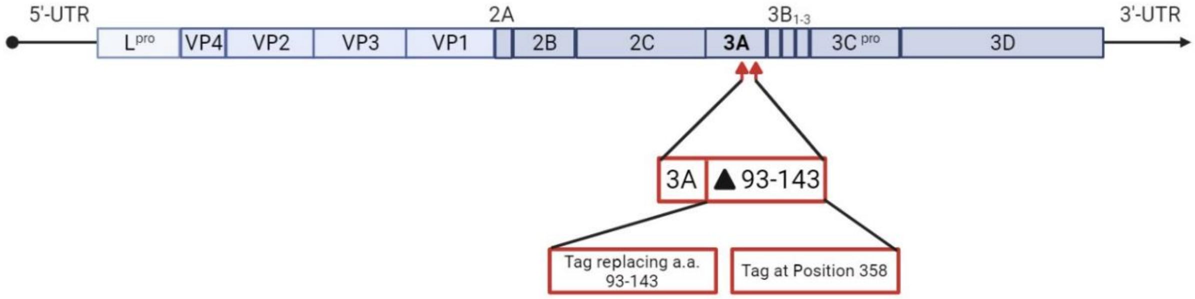

Figure 3.1 FMDV genome and site of tag insertion.

The red arrow indicates the two approaches used to insert tags into the 3A deleted region: (i) tags in 3A replacing amino acids 93-143 or at nucleotide position 358 (between amino acids 119 and 120) of full-length 3A. Created with Biorender.com

In-situ studies to localise viral proteins and protein-protein interactions utilize the genetic tagging of proteins to allow visualisation and localisation within the microscope. Three major groups of tags are i) short epitope tags, ii) split-green fluorescent protein (GFP), iii) tetracysteine (TC) and metallothionein tags. They will be introduced in more detail in the following section.

In this chapter, we will present the rationale for designing and recovering recombinant viruses that encode a tag. The functionality of these viruses will then be validated using confocal microscopy. Thus, recombinant viruses that preserve the tags and the capability to infect cells will then be used as a CLEM system to study FMDV replication.

3.2. Rationale and generation of FMDV 3A-tagged recombinant viruses

FMDV 3A co-localises with FMDV positive strand vRNA in cells (Berryman *et al.*, 2016) and has been previously used as a marker for sites of replication inside the cell. Previous studies have identified two sites in 3A that can tolerate modifications (Li *et al.*, 2014; Herod *et al.*, 2015), this led to our design of the site of deletion and the insertion sites for tags. The first position for insertion was between nucleotides 357 and 358 of the 3A coding region (Herod *et al.*, 2015). The second site was a naturally occurring deletion between amino acids 93 -143 (Li *et al.*, 2014) where a more sizeable insertion could more likely be tolerated. This deletion attenuates pathogenicity in cattle but has no effect on replication in hamster (e.g. BHK) or porcine (e.g. PK-15) cell lines used in this study. We employed an existing reverse genetics system to insert four major groups of tags into these two sites. These are all short tags thus maintaining the function and genome stability of 3A. They are designed for the development of a CLEM system, which is lacking, to study the replication of FMDV. The three major tags listed in Table 3.1 were chosen carefully to facilitate the development of a CLEM system.

Short epitope tags

Firstly, short epitope tags such as Haemagglutinin (HA) and FLAG tags have been commonly used to track recombinant proteins *in vitro* or *in vivo* (epitope tagging: General method). These distinct epitope sites within the peptide can be detected by commercially available antibodies. These short peptides are often used as tags at the N- or C-terminus of a protein where they are unlikely to affect the tertiary structure or biological activity of the protein of interest. These tags were successfully inserted into FMDV replicons (Herod *et al.*, 2015), and was shown to be tolerated by FMDV 3A. Therefore, was used as a starting point to generate recombinant viruses. Recombinant viruses encoding either of these tags can be used to co-infect cells providing an *in vitro* signal for the dynamics of replication sites. For example, a co-infection study using HA- or FLAG-tagged FMDV capsids was previously used to study the capsid compatibility and the dynamics of the tagged-capsid proteins in the infected cells (Childs *et al.*, 2021). Therefore, by infecting cells simultaneously with the two 3A-tagged FMDV, we can investigate the dynamics of replication sites derived from two different viruses within the same cell by confocal microscopy. If both tagged-3A proteins are detected in a single cell, it then suggests that replication of both recombinant viruses can occur in the same cell.

Tetracysteine and metallothionein tags

TC tags are small tags, with the size of 6 amino acids, that can be imaged in both light and electron microscopy. They bind the biarsenical atoms present in the staining reagents: green fluorescent FIAsH-EDT$_2$ reagent and red fluorescent ReAsH-EDT$_2$ reagent. To visualise biological details in EM, generating strong contrast for the intracellular structures within the biological sample is key to revealing high-resolution information about them. For many years, this contrast has been achieved by the addition of heavy metal atoms into samples. The usage of TC tags and a method known as diaminobenzidine (DAB) photo-oxidation allows the tag to be detected by electron microscopy. ReAsh can be precipitated by DAB and ultimately, the same sample can be used for both light and electron microscopes, which provides a coherent correlative system to analyse data from the same sample using both microscopes. Another metal-binding protein is metallothionein that binds to gold atoms which allows it to be visualised in EM (Diestra *et al.*, 2009; Chen *et al.*, 2014; Morphew *et al.*, 2015). However, the presence of heavy metals builds up toxicity levels in cells, hence is still not a universally used method for *in vivo* work. Viruses containing the tetracysteine and metallothionein tags were developed to directly visualise the tagged 3A protein by confocal (fluorescence) and EM (photo-oxidation) and to correlate the position of 3A in cells with rearranged membranes and assemble virus particles that can be subsequently visualised by EM.

Split GFP system

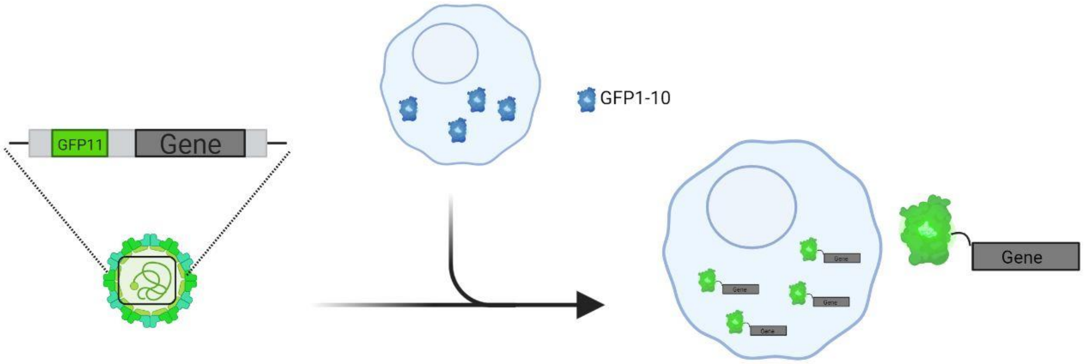

Figure 3.2 Schematic of split GFP system.

Gene of interest is tagged with GFP11. Cells are transduced or transfected with GFP1-10 plasmid. Upon complementation of the two fragments of GFP proteins recovers the fluorescence of the GFP protein.

GFP is a common tool in bioimaging and has been widely applied in different studies. In recent years, a split GFP system has become widely use to study protein-protein interactions. This system has then been extensively applied and improved over the past years and has eventually been used in virology research including studies on picornaviruses (Avilov *et al.*, 2012; Schaar *et al.*, 2016a). In brief, 11 β-strands constitute the GFP fluorophore. These 11 β-strands are split into two fragments; the first consists of the N-terminal 10 β-strands (GFP1-10) while the second encodes the C-terminal β-strand (GFP11). These two fragments can be supplied by separate systems within the cell and reconstituted upon proximity to become fluorescent.

The sequence encoding for full-length GFP is approximately 700 nucleotides. If this full-length GFP is inserted into the viral genome, it would impair its replication function as the genome packaging limit would be exceeded and the insertion will be removed by the virus (Seago *et al.*, 2013). Hence, we employed the split-GFP system. We inserted the GFP11 fragment, which is the last 15 amino acids of GFP, into FMDV 3A replacing residue 93 - 143. GFP1-10 was then expressed by PK-15 cells. Upon infection, the GFP fragments will bind and express green fluorescent signals that can be detected in the confocal microscope, representing FMDV 3A protein in infected cells (Figure 3.2). In our study, there are three versions of this 3A-GFP-tagged virus. They vary by the number of GFP11 fragments being inserted into 3A; from one to three copies. GFP1-10 is supplied by transient transfection of the plasmid or stable cell line expression of high levels of GFP1-10.

Table 3.1 List of recombinant viruses and their rationale.

FMDV constructs	**Amino Acid sequence**	**Rationale**
FMDV_3A_AscI	No tag	AscI site was added for ease of cloning tagged viruses
FMDV_3A_del_New_AscI	Deletion in amino acid 93-143 of 3A	3A deletion was introduced to allow the insertion of larger

		tags.
FMDV 3A_del_**FLAG** tag	DYKDDDDK	Co-infection experiment to investigate the dynamics of the replication site.
FMDV **FLAG** tag at Pos 358		
FMDV 3A_del_**HA** tag	YPYDVPDYA	
FMDV **HA** tag at Pos 358		
FMDV 3A_del_**tetracysteine**	CCPGCC	These tags can be directly visualised under EM. Therefore, it is beneficial towards the development of CLEM protocol to localise 3A in cells.
FMDV **Tetracysteine** tag at Pos 358		
FMDV 3A_del_**metallothionein** (not used)	PGGLAMDPNCSCSTGGSCTCTSSCACKNCKCTSCKKSCCSCCPVGCSKCAQGCVCKGAADKCTCCAAPR	
FMDV 3A_del_**metallothionein_tetracysteine**	PGGLAMDPNCSCSTGGSCTCTSSCACKNCKCTSCKKSCCSCCPVGCSKCAQGCVCK	

	GAADKCTCCAGGSGGCCPGCCAPR	
FMDV 3A_del_**1xGFP11**	PGGLARDHMVLHEYVNAAGITAPR	Our split GFP system enables us to localise 3A within the cell which provides a straightforward system for the development of a CLEM system to study the connection between viral non-structural protein and membrane rearrangement.
FMDV 3A_del_**2xGFP11**	PGGLARDHMVLHEYVNAAGITGGSGGRDHMVLHEYVNAAGITAPR	
FMDV 3A_del_**3xGFP11**	PGGLARDHMVLHEYVNAAGITGGSGGRDHMVLHEYVNAAGITGGSGGRDHMVLHEYVNAAGITAPR	

3.2.1. Tag insertion into FMDV genome using existing reverse genetics system

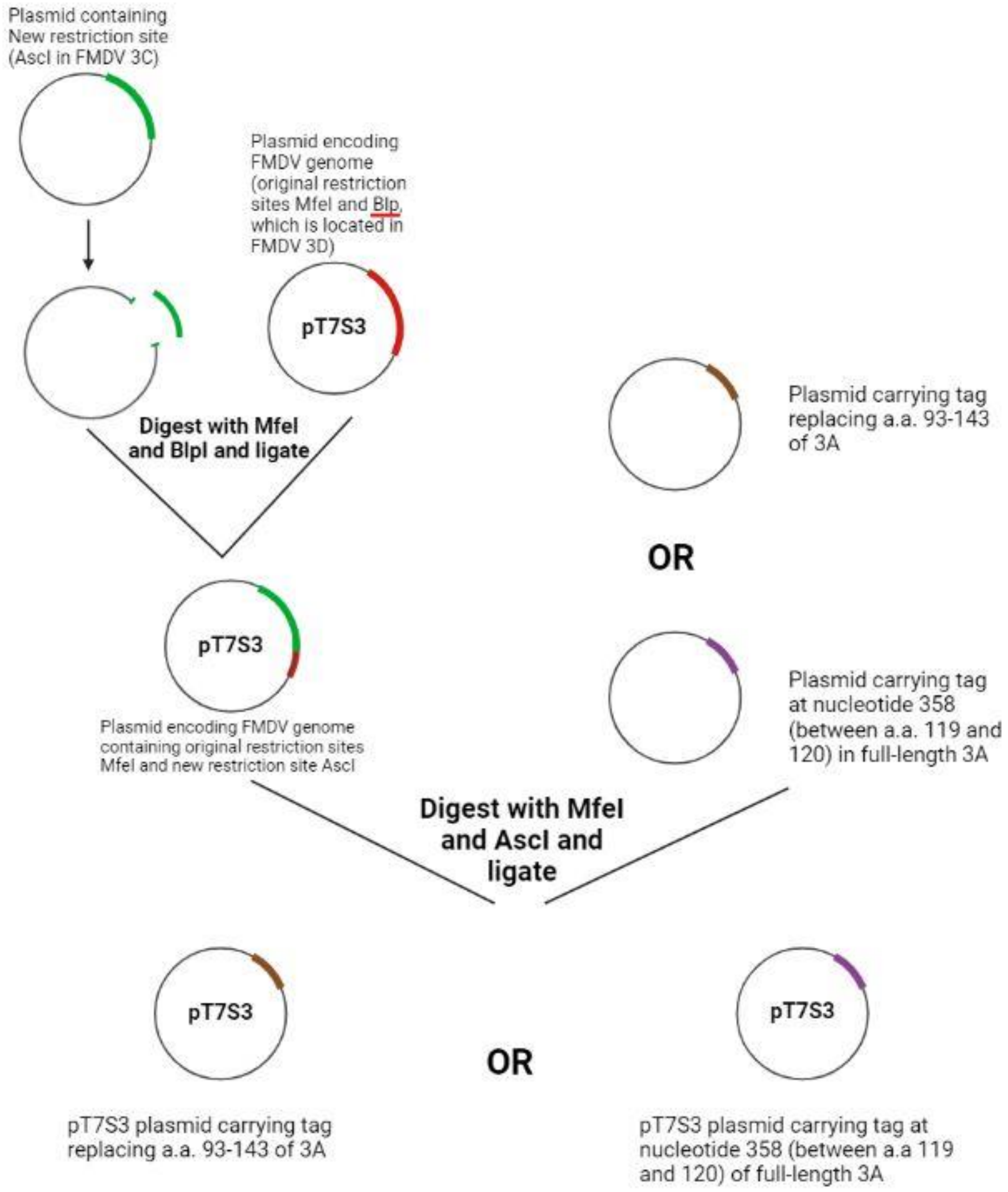

Figure 3.3 Schematic of two-stage cloning of FMDV 3A-tagged recombinant constructs.

A two-stage cloning of FMDV 3A-tagged recombinant constructs. pT7S3 plasmid encoding FMDV genome contains two original restriction sites MfeI and BlpI located in the regions coding for 3A and 3D respectively (red). The MfeI and BlpI restriction sites were used to introduce a new restriction site AscI in to the 3C coding region of pT7S3 using synthetic DNA ordered from GeneArt (green) covering the region from MfeI to BlpI. The MfeI and newly introduced AscI sites were then used to introduce a deletion of amino acids 93-143 of 3A, tags replacing amino acids 93-143, or tags inserted at nucleotide 358 (between amino acids 119 and 120) of full length 3A, using further synthetic DNA sequences ordered from Geneart.

We employed an existing and routinely used reverse genetics system for recovery of FMDV from a full-length infectious cDNA plasmid (Zibert *et al.*, 1990). Inserting tags into 3A required a multi-step cloning strategy. Plasmids containing our tags were designed and ordered from GeneArt. The original restriction sites in the infectious cDNA plasmid pT7S3 were MfeI and Blp1, which was used to introduce an AscI restriction site located in the region encoding FMDV 3C. The restriction sites, MfeI and AscI were then used to introduce tags replacing amino acid 93 - 143 of 3A, or tags inserted at nucleotide 358 of full length 3A (Figure 3.3). T7-driven RNA transcripts of plasmid constructs were generated *in vitro*. Subsequently, purified RNA was then transfected into BHK (hamster) cells. The transfection supernatant was then used to infect BHK cells. Viruses were passaged by infection (estimated MOI of 1 based on BHK titres) and development of cytopathic effect (CPE) in BHK cells was observed up to passage 10 (P10) after being recovered. CPE developed overnight across passages. Wildtype FMDV with the additional AscI site introduced was recovered simultaneously and viruses with 3A tag behaved similarly to the wildtype virus, displaying a similar time to onset CPE.

3.2.2. Recombinant viruses are genetically stable

In the two-stage cloning system described in the above section, changes to the virus sequence can be introduced by standard DNA cloning approaches. In order to validate that the tags were preserved after we recovered and passaged the viruses, we sequenced the virus at P3, which was the working stock for all subsequent studies and also at P5 and P10 to check that the introduced tags were stably maintained. We found no sequence changes in any of the recovered viruses described above, suggesting that the viruses were viable and genetically stable up to P10. This then led us to the next section on further evaluation of their functionality using confocal microscopy. The titre of viruses recovered was measured. The titre of all recombinant viruses was measured in BHK cells. As mentioned earlier in the chapter, FMDV with a 3A deletion was shown to be functional in replication in porcine cells. Hence, for further characterisation of the viruses we intend to use, the titre of viruses was measured in porcine (PK-15) cells (Table 3.3, see section 3.3.4). The titre of recombinant viruses appeared to be within the same range as FMDV wildtype viruses between 10^6 to 10^7 in BHK cells except for recombinant viruses containing the tetracysteine tags which was slightly lower at 10^5 which was still within an acceptable range (Table 3.2). Nevertheless, this suggested that the replication of the recombinant viruses was not affected.

Table 3.2 List of virus titre in Baby Hamster (BHK) cells.

Site of insertion	Virus	Cell type	Titre	Replicate
	FMDV Wildtype with AscI restriction site	BHK	1.5×10^6	One
FMDV 3A deletion at residues 93-143	FMDV_3A_del_93-143	BHK	2.3×10^7	
	FMDV 3A_del_HA	BHK	2.5×10^6	
	FMDV_3A_del_FLAG	BHK	1.25×10^7	
	FMDV_3A_del_1xGFP11	BHK	1.95×10^6	
	FMDV_3A_del_2xGFP11	BHK	3.7×10^6	
	FMDV_3A_del_3xGFP11	BHK	1.95×10^6	
	FMDV_3A_del_Tetracysteine	BHK	1×10^5	
	FMDV_3A_del_metallothionein	BHK	5.5×10^5	
	FMDV_3A_del_tetracysteine-metallothionein	BHK	7×10^5	
Tagged at FMDV 3A Position 358	FMDV_3A_Tetracysteine_Pos_358	BHK	3.5×10^5	
	FMDV_3A_HA_Pos_358	BHK	2.35×10^6	
	FMDV_3A_FLAG_Pos_358	BHK	3.6×10^6	

3.3. Characterising recombinant viruses by light microscopy

Sequencing results showed that no mutations occurred during passage and that the tagged viruses were genetically stable. We then wanted to characterise these viruses and confirm that the tags are functional using confocal microscopy. We infected PK-15 (porcine) cells or SK-RST cells, which was first thought to be porcine cells but later revealed to be hamster cells (as explained in Chapter 2.2.), to validate the functionality of the recovered 3A-tagged viruses. Infected cells were immunolabelled with the respective antibody. In the case of a split GFP system, cells were either transiently transfected with GFP1-10 or by infecting a stable PK-15 cell line that constitutively expresses GFP1-10, which requires no further immunolabelling. Initially we used an anti-3A monoclonal (2C2; De Diego et al., 1997) to confirm infectivity. However, this did not recognise our recombinant viruses and as such we switched to using an antibody that detects the FMDV capsid, IB11 (Juleff *et al.*, 2008). This suggests that the 2C2 epitope site was disrupted by our deletion or insertion of tag in 3A. We then constructed a pilot study to characterise our recombinant viruses using confocal microscopy. MOI used to infect cells were empirically estimated, based on BHK titres, to infect a reasonable proportion of cells to be analysed in confocal and further confirm the timepoint post infection used in this study. We are presenting data at 3.5hpi, which is known in our lab to be the peak infection timepoint where replication of viral proteins is active and most 3A protein can be captured. We expected to see strong and distinct signals for any functional 3A-tagged viruses. For final characterisation of viruses, we intended to use for subsequent experiments, we titrated them in PK-15 cells.

3.3.1. Short epitope tags

As described in section 3.2.1., there were two ways we inserted the epitope tags to generate recombinant viruses; where tags were replacing amino acid 93-143 of 3A (FMDV 3A_del_HA and FMDV_3A_del_FLAG) or tagged at position 358 of full-length 3A (FMDV_3A_HA_Pos358 and FMDV_3A_FLAG_Pos358). SK-RST cells were infected with wildtype, FMDV_3A_del_HA and FMDV_HA_Pos358 respectively. Infected cells were fixed at 3.5 hours post infection, labelled with 2C2 against FMDV 3A, and analysed by confocal microscopy. SK-RST infected with wildtype FMDV fixed at 3.5hpi and labelled with 2C2 showed a strong positive signal in the cytoplasmic region indicating cells were infected. Noise signals was high in uninfected cells, nevertheless positive signals were distinguishable but individual puncta could not be easily identified (Figure 3.4A). Positive signals were not observed in cells infected with FMDV_3A_del_HA (Figure 3.4B). Weak 3A puncta, labelled with 2C2, were observed in cells infected with FMDV_HA_Pos358. 3A puncta could be seen in the cytoplasmic region (Figure 3.4C). Cells infected with FMDV_3A_del_HA and FMDV_HA_Pos358 were fixed at 3.5hpi and labelled with anti-HA antibodies. HA-tagged viruses replicated as expected in terms of intensity and localisation of 3A signal where puncta were distributed across the cytoplasm (Figure 3.5A and B). Since 2C2 was not recognising FMDV 3A as expected, this suggested to us that the epitope site for 2C2 was potentially disrupted. Hence, this antibody was not used for subsequent experiment.

SK-RST cells were also infected with FMDV_3A_del_FLAG and FMDV_3A_FLAG_Pos358 and fixed at 3.5h post infection. Cells were then labelled with anti-FLAG antibodies and analysed by confocal microscopy. FLAG-tagged viruses also replicated as expected in terms of intensity and localisation of 3A signal where puncta appear abundant in the cytoplasm (Figure 3.5C and D). These recombinant viruses showed a similar pattern of labelling in the cytoplasm of the infected cells as wild type FMDV and showed that these tagged viruses were viable and functional.

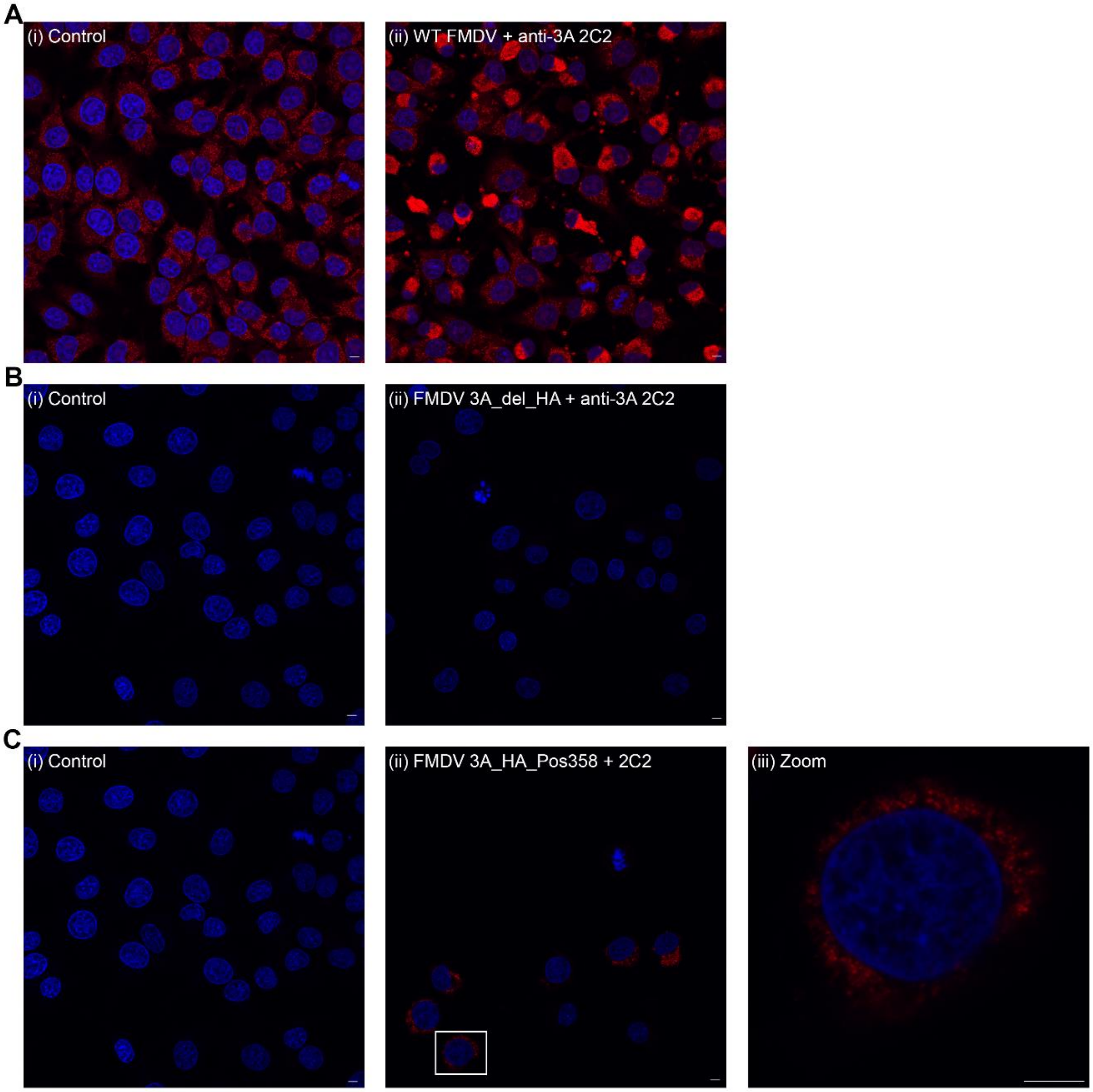

Figure 3.4 SK-RST cells infected with FMDV wildtype and 3A-HA tagged virus immunolabelled with anti-3A (2C2).

A(i), B(i) and C(i) are uninfected cells. Nuclei stained with DAPI (blue). **A(ii)** presents SK-RST cells infected with wildtype FMDV fixed at 3.5hpi and immunolabelled with anti-3A 2C2 (red). Although the noise signal is high, positive signals are distinguishable where red fluorescent signals are seen in the cytoplasm region. SK-RST cells were infected with **B(ii)** FMDV 3A_del_HA and **C(ii) + (iii)** FMDV 3A_Ha_Pos358. Cells were fixed at 3.5hpi and immunolabelled with 2C2. No positive signals are detected in cells infected with FMDV 3A_del_HA. Weak 3A puncta are detected in cells infected with FMDV 3A_HA_Pos358 in the perinuclear region. (All scale bar = 5 μm)

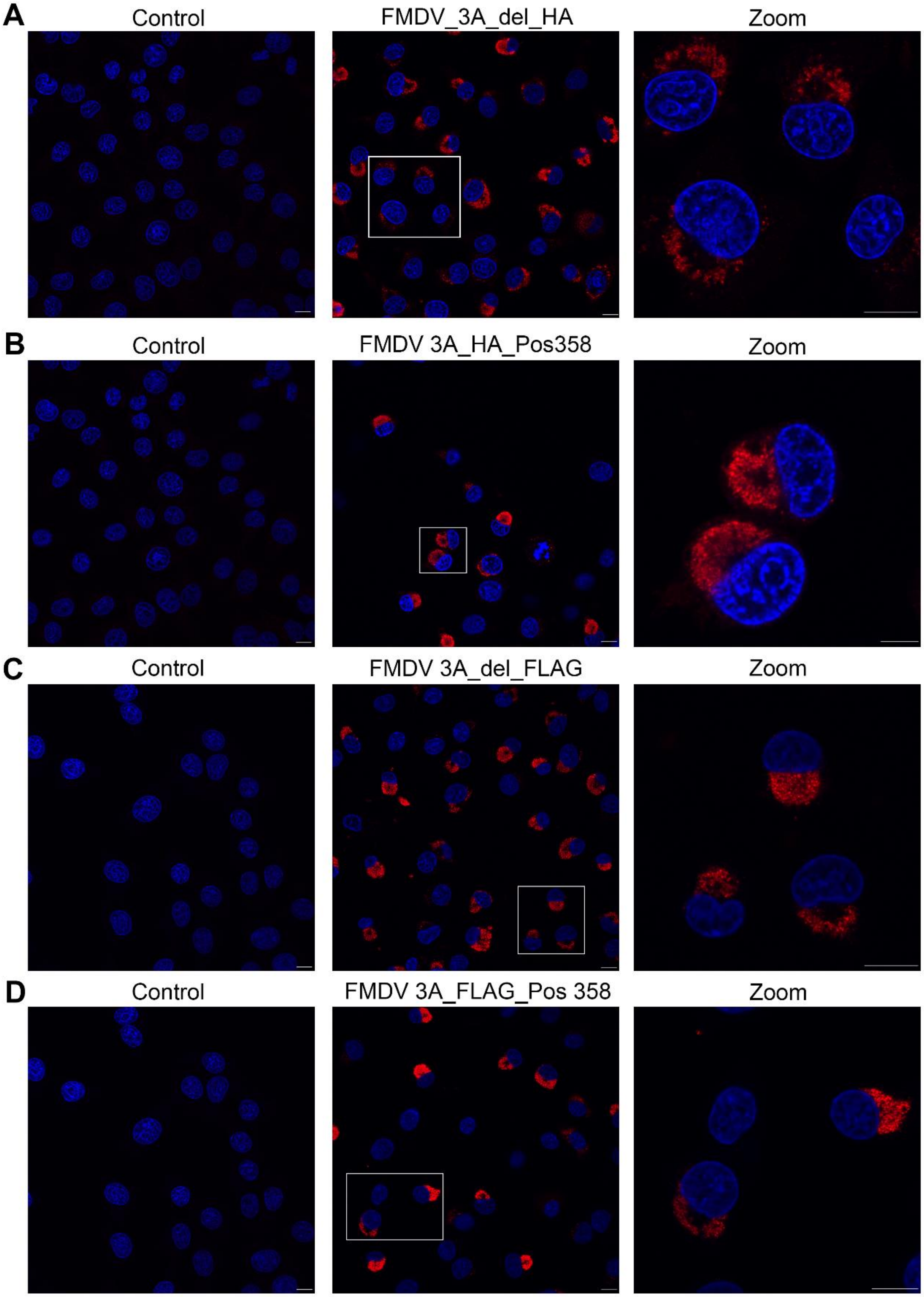

Figure 3.5 Characterisation of 3A-short epitope tagged FMDV.

All the left-hand panels are uninfected controls. Nuclei were stained with DAPI (blue). SK-RST cells infected with **(A)** FMDV_3A_del_HA, **(B)** FMDV_3A_HA_Pos358, **(C)** FMDV_3A_del_FLAG and **(D)** FMDV_3A_FLAG_Pos358 respectively. Infected cells were fixed at 3.5h post infection. Cells infected with 3A-HA tagged FMDV (**A** and **B**) were immunolabelled with anti-HA primary antibody. 3A puncta (red) are distinct in infected cells and appear abundantly in the cytoplasm. Cells infected with 3A-FLAG tagged FMDV were immunolabelled with anti-FLAG primary antibodies. Cytoplasmic puncta are observed in infected cells. Both 3A-HA and 3A-FLAG tagged FMDV shows a similar 3A pattern in the cytoplasm. (All scale bar = 5 μm)

3.3.2. Tetracysteine and metallothionein tags

Our recombinant viruses contain a 3A deletion where tags are inserted therefore, the porcine cell line was preferred over other cell lines, as this deletion does not affect replication in porcine cells (as explained in section 3.2). Hence, when the SK-RST cells we used were found to be hamster cells, as discussed in Chapter 2.2., we changed to PK-15 cells, which is a porcine cell line, for subsequent experiments. ReAsh, a biarsenical reagent that binds to the TC motif is used to stain our TC-tagged 3A FMDV for visualisation in the confocal microscope.

PK-15 cells were infected with FMDV_3A_del_Tetracysteine and FMDV_3A_Tetracysteine_Pos358 respectively. Cells were then fixed at 3.5h post infection. An example of PK-15 cells infected with FMDV_3A_del_Tetracysteine showed strong 3A signals where puncta appeared to cluster (Figure 3.6A; zoomed panel). Otherwise, most cells presented 3A puncta that was distributed sparsely across the cytoplasm (Figure 3.6). Cells infected with FMDV_3A_Tetracysteine_Pos358 showed a similar pattern where 3A puncta were spread across the whole cytoplasmic area. In our infected cells, we could see the nucleus aligned with 3A puncta, filling up the perinuclear region, at this timepoint, we can also see an abundant amount of 3A signals distributed across the cytoplasm (Figure 3.6B, zoomed panel).

PK-15 cells were infected with FMDV_3A_del_metallothionein_tetracysteine and fixed at 3.5h post infection. Infected cells were either stained using the TC ReAsh kit or immunolabelled using anti-FMDV capsid, IB11 (Juleff *et al.*, 2008). There were very few strong 3A puncta observed in infected cells stained with TC ReAsh kit, most puncta were weak and not as distinguishable due to high background noise (Figure 3.7A). Therefore, infected cells were immunolabelled with mAb IB11 which allowed us to confirm the infectivity of this virus. Red puncta representing FMDV capsid was observed in cells. Although the noise is high, the positive signals were distinct and strong puncta were observed easily in the cytoplasm (Figure 3.7B). As expected, these results collectively showed that this recombinant virus was able to infect cells and was functional (Figure 3.8). However, the lack of labelling with the TC ReAsh kit suggested that the presence of metallothionein tag potentially disrupted accessibility to the TC ReAsh stain. Since, the dual-tagged recombinant virus was not functioning as well as expected, it was therefore not used in subsequent experiments.

The last recombinant virus in this category is 3A_del_metallothionein-tagged FMDV. This virus was not used as it could only be visualised by EM and therefore not tested. In addition, its toxicity towards cells has previously been reported (Bouchet-Marquis *et al.*, 2012). However, they are genetically stable and functional and thus can be further investigated in their potential use for CLEM studies.

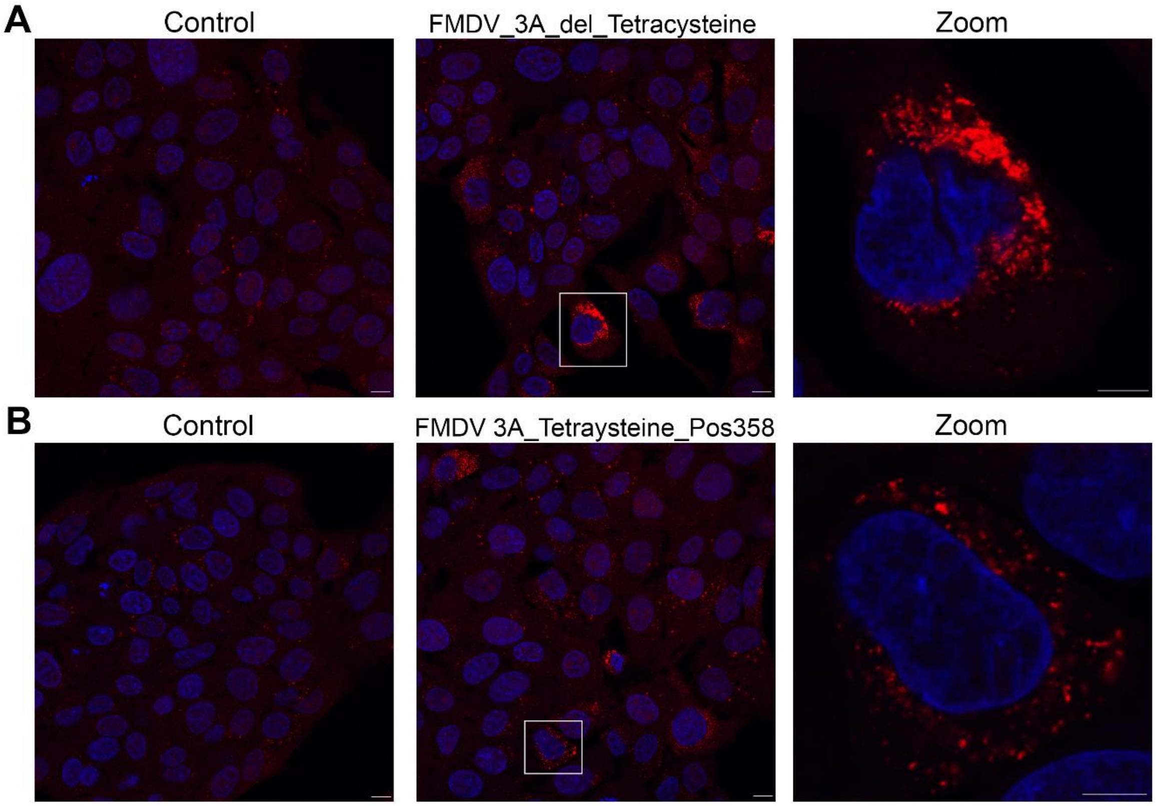

Figure 3.6 Characterisation of 3A-tetracysteine tagged FMDV.

Uninfected controls are shown in left hand panels. Nuclei were stained with DAPI (blue). **(A)** PK-15 infected with FMDV_3A_del_Tetracysteine stained with ReAsh detection kit and fixed at 3.5h post infection. The Zoom panel shows an example of an infected cell with strong 3A puncta, some are in clusters that appear mainly in the perinuclear region. **(B)** PK-15 cells infected with FMDV_3A_Tetracysteine_Pos358 fixed at 3.5h post infection. Infected cells were stained with ReAsh detection kit. 3A puncta are spread across the cytoplasm. (Scale bar = 10 μm, zoom = 5um)

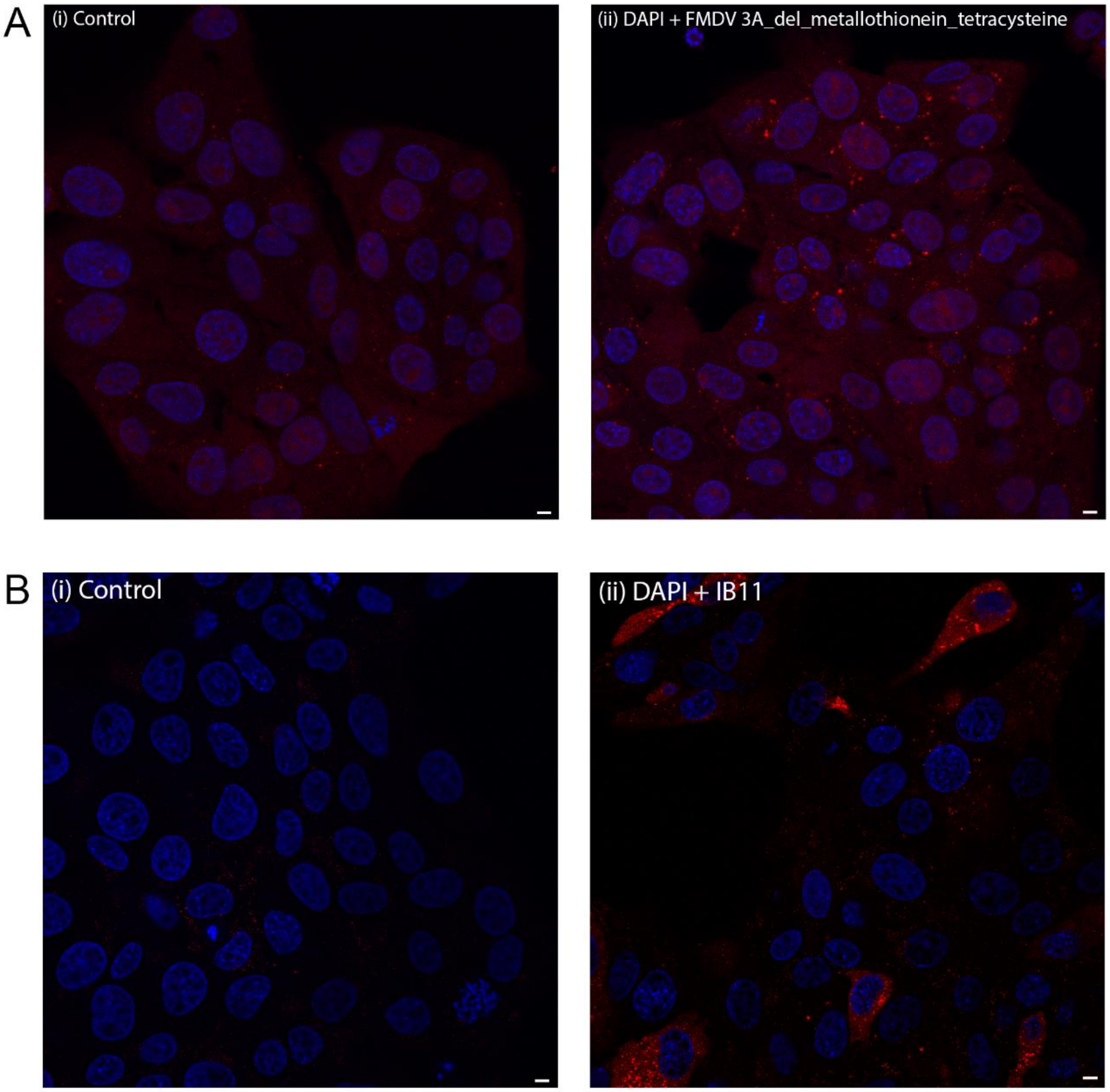

Figure 3.7 Characterisation of 3A-metallothionein-tetracysteine tagged FMDV.

Uninfected controls cells are presented in the left-hand panels (**A(i)** and **B(i)**). Nuclei stained with DAPI (blue). **(A)** PK-15 cells infected with FMDV_3A_del_metallothionein_tetracysteine stained with ReAsh detection kit and fixed at 3.5h post infection. There are few strong 3A puncta and most are not distinguishable due to high background noise. **(B)** PK-15 cells infected with FMDV_3A_del_metallothionein_tetracysteine fixed at 3.5h post infection. Cells were immunolabelled with mAb IB11 which stains FMDV capsid that confirms infectivity. (Scale bar = 5 μm)

3.3.3. Split-GFP system

Obtaining optimal conditions for this system was essential, therefore we developed and compared two different systems: transient transfection of GFP1-10 into cells and a stable cell line expressing GFP1-10. This stably expressing GFP1-10 cell line was produced in our lab from transduction of PK-15 cells with express GFP1-10 (refer to PK-15 GFP1-10 cells hereafter). These cells were bulk sorted by FACS to isolate the cells that express the highest levels of GFP1-10. We also explored transient transfection of the GFP1-10 plasmid into cells. This approach gave a visibly stronger 3A-GFP signal in cells with the 3A-GFP11-tagged viruses. Transiently transfected cells gave stronger signals and better results, although this was limited by the transfection efficiency, therefore the proportion of cells within the population that express GFP signals vary between experiments. Nevertheless, we concluded that transient transfection would be used for further work with the aim to study FMDV replication, as we could see 3A signals more easily.

We then compared the three versions of recombinant FMDV containing GFP11. PK-15 GFP1-10 cells were infected with viruses containing 1, 2, or 3 copies of the GFP11 tag inserted into 3A. We infected cells with FMDV_3A_del_1xGFP11, FMDV_3A_del_2xGFP11 and FMDV_3A_del_3xGFP11 respectively. Cells were then fixed at 3.5 hours post infection. Strong 3A signals were observed in all three versions of 3A-GFP11-tagged infected cells. FMDV_3A_del_1xGFP11 cells showed that 3A puncta clusters were seen in the cytoplasmic region. 3A signals were sparsely distributed in cells but not all cells were expressing 3A signals as again this could be affected by the low transfection efficiency and low infectivity of GFP11 (Figure 3.8A). FMDV 3A_del_2xGFP11 showed strong and distinct puncta where individual puncta could be identified clearly. 3A puncta appeared more abundant in the cytoplasm (Figure 3.8B). FMDV_3A_del_1xGFP11 and FMDV 3A_del_3xGFP11 infected cells showed a relatively similar pattern with reasonable intensity puncta that were mostly seen in clusters. 3A clusters appeared to be more abundant and distinct in FMDV 3A_del_3xGFP11 infected cells (Figure 3.8C). We were concerned that three copies of GFP11 fragments in 3A may exceed the packaging limit and two copies of GFP11 could be better tolerated by the virus. Hence, FMDV 3A with two copies of GFP11 fragments (FMDV_3A_2xGFP11) was chosen to be used in subsequent experiments as it gives the most reasonable 3A pattern that is comparable to other tagged viruses and to wild type infections.

We then investigated the time course of 3A signal to further characterise the 3A_del_2xGFP11 tagged virus. PK-15 cells were transfected with GFP1-10 plasmid prior to infection, cells were then infected for 4.5h with cells fixed at three different timepoints. GFP signals were strong and distinct at 3.5hpi with little strong GFP signals at 2.5hrs post infection. This was expected as 3.5hpi is the peak replication timepoint where 3A should be highly expressed in cells. 2.5hpi showed a weaker signal suggesting it was still early during the replication cycle whereas infected cells at 4.5hpi were potentially undergoing cytopathic effect. This could be due to the low infection rate and hence most cells that were infected have rounded up and lifted from the coverslips leaving cells behind that potentially were infected by virus particles released from lysed cells. This suggested that the replication cycle of the recombinant FMDV in cells is rapid and remains consistent across our experiments with the wild type viruses, reassuring us that we chose the correct timepoint for our study (Figure 3.9).

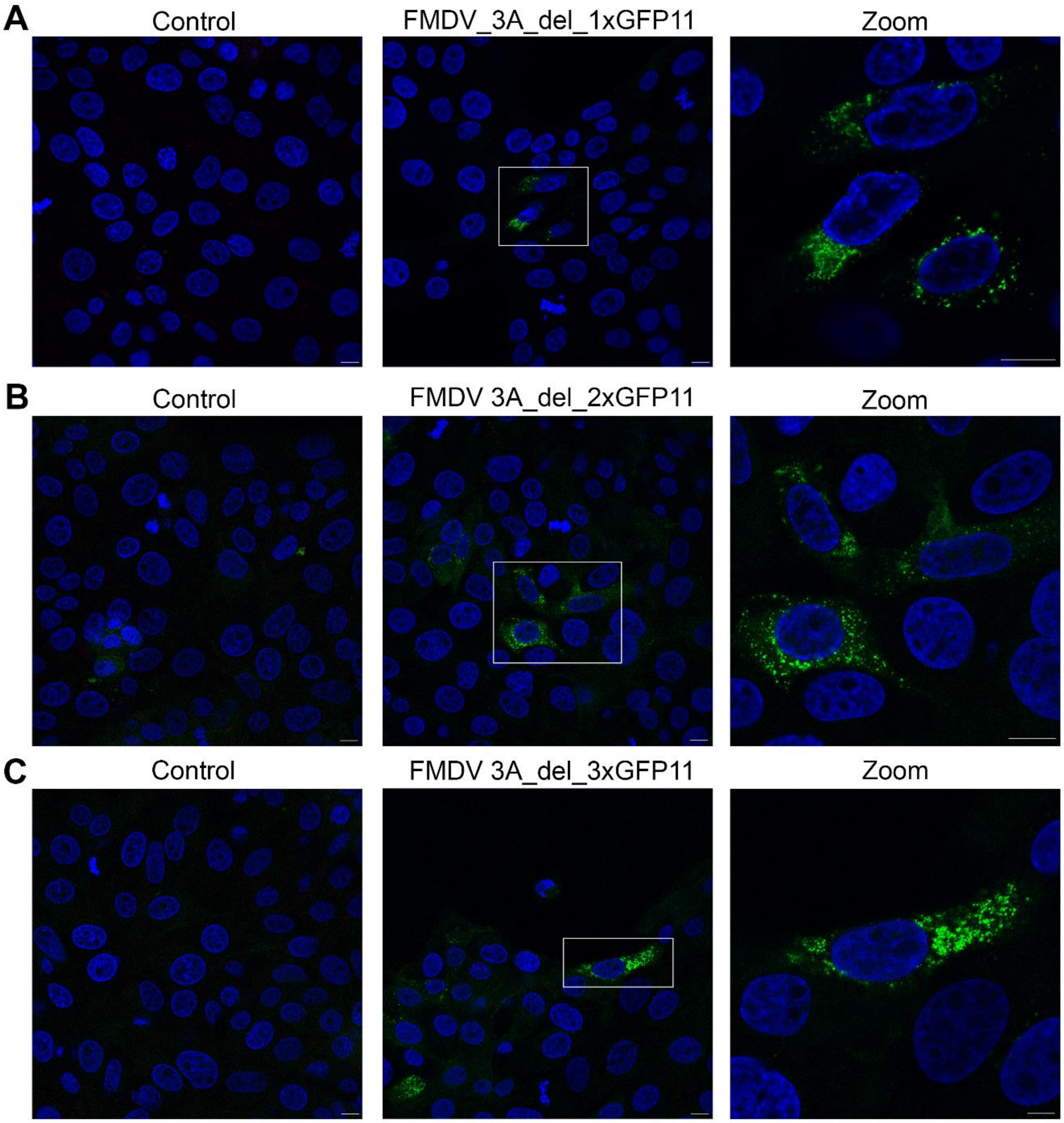

Figure 3.8 Characterisation of 3A-GFP11 tagged FMDV.

FMDV infected PK-15 GFP1-10 cells fixed at 3.5hpi. Uninfected cells are presented in left hand panels. Nuclei stained with DAPI (blue). This figure shows the three split GFP system of 3A-GFP tagged FMDV. PK-15 cells infected with **(A)** FMDV_3A_del_1xGFP11, **(B)** FMDV_3A_del_2xGFP11 and **(C)** FMDV_3A_del_3xGFP11 respectively. In the zoom panels, the 3A (green) GFP puncta pattern is shown more clearly.

FMDV_3A_del_1xGFP11 infected PK-15 shows that 3A signals appeared to be spread sparsely from the perinuclear region, with the middle cell showing 3A puncta in clusters. FMDV_3A_del_2xGFP11 infected PK-15 shows a clear pattern of 3A puncta that can be detected individually and are abundant across the cytoplasm. Puncta aligning the nucleus appear to be strongest and individual puncta is distinct. FMDV 3A_del_3xGFP11 infected PK-15 cells show a pattern that is similar to FMDV_3A_del_1xGFP11, however with puncta in smaller clusters and more abundant throughout the whole cytoplasm. (Scale bar = 5 μm)

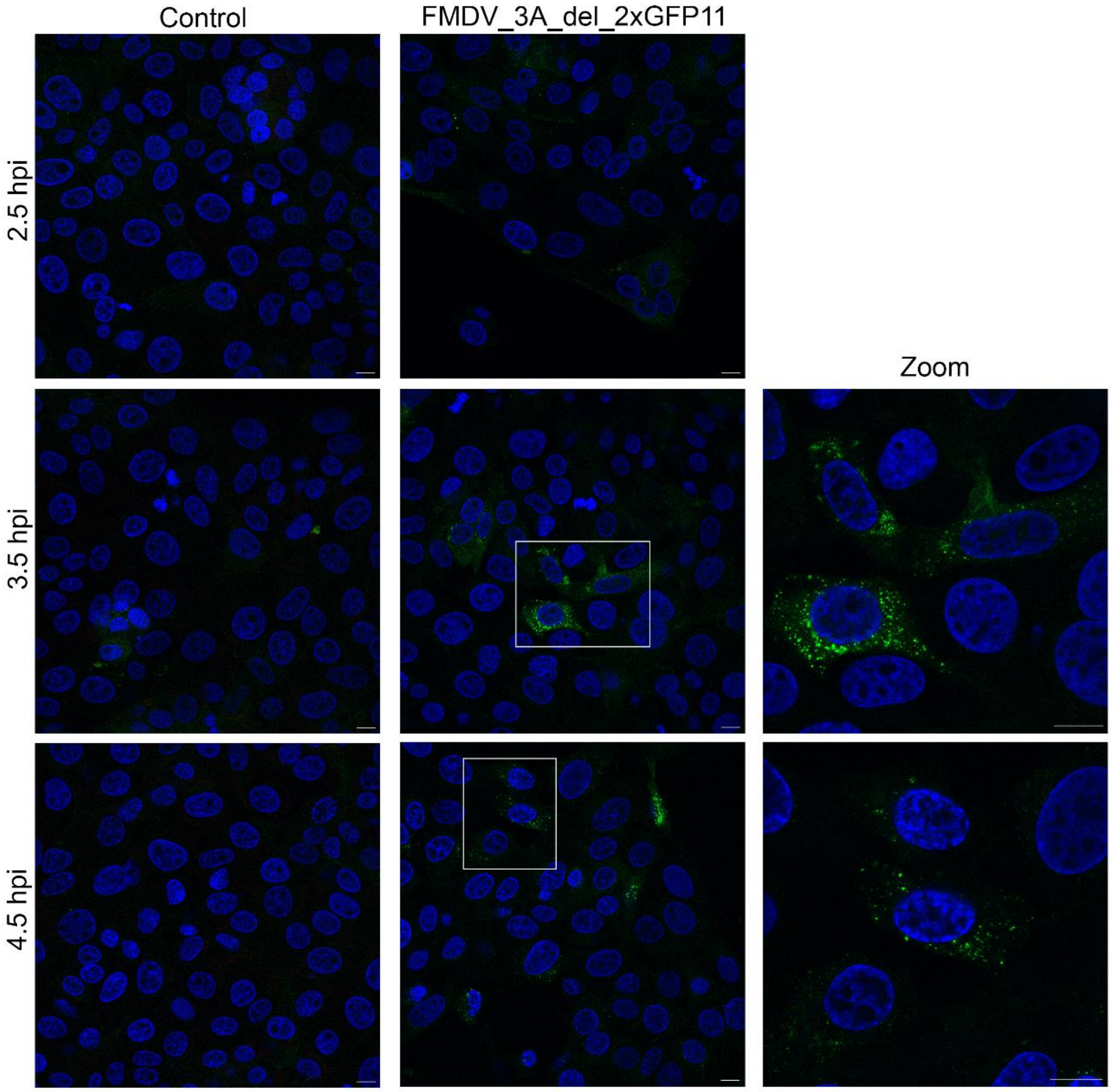

Figure 3.9 Time course of FMDV_3A_del_2xGFP11.

PK-15 GFP1-10 cells infected with FMDV 3A_2xGFP11 fixed at 2.5h, 3.5h and 4.5h post infection. Very few 3A (green) puncta appear at 2.5hpi. Signals also appear to be very weak. At 3.5hpi, stronger and abundant 3A puncta are detected. Signals are distributed across the cytoplasm with a few strong 3A puncta appearing next to the nucleus. At 4.5hpi, individual 3A puncta are detected in cells, however there are fewer 3A sites. Uninfected cells are presented in left hand panels. Nuclei stained with DAPI (blue). (Scale bar = 5 μm)

3.3.4. Comparing replication of FMDV WT and FMDV_3A_del_2xGFP11

Table 3.3 List of virus titre in porcine (PK-15) cells.

Site of insertion	Virus	Cell type	Titre	Replicate
3A deletion at residues 93-143	FMDV wildtype with AscI restriction site	PK-15	4.05 x 10^7	One
	FMDV_3A_del_1xGFP11	PK-15	7.2 x 10^6	
	FMDV_3A_del_2xGFP11	PK-15	5.2 x 10^6	
	FMDV_3A_del_3xGFP11	PK-15	1.7 x 10^7	
	FMDV_3A_del_Tetracysteine	PK-15	1.75 x 10^7	
	FMDV_3A_del_metallothionein_tetracysteine	PK-15	5.5 x 10^6	

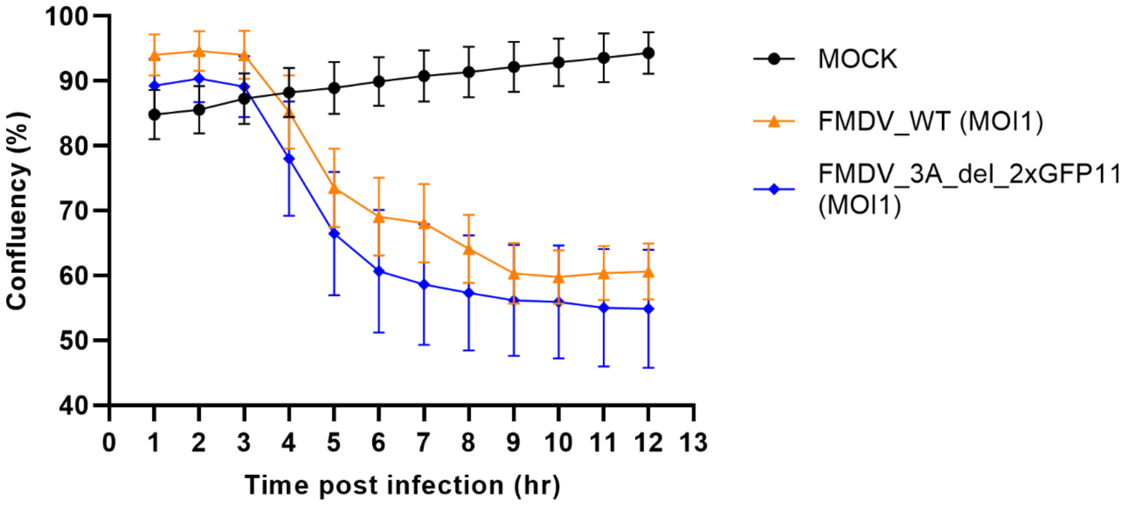

Figure 3.10 Cell killing assay of FMDV wildtype and FMDV 3A_del_2xGFP11.

Replication of FMDV WT (Orange) and FMDV_3A_del_2xGFP11 (Blue) based on cytopathic effect (CPE). We compared the replication of the two viruses based on development of CPE to ensure no significant reduction in replication was caused by deletion. PK-15 cells were infected with either virus at MOI 1 in technical triplicates. Confluency of cells in 96 well plates was recorded on Incucyte. FMDV_3A_del_2xGFP11 cause a slight reduction in replication but it is still very similar to WT FMDV replication. During the exponential phase, 3.5hpi is considered the peak replication timepoint as full CPE is reached at approximately 5hpi. Earlier timepoints show little or no CPE suggesting it is still early during replication inside cells.

GFP11 and WT viruses induce CPE at the same rate. This was observed through serial passage of the recombinant viruses where CPE was observed overnight when infected with WT or 3A-tagged recombinant FMDV. For our final characterisation of our recombinant viruses, the virus titre we intended to use for subsequent experiments was measured in PK-15 cells. The virus titre in both BHK cells (Table 3.2, see section 3.2.2) and PK-15 (Table 3.3) cells fell within the range of WT FMDV between 10^6 to 10^7, hence this was consistent with our observation of CPE development. However, to further confirm that the deletion of the tag insertion does not cause a significant change affecting 3A's function, and FMDV replication, we ran another experiment to monitor the CPE over 12 hours post-infection. We then analysed the confluency of the cells over time using MOI1 (Figure 3.10). Earlier timepoints showed little or no CPE suggesting that it was still early in the replication cycle, we started to see CPE after 3hpi. A plateau started between 5 and 6hpi which suggested that these were timepoints that were quite late during the replication and cells lysis in response to releasing viruses in the media. Therefore, we will not be able to study much of the replication details at those late timepoints. In summary, 3.5hpi was the timepoint where optimal replication was happening that enables us to localise most abundant number of 3A foci in cells. Combining this with results earlier in the chapter, where we saw strong abundant 3A (GFP) signals at 3.5hpi in FMDV infected cells, this suggested to us that it was the optimal replication timepoint. This led us to start the development of a CLEM system in the next section, using conditions optimised earlier in the chapter.

3.4. Golgi membrane signals appear close to but do not co-localise with FMDV 3A signals

Our aim to produce recombinant virus was to aid in the development of the CLEM system for aphthoviruses. In addition to CLEM signals localising viral proteins, we wanted to explore the possibility in developing CLEM system labelling intracellular membrane compartments. Hence, after the optimisation of the split-GFP system described in section 3.3.3., we started to look at membrane trackers. The rationale was that direct labelling of membranes would allow us to potentially elucidate sources of membranes that form ROs in LM, which subsequently enable us to identify these structures in EM. This is due to virus particles not being visible in conventional/RT EM as chemical fixation dissociates the FMDV capsid. Therefore, the aim of developing a CLEM system is to look for replication sites (3A) and identifiable structures in both confocal and EM. In our study, we were targeting membranes that interact with FMDV 3A. Positive strand RNA viruses will induce ultrastructural changes in the host cell membranes, in which the rearranged membranes are recruited to the replication platform where RNA synthesis takes place. Since Golgi and ER play a key role in protein synthesis in cells, we therefore investigated the use of two different membrane dyes; ER tracker and BODIPY TR ceramide, which is referred to as Golgi tracker hereafter.

PK-15 cells were transfected with GFP1-10 plasmid and were then infected with FMDV_3A_del_2xGFP11 and fixed at 3.5hpi. There were no ER tracker (red) signals observed. 3A-GFP11 (green) puncta were seen easily in infected cells (Figure 3.11). We then discovered that membrane permeabilization is not required by ER tracker as lipids might be extracted by triton permeabilization. As part of troubleshooting the protocol, we were also concerned that different buffers may affect the ER tracker signal, therefore we repeated the experiment using various reagents ranging from HBSS to serum-free DMEM to dilute ER tracker. ER tracker signals (red) was seen following these condition-optimising experiments proving that this ER tracker was useable with our infected cells. Nevertheless, the signals were not as strong as Golgi membrane markers, and connections between 3A ER membranes were not observed (Figure 3.12). Contrary to this, the Golgi tracker showed a more distinct pattern. PK-15 cells were transfected with GFP1-10 plasmids and infected with FMDV_3A_del_2xGFP11, infected cells were then fixed at 3.5hpi. 3A-GFP11 (green) puncta appear adjacent to the Golgi tracker (red) signals in infected cells (Figure 3.13). We did not see a high proportion of cells that expressed both the Golgi membrane tracker and the 3A-GFP signals. However, we believed that this is affected and dependent on two factors: firstly, GFP1-10 transfection rate in cells. We were unsure if all cells were transfected with GFP1-10, and which population of cells were expressing high levels of GFP1-10. We believed that following the protocol used in validation should be sufficient to transfect a reasonable proportion of cells. Secondly, the Golgi tracker signals was not observed in all cells which means that not all cells were stained. We have seen, within the same population of cells, some were expressing GFP1-10 only, as 3A-GFP signals was seen lacking the Golgi tracker signals, or vice versa. There were also small proportion of cells that had clearly shown that they do not express both GFP and Golgi signals. Therefore, potentially suggesting to us that, this protocol should potentially be further optimised. Or if a stable cell line expressing GFP1-10 was generated and used instead of transfection potentially resolve part of this issue. No colocalisation between the GFP and Golgi signals was observed. This suggested that replication sites appear next to the Golgi and Golgi membranes potentially serves as a membranes source for FMDV replication. Also, use of Golgi tracker was relatively straightforward, and would be recommended for future development of CLEM system to study FMDV replication.

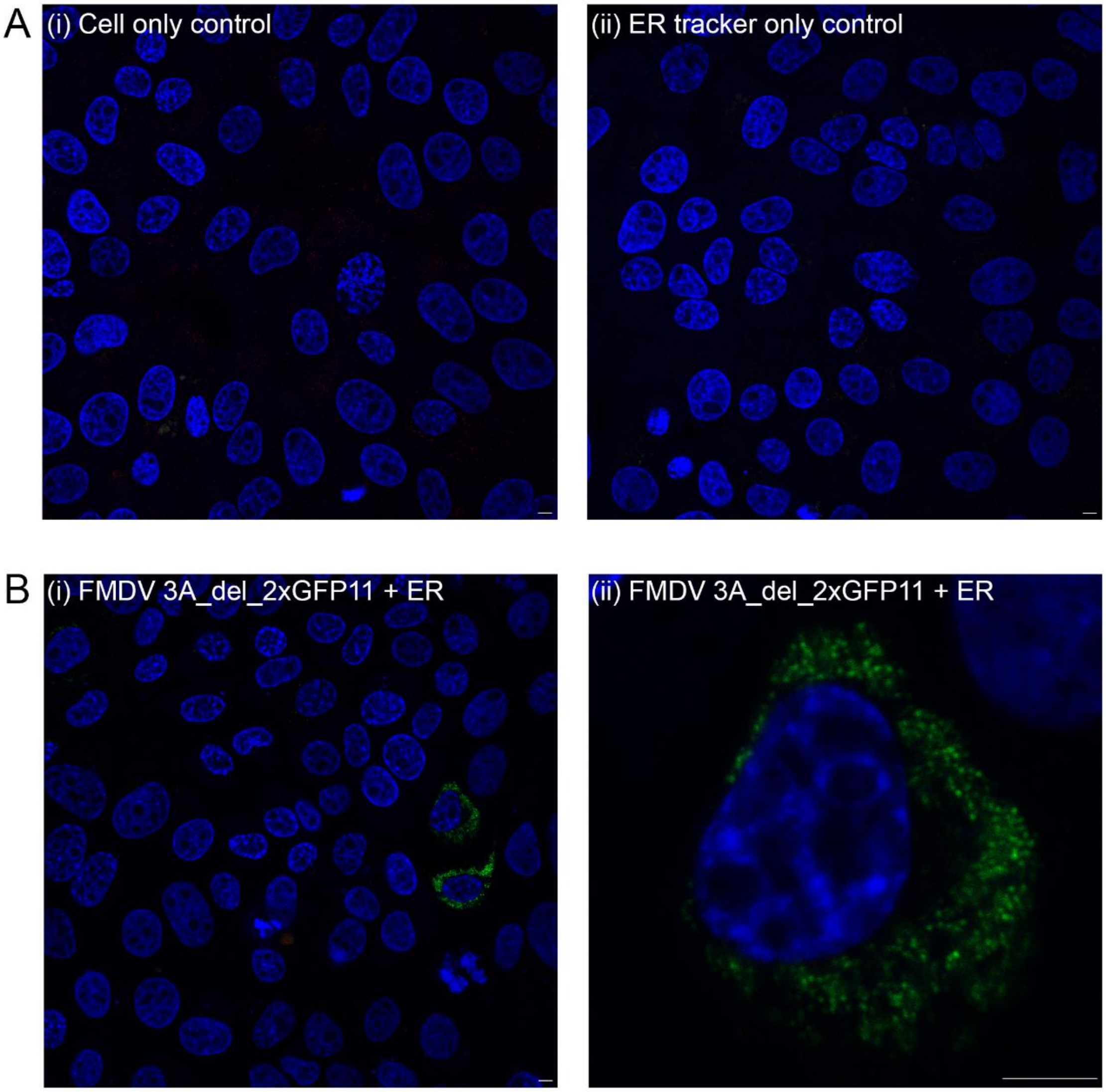

Figure 3.11 FMDV infected PK-15 cells were permeabilised and stained with ER tracker.

PK-15 cells were transfected with GFP1-10 and infected with FMDV 3A_del_2xGFP11. Infected cells were stained with ER tracker (red) and fixed at 3.5hpi and permeabilised with Triton. Nuclei stained with DAPI (blue). A(i) and (ii): Controls. B(i) and (ii) represent infected cells stained with ER tracker (red). GFP (green) signals are seen with no ER tracker signals observed. (Scale bar = 5 µm)

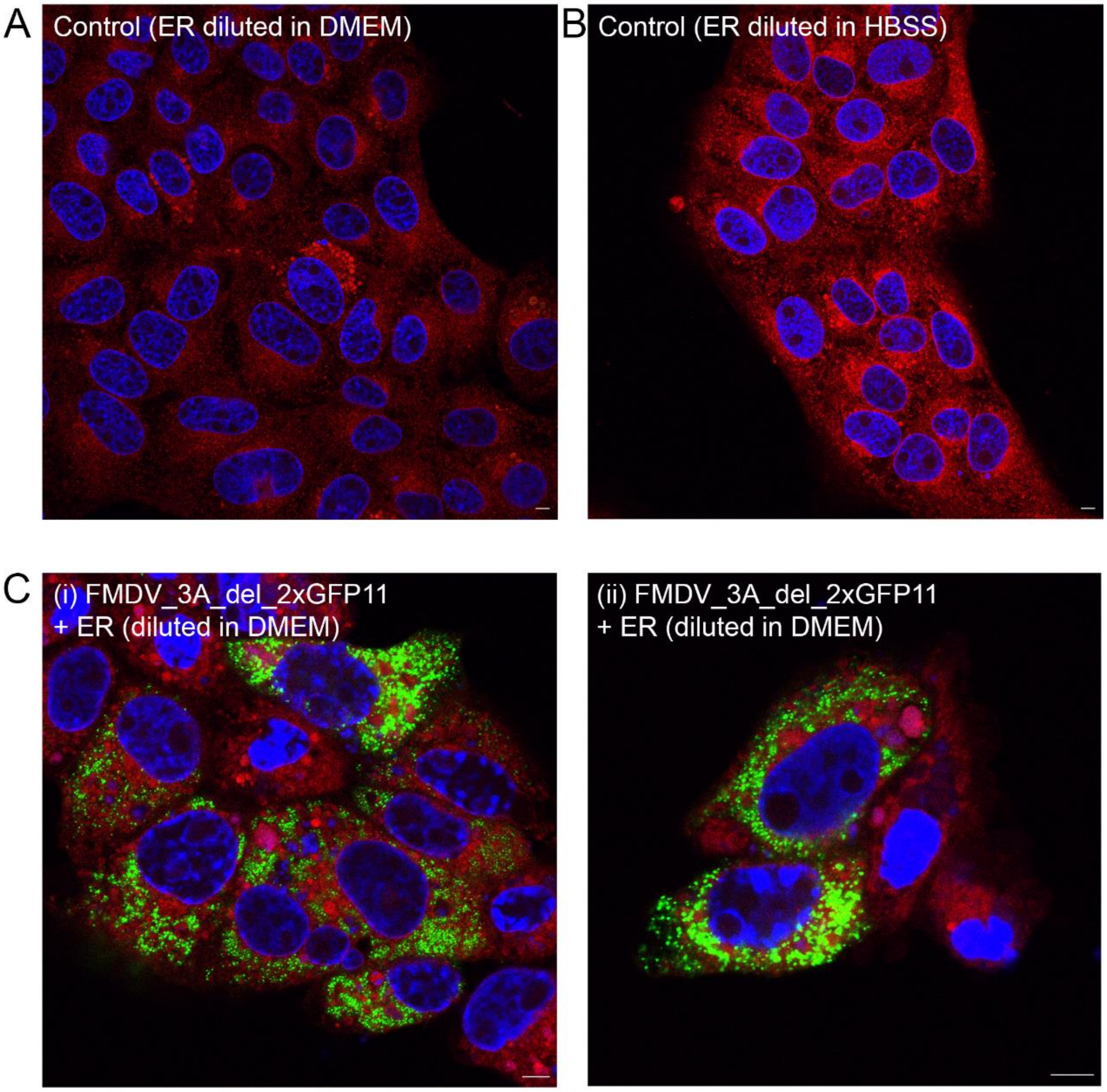

Figure 3.12 FMDV infected PK-15 cells without permealisation of cells and stained with ER marker.

FMDV 3A_del_2xGFP11 infected PK-15 cells with GFP1-10 transfected and stained with ER tracker (red) were fixed at 3.5hpi, without permeabilisation of cell membranes. Nuclei stained with DAPI (blue). A and B are controls stained with ER tracker diluted in DMEM and HBSS respectively. Both have shown a high level of noise in cells. A lot of the ER stain (red) appear to show a higher noise signal in the perinuclear region compared to the cytoplasm, this is particularly obvious when ER tracker was diluted in HBSS. C(i) and (ii): Infected cells were stained with ER tracker diluted in DMEM. GFP (green) signals are strong and distinct at 3.5hpi where ER signals are relatively weaker and not specific. There showed no colocalization of both signals. (Scale bar = 5 μm)

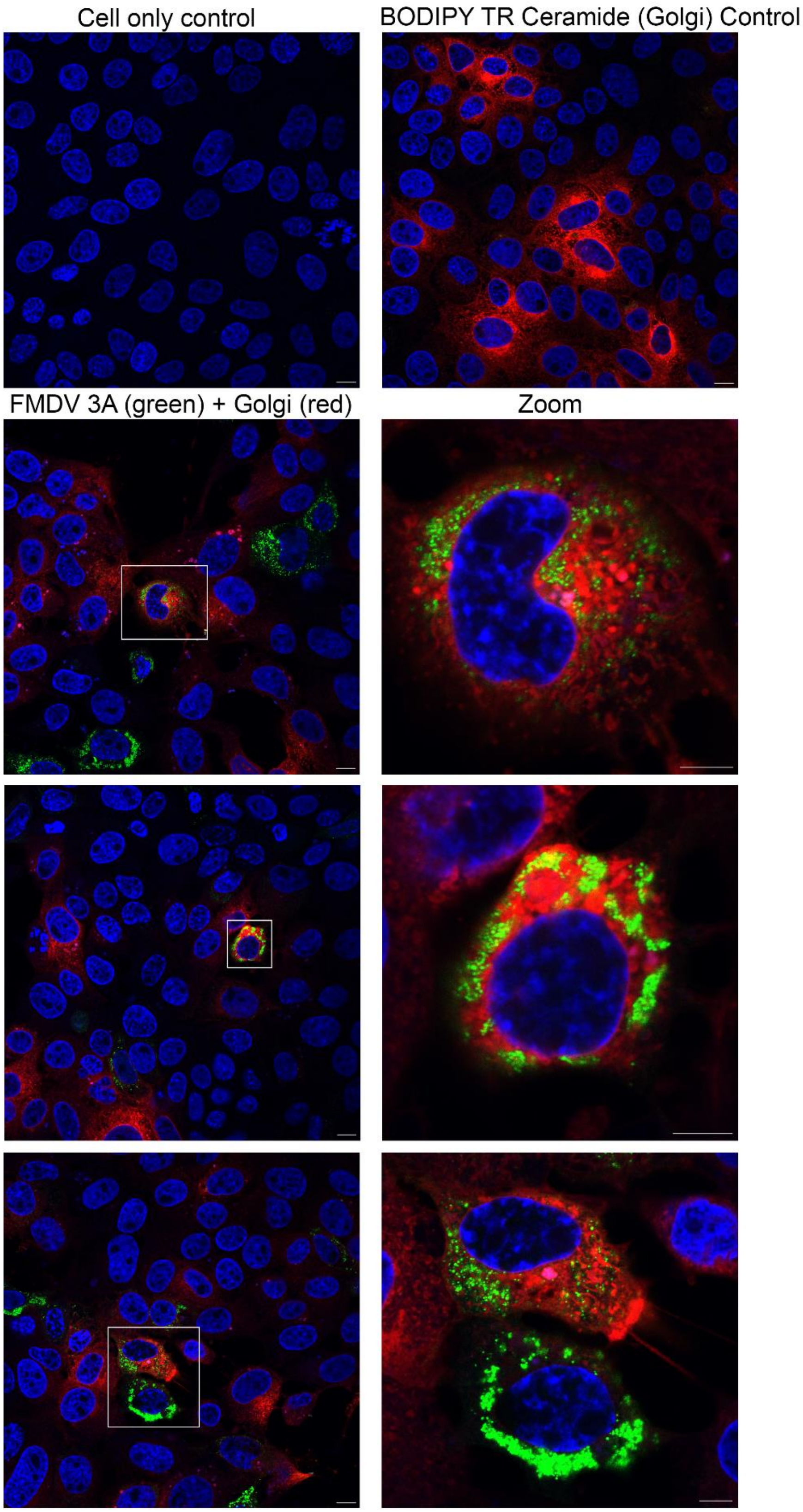
Cell only control
BODIPY TR Ceramide (Golgi) Control
FMDV 3A (green) + Golgi (red)
Zoom

Figure 3.13 PK-15 transfected with GFP1-10 infected with FMDV 3A_del_2xGFP11 stained with BODIPY TR ceramide (Golgi tracker) fixed at 3.5hpi.

Top panels present the controls. Infected cells presented a strong GFP (green) puncta in cluster across the cytoplasmic area. Golgi marker (red) signals are observed in some cells. Some cells express both the 3A-GFP signals and Golgi marker signals, the green and red signals appear adjacent to each other with no co-localisation observed. Nuclei stained with DAPI (blue) (Scale bar = 10 μm, zoomed panels scale bar = 5 μm)

3.5. Discussion

Information on the interaction of viral proteins and rearranged membranes induced during viral replication for FMDV is still lacking. Therefore, the development of a system that uses fluorescent tags is the simplest and the most direct approach to correlate both the viral protein and the membrane-associated with replication. We aimed to combine our fluorescently-tagged FMDV with membrane trackers to develop a CLEM system to study the localisation and dynamics of FMDV 3A protein exploiting details of FMDV replication. Most importantly, since these fluorescent tags are small, there is minimal risk that they will disrupt the function of 3A. Anti-3A monoclonal failed to recognise our recombinant viruses suggesting that the epitope site for anti-3A monoclonal was disrupted by our site deletion and tag insertion. Overall, our results from the confocal and our observations of CPE development infected with recombinant FMDV have shown that no noticeable disruption was observed under the microscope and that all viruses are genetically stable and functional.

A CLEM system relies on the identification of the target protein and the membranes of cellular organelles. Tags that can be used in both confocal, or live cell imaging, and directly in EM would be able to develop a more coherent system to localise the viral proteins and their interaction with membranes. Therefore, we chose to insert tetracysteine and metallothionein tags. Tetracysteine tags had been used in a study by (Li *et al.*, 2010) looking into the virus-host interactions of influenza infected cells. They have developed this system for their live-cell imaging of viral proteins in cells and successfully identified the non-structural protein nuclear import inside the infected cell. Our study has shown that our tetracysteine-tagged viruses are all functional in LM with the use of ReAsh stain, which mediates the photo-conversion of DAB that binds to the tetracysteine tag, this then appears as a dense dark particle which, in our case will represent 3A, directly in EM. This also helps us with correlating the signals from live-cell imaging. Hence, this would be a useful tool in the future for the development of the CLEM system. The only complication we have in this category of tags is the metallothionein tag, a small metal and gold tag that clusters metal atoms into a high-density particle which can be directly visualised in EM. However, this has been reported to be toxic to living cells (Bouchet-Marquis *et al.*, 2012). We created a recombinant virus that contains both tetracysteine and metallothionein tags hoping that ReAsh stain will be useful for this virus and cells would be safe from the toxic effect. However, the results were not as we expected as shown in Figure 3.6. Alternatively, since we have the sequencing data, both results then suggested that detection of the tetracysteine tag by ReAsh stain is disrupted due to the presence of the metallothionein tag.

Split-GFP system

An overview of GFP has been reported by Tsien, (1998) including how pH, temperature, protein concentration and prior illumination can affect the GFP whilst Romei and Boxer, 2019 reported an overview of the split-GFP system and its limitation (Romei and Boxer, 2019). The application of GFP has become common over the past years since its first discovery by Shimomura, Johnson and Saiga, (1962). Following the rapid expansion of the microscopy field, more details on protein structures and folding have been revealed. The development and application of the split-GFP system has then been more widely used to study protein-protein interaction. It has then been used to localise viral proteins and study the dynamics and viral protein to cellular proteins gaining an in-depth understanding of the virus' life cycle. An example of a picornavirus study that involves the split-GFP system is reported by Schaar et al., (2016b) by employing the split-GFP system to study enterovirus replication. We required a fluorescent tag for confocal microscopy which could ideally be visualised in EM to understand the details of FMDV replication. Herod et al., (2015) and Li et al., (2014) exploited 3A's tolerance of a small deletion leading us to develop this split-GFP system for FMDV. We have shown that the insertion of GFP11, from one copy to three copies, into FMDV 3A has no mutation after 10 passages nor disruption to its function under confocal. We have started to obtain more details, through localising 3A, during the replication cycle. As mentioned, various factors affect the detectability of the GFP protein (reviewed in Tsien, 1998). We also encountered various issues in this study. Firstly, GFP1-10 can be expressed by transient transfection or with a stable cell line. We proved earlier that transient transfection gives a higher expression level of GFP1-10 and thus the 3A signals become more noticeable. However, one constant problem that remained is the variable transfection rate. The same protocol was applied to all experiments to maintain minimal variabilities that could affect our results. Further issues appeared when it was combined with the use of membrane trackers in CLEM development. One of the issues was the buffer used to dissolve the membrane tracker, and that the fixation protocol would need to be altered as the ER tracker we used cannot be permeabilised. Nevertheless, adding additional controls for each experiment, although increasing the working sample size, reassured us that human errors could be minimised. As an alternative option for the split-GFP system, the stable porcine cell line that expresses GFP1-10 works less efficiently after bulk sorting. The reason for this remains unknown but does not affect our work progress and hence is left for further investigation.

CLEM system

Our findings from this study were that the Golgi membrane tracker signals appeared adjacent to FMDV 3A signals during replication. This is rather interesting as it slightly contradicts to what we expected based on other studies. FMDV proteins are known to appear near the Golgi, and it was previously shown that 3A partially co-localises with ER and Golgi markers (O'Donnell *et al.*, 2001; Knox *et al.*, 2005; García-Briones *et al.*, 2006). Later, Midgley et al., (2013) further investigated the association between them. They first identified ER to be involved during replication which our results contradicted as ER membrane tracker did not show any distinct pattern associating with 3A. Secondly, in their study, Golgi markers were not detected during replication, leading to our hypothesis of the redistribution of Golgi during FMDV replication. This was expected by us at the beginning of the study. Our proposed theory is that the Golgi protein marker was dispersed during replication and hence became undetectable. Contrarily, Golgi membrane remains intact in the infected cells and hence was detected when Golgi membrane stain was used. They appear near the replication site 3A, suggesting this is a potential site for targeting in EM, moreover, the Golgi membrane could be the main source of cellular membrane associated with viral replication. In addition to this, TR-ceramide is not specific to staining Golgi, it also stains lipids in cells. Therefore, from our data, the red signals are likely to be a combination of lipid droplets and Golgi. This will be discussed in detail in Chapter 5 or 6. In summary, we identified that the Golgi membrane could potentially serve as a major source of membrane for FMDV replication, and in the future, this CLEM system could elucidate more information about the Golgi redistribution and interaction with the FMDV replication site over the time course.

3.6. Summary

In summary, four major types of tags were inserted into FMDV 3A using reverse genetics. We observed no mutations, and all 3A-tagged FMDVs were functional via validation using the confocal microscope. The exception was 3A-metallothionein-tagged recombinant FMDV which requires further development in the future as there was no available protocol for this tag in confocal or EM for *in vivo*. We further optimised the split GFP system, where we employed the FMDV 3A that encodes two copies of GFP11 fragments (3A_del_2xGFP11) for our experiments. We observed similar time was required for CPE development for 3A-tagged recombinant FMDV and WT FMDV. A further comparison of the rate of replication was shown by a growth curve comparing WT FMDV with FMDV 3A_del_2xGFP11 which showed no differences. We then employed the split-GFP system to develop a CLEM system. Our observation from these preliminary experiments for the CLEM system was that Golgi tracker signals appeared adjacent to FMDV 3A signals with no co-localisation detected. Further optimisation of this protocol is required for both fixed cells and live cell imaging in the future.

Chapter 4 Ultrastructural rearrangement in FMDV and ERAV are comparable

4.1. Introduction

Transmission electron microscopy (TEM) is an important tool to study ultrastructural contents and thus, contributes significantly to cell biology. Ultrastructure is defined as the structure within cells that can only be visualised via EM. Conventional transmission electron microscopy can be summarised as the following steps:

(1) Prepare cell samples on a coverslip
(2) Fix and stain samples
(3) Embed the plastic coverslip in resin
(4) The resin is then cut into thin sections and stained
(5) Image these thin sections in the electron microscope.

Ultrastructural information within the EM images will then be analysed during the final step. Our aim in this chapter is to investigate the ultrastructural changes caused by FMDV and ERAV in cells, visualising the virus-induced membrane structures such as single and double membraned vesicles (SMV, DMV). Since ERAV will be used as a surrogate model in our cryo-EM study (Chapter 5), we will be looking for comparable features between the two viruses.

Positive strand RNA viruses cause extensive rearrangements in host cells to facilitate viral replication. The details of these rearrangements have been explored more widely in other picornaviruses (Limpens *et al.*, 2011; Belov *et al.*, 2012; Wolff *et al.*, 2020; Dahmane *et al.*, 2022). Viruses divert secretory pathways and employ host cell membranes to form a replication platform, which is known as the replication organelles (ROs). Examples of ROs are SMVs and DMVs, which are vesicles delineated by a single or double membrane layer. Acidification caused by fixation leads to dissociation of virus capsids hence the presence or absence of newly formed virions cannot be used as an indicator of virus infection (Johnson, 1985; Hayat, 1989). Therefore, SMVs/DMVs serve as hallmarks of infection in our analysis. As mentioned, membrane vesicles are commonly observed in other picornavirus-infected cells, the details of which have been widely studied (Limpens *et al.*, 2011; Belov *et al.*, 2012; Wolff *et al.*, 2020; Roingeard *et al.*, 2022). For example, during infection, poliovirus inhibits ER-to-Golgi trafficking. It was demonstrated that nsp 2B of poliovirus colocalises with a complex that mediates vesicle transport between ER and Golgi, known as COPII, on vesicles budding from ER (Rust *et al.*, 2001). These empty vesicles, that are enriched with COPII, appear near the *cis*-Golgi during early infection with the complexity of these vesicles increasing over time, from a single to a double membrane (Stephens *et al.*, 2000; Rust *et al.*, 2001; Szul and Sztul, 2011; Trahey *et al.*, 2012; Abernathy *et al.*, 2019). This shows that viral proteins disrupt and divert the intracellular pathway and membranes for viral replication. In addition, remodelled membrane structures have been linked to autophagy, although autophagy induced DMVs are known as autophagosomes. The similarity between the virus induced vesicles in FMDV infected cells and those in other picornavirus infected cells justifies the use of these structures as an indicator in conventional TEM studies for aphthovirus infection.

Current conventional fixatives, such as paraformaldehyde (PFA) and glutaraldehyde (GA), are both aldehyde fixatives commonly used for microscopy sample preparation. Both stabilise proteins by crosslinking but with PFA, which penetrates cells relatively quickly as it is a smaller molecule, the crosslink reaction is reversible by adding excess water (Jackson, 1978; Solomon and Varshavsky, 1985; Hayat, 1989; Hoffman *et al.*, 2015). GA on the other hand permanently crosslinks proteins but because of this, infiltrates slowly into cells. The aldehyde groups react with amines resulting in the formation of a methylene bridge. The methylene bridge formed between macromolecules crosslink proteins. Aldehydes do not preserve other cellular structures such as lipids which can lead to extraction of these elements during downstream processing, producing fixation artefacts. During fixation GA is known to cause acidification in solutions, especially if amino acids or proteins are present, which precedes crosslinking as it penetrates cells (Johnson, 1985; Hayat, 1989). This low pH dissociates the FMDV capsid (Curry *et al.*, 1995; Martín-Acebes *et al.*, 2010; Vázquez-Calvo *et al.*, 2014). We investigated a different approach by testing lower concentrations of aldehyde fixatives to stabilise the capsid in a pre-fixation step. Further details on this new protocol will be discussed in section 4.3.

As previously explained in Chapter 1, FMDV can only be used in a high biocontainment laboratory, therefore we will have to use the surrogate model equine rhinitis A virus (ERAV) for our cryo-EM work at Diamond Light Source (Chapter 5). ERAV is another member of the *Aphthovirus* genus, and has a similar genome organisation to FMDV, only lacking the three copies of 3B (VPg). In this chapter, we will be comparing the characteristics of FMDV and ERAV-infected cells in order to validate the usage of this virus as a surrogate model to study the replication details by cryo-EM.

4.2. Visualising site of replication

Current conventional EM protocols require the use of chemical fixatives. We used GA to fix the cells on plastic coverslips at 8hpi, 9hpi and 11hpi, before further sample preparation. Timepoint determination was based on the morphology of cells and cytopathic effect (CPE), further details regarding this choice will be presented in Chapter 5.1. Infected cells on coverslips were processed and embedded in resin, then cut into thin slices, stained, and mounted on EM grids. Data was collected and interpreted under the supervision of Prof Pippa Hawes (Head of Bioimaging, The Pirbright Institute).

To investigate the change in the ultrastructure of infected cells, we first infected SK-RST (hamster) cells with FMDV at an approximate MOI0.1. The FMDV replication site is a relatively distinct area inside the infected cell. At late time points the contents are concentrated in the perinuclear region for replication (outlined in Figure 4.1A), and all cellular components needed for replication are clustered into this packed region creating an optimal environment for viral replication. A major distinctive feature of FMDV infection are the SMVs as they are absent in uninfected cells (red arrows in Figure 4.1B). They are typically between 100 to 300 nm in size. These virally induced vesicles consistently appear to have a darker stained membrane than other cellular membranes by conventional EM which could indicate a different lipid/protein composition. SMVs also present with a distinctive ‘pavement’ pattern inside which is not seen inside any vesicles of uninfected cells (Figure 4.1B). Interspersed with these SMVs are also double membraned vesicles (DMVs) as seen in Figure 4.1C.

These are also considered to be part of the ‘replication organelle’ (RO) because of their location. Another hallmark of infection is the accumulation of polysomes in the replication area which presumably are in the process of translating viral RNA (Figure 4.1D). While we are able to identify infected cells by the rearrangement of host cell components, the obvious question is where are the newly formed virions? As discussed, the fixative used for standard chemical fixation for EM reduces the pH of the sample. FMDV capsids are acid labile, so it is reasonable to conclude that the fixative is destroying the newly formed virions. As part of an ongoing collaboration between the Pirbright Institute, University of Oxford and eBIC at Diamond Light Source, infected cells have been prepared by high pressure freezing which does not use acidic fixative. Images show that cells exhibit less extraction; the cytoplasm has retained its contents therefore the replication area and accumulation of ribosomes is not as distinctive as in chemically fixed cells (Figure 4.1E). Also, the RO vesicles appear to have an electron dense centre which is lost during standard fixation. Importantly though, it is possible to identify clusters of newly formed virions, located near RO vesicles (Figure 4.1F). It is interesting to note that while the RO vesicles are located very close to each other, they do not cluster as closely as the enterovirus RO vesicles which often appear to touch membranes (Melia *et al.*, 2019).

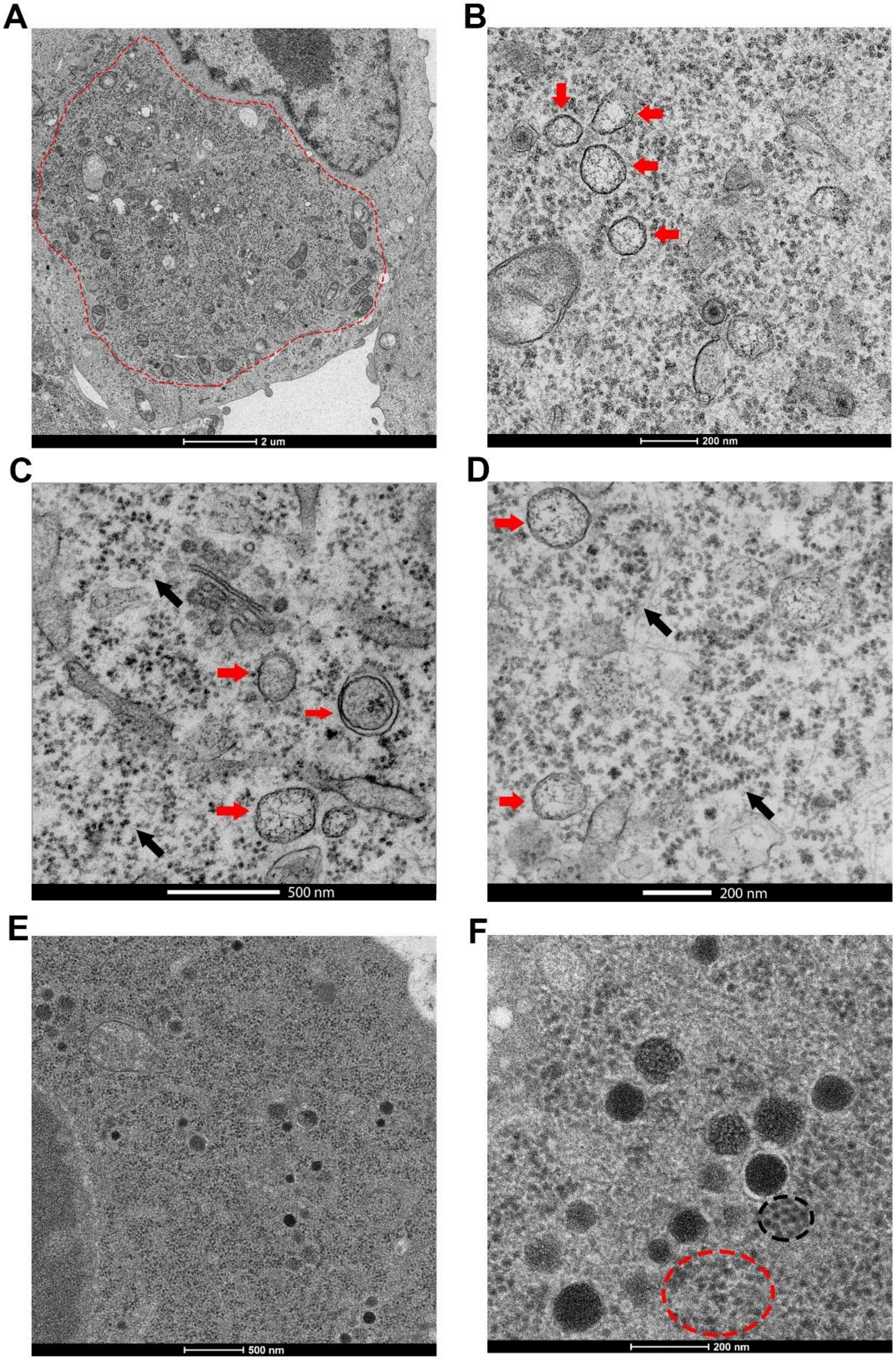

Figure 4.1 Conventional TEM of FMDV infected SK-RST cells.

FMDV infected SK-RST cells prepared by chemical fixation **(A-D)** or high pressure freezing **(E-F)**. The distinct replication site is visible in panel A. Red arrows in panel B indicate the single membraned vesicles (SMV) that vary slightly in size. Double membraned vesicles (DMV) also form part of the replication organelle, as seen in panel C. The accumulation of ribosomes/polysomes (black arrow) in the replication site is also another distinctive feature of infected cells prepared this way. High-pressure freezing of infected BHK cells retains more cytoplasmic contents which makes it more difficult to identify the replication area and accumulation of ribosomes (panel **E**), however replication organelles (RO), both SMVs and DMVs, are present and have retained an electron dense core in this preparation (red arrows). Clusters of virions are visible (**F** dashed circles).

4.2.1. Comparison of FMDV and ERAV infected Vero cells

This study aims to understand the replication of Aphthoviruses using different microscopy techniques. As mentioned earlier we would like to use ERAV as a surrogate model for our study of FMDV replication outside the high containment facility. In this section we will compare FMDV and ERAV infected cells investigating features that are comparable and thereby determining if ERAV is a good model system for FMDV.

Unfortunately, ERAV does not infect hamster cells or porcine cells, and therefore we employed another cell line, Vero cells (Figure 4.2 A-B). Vero cells are a monkey kidney cell line that are susceptible to both FMDV and ERAV infection. Previously, we showed that the SMVs and DMVs and polysomes are the hallmarks of FMDV infection in conventional EM (Figure 4.1). We fixed and compared cells at a single timepoint, 3.5hpi for FMDV and 9hpi for ERAV, as we believe these timepoints are equivalent (refer to Chapter 5.2).

Initially, we compared FMDV infected SK-RST cells to infected Vero cells and showed that the same features of infection are present in both cell types. Replication organelles were identified, and the distinct replication sites are similar in both the cell lines. We then compared FMDV infected and ERAV infected Vero cells. We infected FMDV and ERAV at high MOI and fixed them at 3.5h post FMDV infection and 9h post ERAV infection respectively (which is also discussed later in more details in Chapter 5.3.2). SMVs were observed in small clusters in both ERAV and FMDV infected Vero cells (Figure 4.2). Although the replication area was not as distinct in ERAV infected Vero cells, it still showed a similar change in the ultrastructure to FMDV infected cells where DMVs and accumulation of ribosomes were observed in the perinuclear region. Hence, the appearance of SMVs in FMDV and ERAV infected cells served as the identification of infected cells, and we confirmed that both viruses induce the same type of replication organelles. Interestingly, in ERAV infected cells areas of ‘membranous web’ (MW) were regularly seen (Figure 4.2F), apparently derived from ER as ribosomes are clearly visible at the membrane-cytoplasm interface. Due to COVID, we were unable to repeat the experiment, however, this initial experiment was sufficient for us to continue our work with ERAV using cryo-EM at Diamond.

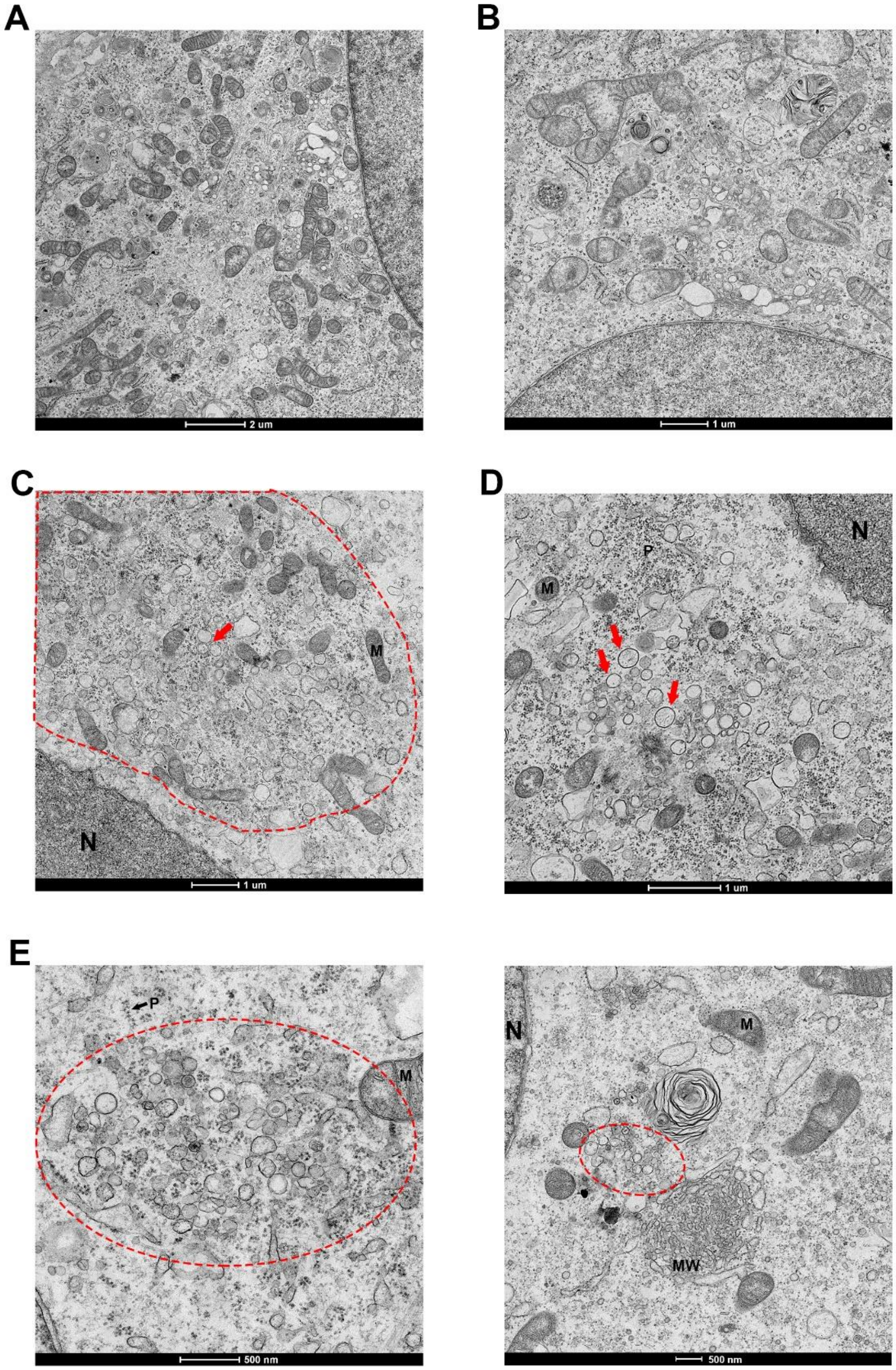

Figure 4.2 FMDV and ERAV infected Vero cells fixed using standard GA protocol.

Uninfected Vero cells **(A-B)**. FMDV infected Vero cells fixed at 3.5hpi. Edge of the replication area is highlighted in C. Inside the replication area are many vesicles and ribosomes/polysomes, characteristic replication organelle vesicles are seen (**C-D**, red arrows) ERAV infected Vero cells fixed at 9hpi also show an accumulation of replication organelle vesicles (E, red arrows) and ribosomes in replication area (**E**, dashed area). Another replication area is visible in panel F (dashed area) alongside an accumulation of membranes, potentially virally induced, derived from ER (ribosomes are still present on membrane surface (arrow)). N = nucleus, M = mitochondrion, P = polysome, MW = membranous web.

4.3. Double fixation protocol for FMDV capsid preservation

FMDV capsid is acid labile and as such is extremely sensitive to pH and temperature changes. The conventional fixative GA is known to be acidic. FMDV capsids inside cells have never been preserved using conventional fixation for TEM study. It is believed that acidic waves, created when fixative contacts the cells, dissociate the capsid. Our lab has developed a double fixation protocol to preserve and image the intact capsid by confocal microscopy (unpublished data). We have shown that intact FMDV capsid can be detected by immunofluorescent microscopy when the cells are first fixed with a low percentage of PFA (0.5 - 1%) before a higher concentration (4%) PFA fix (which is needed to comply with biosafety regulations (see Chapter 2.6 for details). This experiment tested a range of low PFA concentrations, from 0.5% to 2%. Since SK-RST were found to be a hamster cell line, hence we employed another cell line PK-15, which is a pig cell line. FMDV infected PK-15 were fixed with low concentration PFA (0.5% - 2%) followed by indirect labelling with an antibody against intact FMDV capsid, M170 (Harmsen *et al.*, 2007, 2011), and a secondary species-specific antibody with fluorophore, before a high (4%) PFA was added to further fix the cells. Figure 4.3 presents the results from the preliminary experiment where panels B-C showed the M170 (green) signals representing FMDV intact capsid. We can see the presence of intact capsids (green puncta) when a low concentration of PFA, up to 1% was used. However, at 2% PFA fixation, signals for the intact capsid were not visible, suggesting that the capsids were dissociated. Therefore, in order to preserve the intact capsid, the PFA fixation should not exceed 1%. We wanted to adapt this protocol to try to preserve capsids for imaging in the EM. The rationale is to crosslink the intact capsid using a mild PFA fixation ("pre-fixation" step), before then preserving the cell ultrastructure using the conventional GA fixation protocol used in the previous section. The hypothesis is that PFA will stabilise the capsid in preparation for GA fixation.

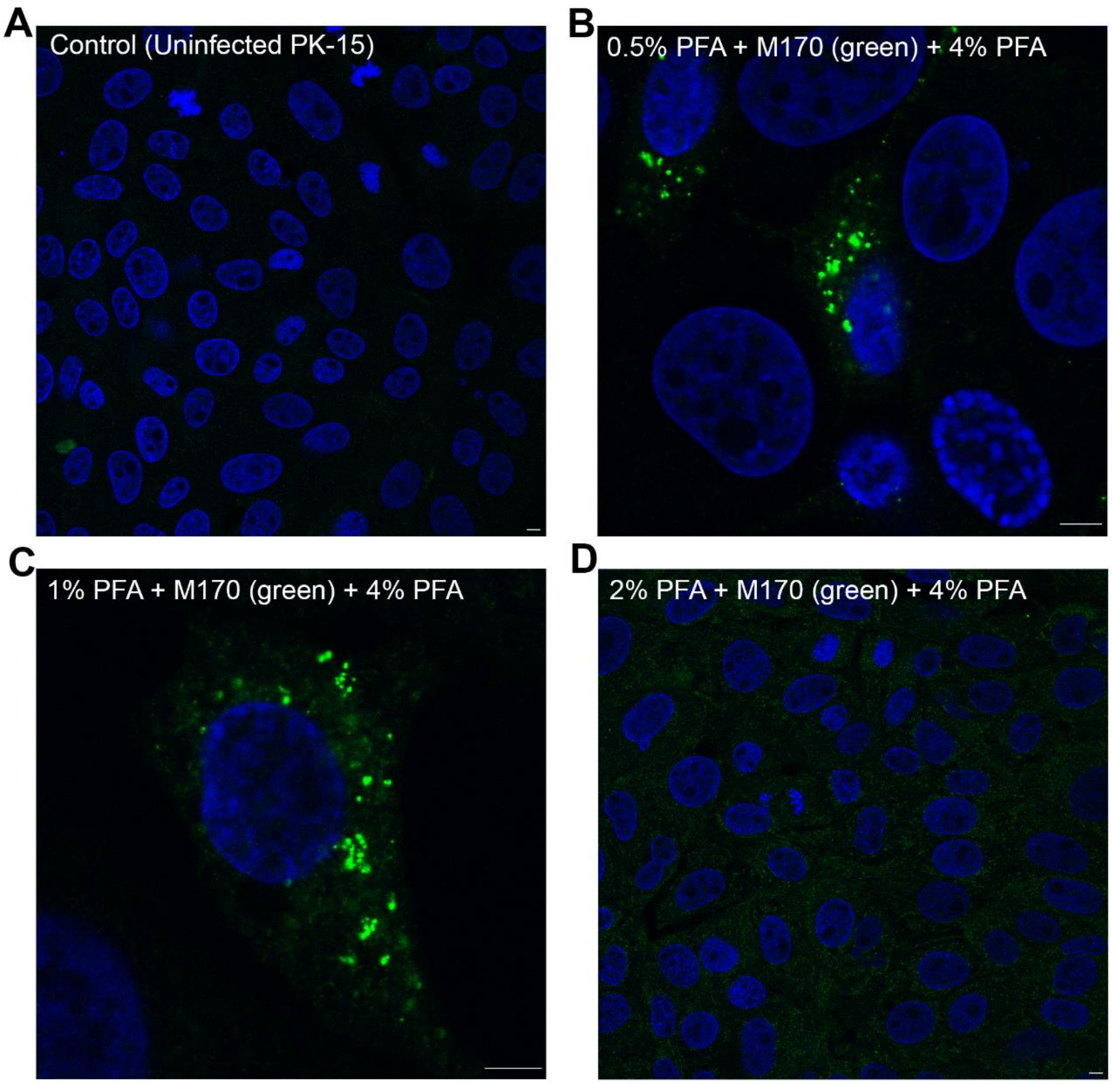

Figure 4.3 FMDV infected PK-15 fixed using the double fixation protocol.

Cells were fixed at a lower concentration of PFA and an antibody raised against the intact FMDV capsid (M170) is added before further fixing with a higher concentration of PFA. **(A)** Control. **(B -D)** show FMDV infected cells fixed with three concentrations of PFA (0.5% to 2% PFA respectively) before adding M170 (green) followed by a 4% PFA fix. Signals of intact capsid at 0.5% and 1% PFA were detected. Cells fixed with 2% PFA showed no signals of the intact capsid. (Scale bar = 5 μm)

To compare the replication details observed in the cryo-EM work at Diamond Light Source to that at Pirbright, it would be ideal to compare both ERAV and FMDV particles in infected cells. Additionally, the pre-fixation protocol may allow us to export samples from high containment such that cryo-EM can be done, thus making a more detailed comparison using cryo-ET possible for FMDV.

We applied this protocol to EM sample preparation. Again, FMDV infected PK-15 were fixed with a low percentage PFA at 3.5hpi, followed by GA fixation and standard EM sample preparation (please refer to Chapter 2.9.1.). However, the ultrastructure of the cell was not well preserved (Figure 4.4 A-B). Overblown mitochondria and rucked membranes indicate an osmolarity mismatch between the cell and fixation buffer. Also, intact capsids were still not visible. Therefore, we investigated different buffers that could be used to dissolve the PFA and GA. The rationale behind this was to resolve the two issues we encountered: namely, the change in osmolarity in cells and the acidification of cells during fixation. In order to resolve both issues, we dissolved both PFA and GA in different buffers including cell culture media Glasgow’s minimum essential medium (GMEM), EM buffer (please refer to the recipe in Chapter 2.9.1) and HEPES. GMEM and HEPES are commonly used in cell culture and would potentially minimise the issues of osmolarity and pH as the cells are familiar with this medium. As part of our standard EM preparation protocol, GA is always used in combination with EM buffers to ensure we are using the appropriate osmolarity and pH for fixation. Our rationale behind dissolving PFA in the EM buffer is to maintain the osmolarity by minimising the use of different buffers with the different fixatives. This then reaches the equilibrium between cells and the fixative, causing minimal destruction.

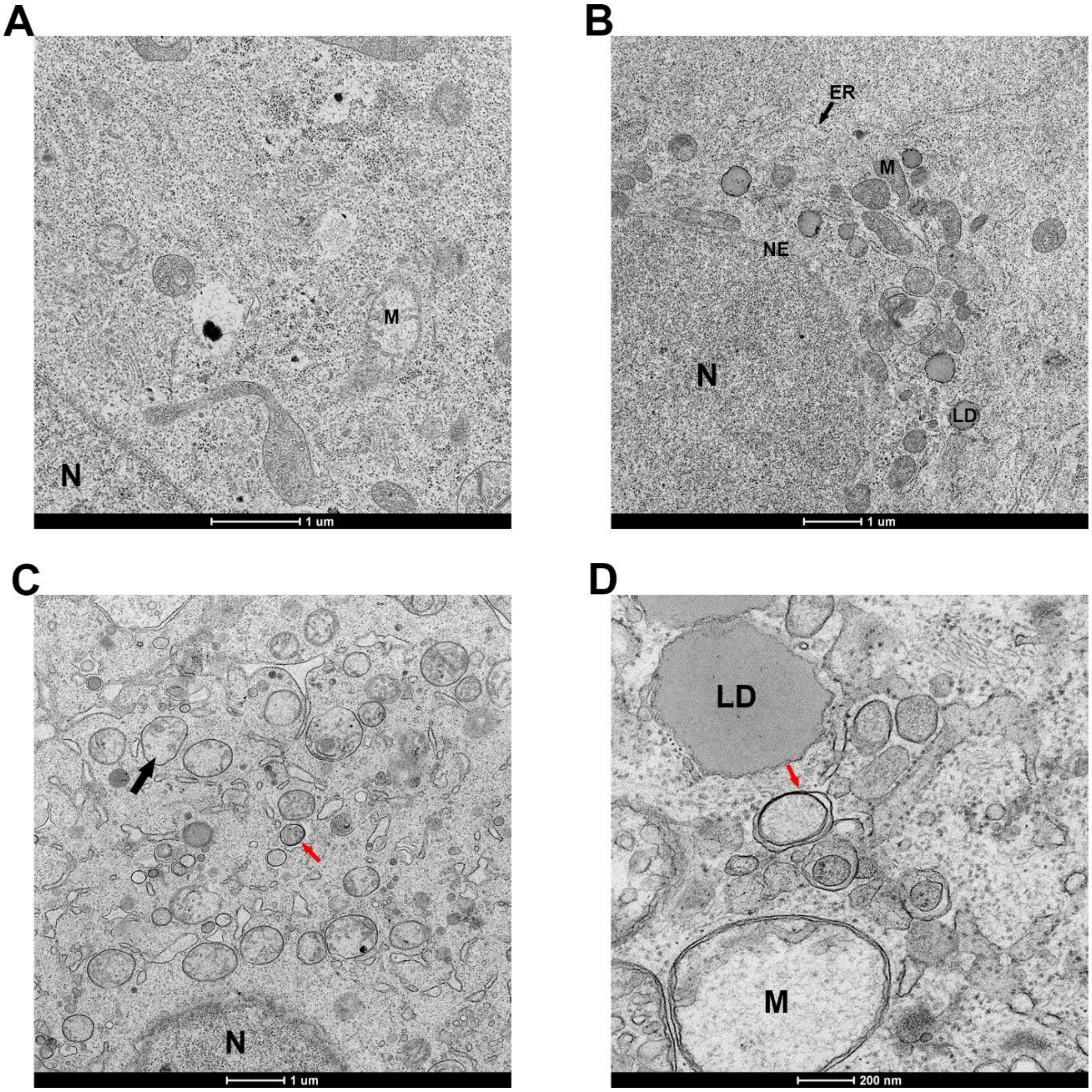

Figure 4.4 FMDV infected PK-15 fixed with PFA and GA dissolved in different buffers. Panel A presents FMDV infected PK-15 fixed with 0.5% PFA dissolved in GMEM followed by GA dissolved in HEPES. Organelles are barely distinguishable and display signs of extraction due to osmolarity mismatch between the cell and the fixative. Mitochondria can be particularly susceptible to this phenomenon (Schultz and Karlsson, 1965; Ghadially,

1988; Hayat, 1989). Panel B presents an infected cell fixed with 0.5% PFA dissolved in EM buffer and followed by GA dissolved in HEPES. Again, cell organelle membranes are either not visible (NE, ER) or are rucked (M, LD). It is not possible to identify any other cell organelles or the virally induced replication area. Panels C and D show FMDV infected cells fixed with 0.5% PFA dissolved in EM buffer and GA dissolved in EM buffer (at low magnification and high magnification respectively). Whereas we can now distinguish organelle membranes, they have not been well preserved, note the lack of definition of the mitochondrial cristae and extraction of mitochondrial matrix (arrows). Although we can identify replication organelles (red arrows), no FMDV capsids were seen in this cell suggesting this protocol was not optimised to preserve FMDV capsids. At higher power rucked organelle membranes caused by poor fixation are clear (LD, M). N = nucleus, NE = nuclear envelope, LD = lipid droplet, M = mitochondria, ER = endoplasmic reticulum.

As seen in our results (Figure 4.4 C-D), pre-fixed cells showed a level of disruption even with different buffers, for example the swelling of mitochondria and missing content inside these organelles. While the level of disruption from the fixative is tolerable, we could not see any virions in our sample hence we did not fulfil our aim. The absence of intact FMDV capsid and disruption of intracellular context suggested that osmolarity equilibrium was yet to be reached and needed further refinement in our protocol. The FA did not stabilise the capsid structure and in addition more than likely led to the disruption of the ultrastructure. Although we were not able to identify any viral capsids, virus induced membrane vesicles (red arrows in Figure 4.4 D)) were still visible. We can therefore still identify infected cells even with this cellular disruption.

In summary, we proved that conventional fixation method is inappropriate for preserving the virus assembly intermediates for TEM analysis. This could be investigated further as part a future direction to enable us to export samples from the high containment facility for further analysis.

4.4. Discussion

Our current indicator for aphthovirus infection in cells is limited to the clustering of ribosomes in the cytoplasm and virus-induced membrane vesicles. FMDV infected SK-RST cells showed a distinct and concentrated replication region filling most of the cell cytoplasm whereas in FMDV infected Vero cells this region are less concentrated, and it is not a feature we observed in ERAV infected Vero cells to the same extent. We can see some signs of ribosome clustering, but the presence of polysomes and ribosome clusters is not as obvious as it is in FMDV infected cells. This, and the presence of membranous web, suggested to us that there may be a slight difference in FMDV and ERAV infection, even though both are aphthoviruses. However, the characteristic replication organelle vesicles are clearly present in ERAV infected cells, albeit with subtle structural differences. For example, the ERAV vesicles can appear to be more pleiomorphic than FMDV vesicles, and form a tighter cluster, sometimes with adjacent vesicles touching. These slight differences were not significant enough to render the comparison between FMDV and ERAV infection irrelevant, so we still went on to use cryo-EM (in Chapter 5) as a new approach for the *in vivo* replication study of aphthoviruses. Part of our aim described in Chapter 1 was to correlate both information from ERAV infected cells from cryo-EM and FMDV using our conventionally fixed samples as well as our recombinant viruses (Chapter 3). This information would ultimately provide insight to compare replication details between aphthoviruses and other picornaviruses such as enteroviruses. Replication details of enteroviruses are extensively studied. The abundance of membrane vesicles and their increase in complexity during replication is a significant feature of poliovirus infection. Our data show a reduced number of SMVs and DMVs in FMDV infected cells compared to enterovirus infected cells, which varied slightly in size but were identifiable as they are not present in uninfected cells. They appear in clusters, with individual SMVs found within the replication site. The number of SMVs and DMVs in both ERAV and FMDV infected cells is less than is seen in enterovirus infected cells at later time points. We compared these features at one timepoint only, perhaps more information would be revealed when later timepoints are also compared. Another reason that explains the difference in the number of membrane vesicles observed may lie in the cell line used for infection. As Vero is a monkey cell line, which is not a native host for the viruses, the infected cell characteristics may vary slightly to host cells. Also, there were lots of other vesicles that could be observed, potentially clustered near SMVs and DMVs, however it is difficult for us to identify whether they are virus induced in the absence of virions. Uninfected cells also contain many vesicles, single membraned vesicles form part of the endosomal and secretory pathways, however virally induced SMVs are distinct from these as of the electron dense layers and the lattice like structures inside the vesicles. We concluded that FMDV and ERAV do share some similarities, and both induce SMVs and DMVs that together form the replication organelle.

We have two purposes in developing the double fixation protocol; firstly, we would like to visualise intact FMDV and ERAV capsids in conventional TEM. Secondly, if capsids have been stabilised, we can then export these fixed samples out of high containment facility, prepared on cryo-EM grids, and analyse them in cryo-EM. FMDV capsids are sensitive to changes in the environment, a slight change in the pH or temperature causes the dissociation of the capsid. This is part of the proposed model for FMDV and ERAV genome release in cells: acidification inside the endosome dissociates the capsid and the genome enters the cytoplasm for replication (Berryman *et al.*, 2005; Groppelli, Tuthill and Rowlands, 2010). Crosslinking the intact capsid was made difficult due to the combination of the low pH of the fixative used for EM and the osmolarity mismatch between the fixative and cell. Therefore, capsids were never preserved in cells for analysis in EM. Fixative vehicles (buffers plus either electrolyte e.g. NaCl or non-electrolyte e.g. sucrose additives) need to be carefully matched to the cell osmolarity in order to preserve the ultrastructure for EM and minimise artefacts. Under unbalanced conditions and potentially improper handling, we can see the swelling of the cells and loss of intracellular contents as the downstream sample preparation steps will extract intracellular contents. Our study tested various combinations of fixatives in different buffers in consecutive fixation steps. This would provide useful information for future studies and help eliminate those buffers that are not suitable to reach that equilibrium in preserving the capsid and ultrastructure. In summary, we were close to osmotic equilibrium, with a small disruption to intracellular organelles that is tolerable for our study, but no virions were seen. Hence, the further optimisation of this protocol should focus on the detection of virions in EM.

4.5. Summary

We can identify infected cells and intracellular structures that indicated infection, i.e. characteristic single and double membraned vesicles in both FMDV and ERAV infected cells. This validates our usage of ERAV as the surrogate model for our cryo-EM work in the next chapter. We tried to develop a protocol to preserve FMDV capsids for electron microscopy using a pre-fixation step in order to export FMDV infected samples out of the high containment in the future. We could not fully optimise the protocol and hence did not detect any intact capsids in conventionally fixed samples. However, this does not prevent us from identifying infected cells. This can be further investigated in future projects as being able to directly compare both FMDV and ERAV replication details in cryo-EM would allow us to identify the similarities and any differences between the replication details of both viruses.

Chapter 5 Visualising ERAV replication details *in situ* using cryo-EM

5.1. Introduction

As introduced in Chapter 1 and 4, the aphthovirus genus include FMDV and ERAV which, like other picornaviruses, remodel host cellular membranes to promote viral replication (Tao and Ye, 2010; Belov and Sztul, 2014; Wolff *et al.*, 2020). After internalisation of the virus, it is assumed that the genome is first released into the cytoplasmic region for viral protein synthesis and replication (Groppelli *et al.*, 2017) followed by capsid dissociation in an acidic compartment (Curry *et al.*, 1995; Tuthill *et al.*, 2009). In FMDV infected cells, Golgi protein markers were previously shown to be dispersed (Midgley *et al.*, 2013); however, our preliminary data from Chapter 3 suggested that the Golgi membrane marker was preserved during infection. In Chapter 4, we have demonstrated that the presence of vesicles, both single and double membranes, are indicators of site of viral replication. They are referred to as replication organelles (RO) and are discussed earlier in Chapter 1.6 (Novoa *et al.*, 2005; Hsu *et al.*, 2010; Romero-Brey and Bartenschlager, 2014). These vesicles are important features to be investigated and their potential association with virus particles can be studied using cryo-EM.

Cryo soft X-ray tomography (cryo-SXT) enables a relatively large area to be imaged and analysed. In cryo-SXT, a series of 2D cellular projections of the cells is recorded at discrete angular increments, resulting in a tilt series, similar to cryo-ET

(Harkiolaki *et al.*, 2018). These are then aligned, and reconstructed generating 3D volumes of the cells called tomograms. Image formation in the X-ray microscopes is achieved by a Fresnel zone plate that can focus soft X-rays, and the maximum resolution achievable in the image depends on the outermost zone width (at Diamond B24 the resolution limit is typically either 25nm or 40nm) (Gorelick *et al.*, 2011). Thus, this method should enable us to observe the ultrastructural changes in 3D, in infected cells.

As mentioned in previous chapters, FMDV requires a high containment facility, therefore we used a surrogate model, Equine rhinitis A virus (ERAV). Aphthoviruses have a capsid roughly 30nm in diameter which encapsidates the single-stranded RNA genome. ERAV particles, like FMDV, are acid labile, which leads to the dissociation of their capsids at the low pH used when preparing chemically fixed EM samples (see Chapter 4). Cryo-preservation of infected cells can avoid these issues and helps maintain the cells in a close-to-native state. Samples are vitrified through plunge freezing into a liquid cryogen, which is liquid ethane in this study. Cryo-fixation of biological material has the advantage of preserving material with minimal perturbation to the ultrastructure of the cells thus preserving the material in a near-native state. Furthermore, cryo-preservation methods offer the potential of analysing key processes in unprecedented molecular details (Weissenberger, Henderikx and Peters, 2021).

In this chapter, we examine our ERAV infected cells in cryo-soft-X-ray (SXT) to observe the overall ultrastructural changes of an infected cell. We then discuss our rationale in optimising sample preparations for cryo-ET data collection. We present data generated from cryo-FIB milling and cryo-ET to investigate how newly assembled viruses associate with remodelled membranes in cells.

5.2. Cryo soft X-ray tomography to examine overall change in infected cells

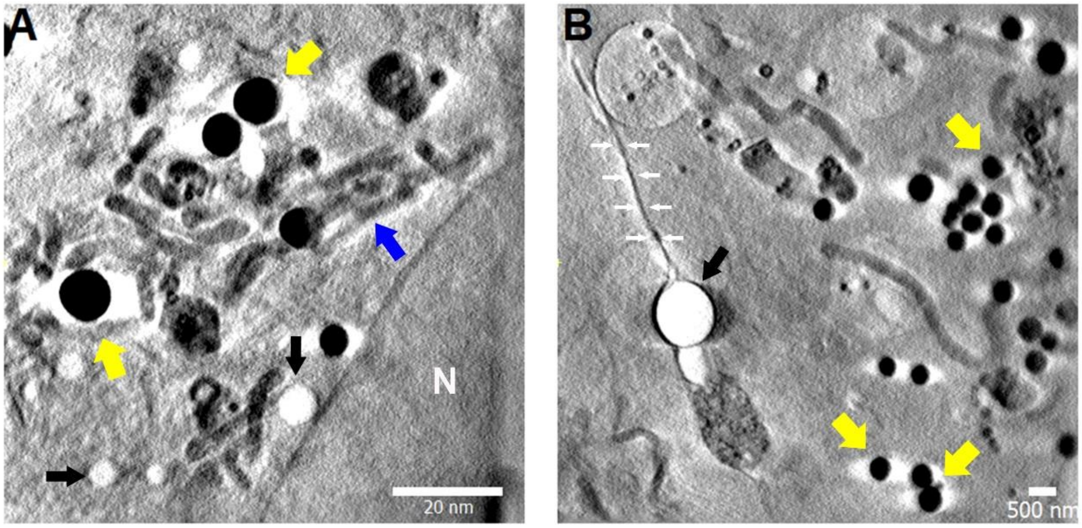

Figure 5.1 Soft-X-ray reconstruction of ERAV infected Vero cells.

Uninfected cell (panel A) shows various organelles including mitochondria (blue arrow), lipid droplets (yellow arrows) and vesicles (black arrow) within the cytoplasm. There are small clusters of lipid droplets and mitochondria in the cytoplasm. In infected cells (panel B) a vesicle was potentially being secreted and captured between two cell plasma membrane (white arrow). No virus particles were observed in the infected cells (although they are at the resolution limit), and virus induced structures were not observed.

We wanted to investigate the overall change in ultrastructure upon infection with ERAV using cryo-SXT. The advantage of Cryo-SXT is that it allows a large area of the cell to be imaged potentially enabling us to observe virus induced ultrastructural changes. This is because the penetration depth of X-rays is much higher than electrons and can be up to few microns. Therefore, cryo-preserved cells could be imaged at close-to-native state. As described in Chapter 2.10.3, cells were imaged at an X-ray energy of 500eV, with a detector pixel at 10nm and a maximum resolution of approximately 25nm using a Fresnel zone plate. A 25nm zone plate could potentially allow us to resolve our 30nm virus particles. We then analysed the timecourse of ERAV infected Vero cells. Based on our preliminary experiments, we decided to collect data at 8h, 9h and 11h post ERAV infection as described in Chapter 4.2.1 and discussed in more details later in section 5.3.2. Tilt series were collected from -60° to +60° at angular increments of 0.5° and 1° respectively. Tilt series then underwent the automated processing pipeline at B24 that aligns and reconstructs the tomograms simultaneously during data collection. We then examined these reconstructed tomograms and the ones intended for further analysis were manually re-aligned and reconstructed as the pipeline does not always reconstruct tomograms optimally.

We compared our uninfected cells and infected cells, and we observed an abundance of mitochondria and lipid droplets and various vesicles in the cells, but with no noticeable difference between the two samples (Figure 5.1). We infected Vero cells at an approximate MOI 10. Canonical signs of ERAV infection previously determined in our conventional TEM analysis (Chapter 4), such as the presence of SMV and DMVs were not detected using this method. At the resolution achievable in soft-SXT, we were not able to identify ERAV particles in the tomograms generated from the infected Vero cells (Figure 5.1B). Without the use of a fluorescent-tagged virus for ERAV, this made confirmation that the cells, and the areas of those cells that we imaged, extremely difficult.

In summary, we examined ERAV infected cells, both virus-induced structures and virus particles, were not observed. We concluded that cryo-SXT had inadequate resolving power to localise assembly sites in the cytoplasm or cells imaged were not infected. Therefore, a higher resolution imaging method was pursued with the aim to detect virus particles in infected cells.

5.3. Optimising cryo-EM samples

Cryo-EM has been used to study virus structure and explore molecular mechanisms such as uncoating and replication (also reviewed in Belov et al., 2012), including enteroviruses such as poliovirus (Dahmane *et al.*, 2022), enterovirus-71 (EV71) (Shingler *et al.*, 2013) and coxsackievirus A6 (CV-A6)

(Büttner *et al.*, 2022). Picornavirus particles are relatively small and the resolution from a soft X-ray microscope did not appear sufficient to detect such small particles (section 5.2). However, by analysing thin sections of cells in cryo-ET it should be possible to resolve 30 nm virus particles.

To investigate *in vivo* visualisation of virus particles and membrane rearrangements, we carried out a preliminary experiment using cryo-EM. Initially, we used the same conditions we used to prepare our cryo-SXT samples for cryo-EM sample preparation. The samples generally had thick ice hence we were 'blind' milling as it was not clear whether we were milling precisely in the perinuclear region, where virus particles are localised, due to the lack of fluorescent marker. Moreover, not all cells would be infected at the MOI stated above. The aim of this higher resolution imaging method was pursued, as our aim was to detect virus particles in infected cells in order to elucidate the details and relationship between the localisation of particles and rearranged membranes (i.e. SMVs or DMVs). We did not detect virus particles in the preliminary cryo-ET experiments indicating that further optimisation was required. This optimisation was separated into two sections: firstly, the cryo-EM grid preparation conditions and secondly, the MOI. The aim was to maximise the chance of detecting virus particles in cells and improve the efficiency of cryo-FIB milling and cryo-ET data collection.

5.3.1. Optimisation of cryo-EM sample preparation

Data were collected using a 300kV Titan Krios III cryo-EM to improve penetration of electrons compared to 200kV. However even at 300kV the penetration depth is limited, therefore taking advantage of recent technological developments in cryo-FIB/SEM the samples analysed in the microscope were milled to a final thickness of ~200nm. This step was generating thin sections through cells (lamella) that could be analysed using cryo-ET.

We used the same conditions that we had used to prepare our sample for soft X-ray tomography to infect cells and prepare our grids. Cells were infected with an approximate MOI of 10 and blotted for 3-5 sec. These cells were milled and then imaged using a Krios. However, with these grids, the milling efficiency was low and thus the majority of lamella produced were not of sufficient quality (i.e. thin enough that cellular structures were visible in low magnification cryo-EM images prior to tilt series collection). Thus, virus particles proved difficult to observe in our early cryo-ET data collections, suggesting that our sample preparation needed further optimisation. Our hypothesis was that we needed to optimise our grid preparation protocol for cryo-FIB milling and/or infect with a high MOI to ensure a higher population of infected cells before FIB milling. There are several factors that affect the quality of the grids during the preparation stage but, the thickness of vitreous ice on grids is the most variable factor and hugely impacts on the quality of samples and ultimately the quality of data collected. There are various aspects throughout sample preparation that contribute to formation of thin ice layers, which makes the grid a good sample for cryo-FIB milling, for example, the blotting time.

The removal of excess liquids from the grids resulting in a thin film is controlled by the length of blotting time used. To optimise our sample preparation, we first needed to reduce the ice thickness around our cells. Different blotting times from 8 sec to 10 seconds were tested and those blotted with 8 seconds showed the best ice thickness. This allowed us to better identify and target our cells in the cryo-FIB/SEM. The media used in cell culture contained a lot of different sugars and nutrients for cell growth, which made the media viscous and therefore more difficult to remove. This is a crucial step as this could contribute to the formation of thick ice during freezing. To minimise this effect, we added two extra steps: manual blotting Hanks' Balanced Salt Solution (HBSS) that removed the media on the grid as a wash step before the grid was placed in the plunge freezer. This improved our sample preparation as the grids could be milled at a more efficient rate. Without these two additional steps, samples were covered in thick ice increasing the milling time significantly. In contrast, thin ice layer allowed us to identify the milling location within cells more easily in the SEM on a cryo-FIB/SEM microscope (Figure 5.2A). The cells were much more distinguishable in the Ion beam where the cell nucleus and cytoplasm could be seen more clearly (Figure 5.2B).

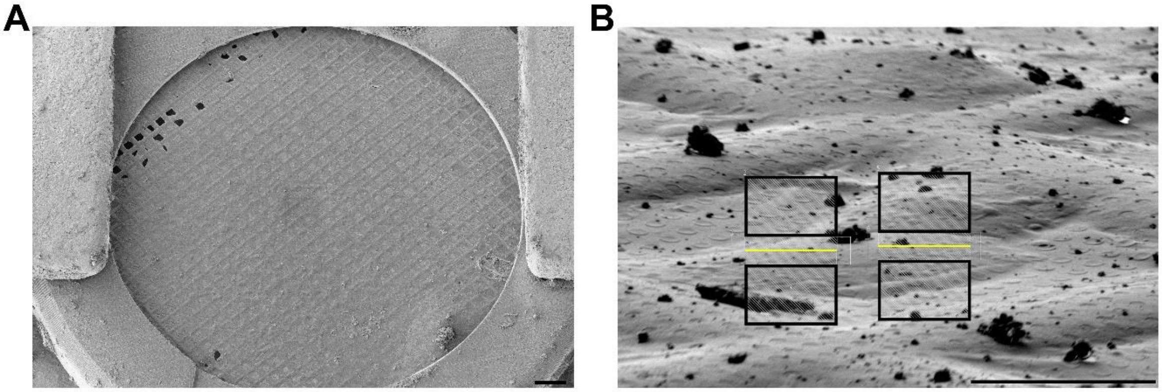

Figure 5.2 Examples of FIB-SEM and confocal images of high MOI infection of Vero cells with ERAV.

(A) SEM image of the vitrified grid prior to FIB milling. **(B)** FIB image of the vitrified cell prior to milling. The boxed area represents cellular materials to be milled and the yellow line represents the position of lamella in the perinuclear region. (Scale bar **A** = 200 μm, **B** = 20 μm)

5.3.2. Optimisation of infection conditions

Another factor that affected our sample preparation and efficiency of data collection was the inability to detect infected cells at a lower resolution during area selection. We were also limited by the lack of fluorescent markers for virus infection, as such our strategy involved targeting the lamella generation to the perinuclear region as that is where the fluorescent signals were detected with FMDV. Due to these factors, we needed to infect with a high MOI, at approximately MOI 120, to maximise the number of infected cells on the grids and increase our chances of detecting virus particles in lamella. In preliminary experiments where we infected cells with a lower MOI, we observed no virus particles in our lamella; therefore, we infected with a high MOI ensuring there was a high infection rate and that over 90% of the cells were infected. We designed anti-sera against ERAV 3A, with the aim to develop a fluorescent marker to validate our infection rate. These anti-sera were designed by our group to target either the first 35 amino acids or the amino acids from 26-60 this covers the entire 3A region of ERAV (sequence can be found in Table 2.2, Chapter 2.8.3). We tested the anti-sera that covers the first 1-35 amino acid as it gives less background noise, and for simplicity this is referred to as ERAV anti-3A hereafter. Although the background of this polyclonal antisera was still not optimal, we could distinguish some distinct 3A puncta in ERAV infected cells (Figure 5.3B). A few strong puncta appeared next to the nucleus; else they were mostly found within the perinuclear region (Figure 5.3B). However due to the high background noise, as seen in uninfected cells (Figure 5.3A), these antisera were insufficient to be used as a validation of infection rate.

To further characterise the time course of ERAV at high MOI, we carried out a preliminary experiment investigating ERAV infected Vero (monkey) cells by observing how CPE developed over time. In this preliminary experiment, we monitored the time for FMDV infected Vero and ERAV infected Vero to develop CPE. When we compared the state of CPE, we found that 3.5h post FMDV infection was similar to 9h post ERAV infection. Suggesting that the ERAV replication cycle was notably, roughly three times, slower than FMDV. FMDV 3.5hpi was known to be the optimal timepoint to study replication, as discussed in Chapter 3, hence we assumed that 9h post ERAV infection would be appropriate.

To further characterise this, we measured the total number of infectious particles, the virus titre, in our lysate using a plaque assay to generate a growth curve. The exponential phase of ERAV replication started at approximately 4hpi and continued until a plateau was reached at 12hpi. Using this data, we decided to look at the three timepoints: 8h, 9h and 11h post infection which sat late in the exponential phase where we believed that optimal replication activities would be reached (Figure 5.4). This, therefore, enabled us to study the localisation of virus particles and rearranged membranes in more detail. As expected, 9h post ERAV infection was equivalent to 3.5h post FMDV infection. We decided that 11h post ERAV infection would be our final timepoint for cryo-ET data collection because it was in the late stage of replication just before the titre plateau at 12hpi (full CPE would be observed after this timepoint). We thus concluded that collecting data at these timepoints would enable us to maximise the chance of observing assembly of virus particles and particles associated with membranes (RO).

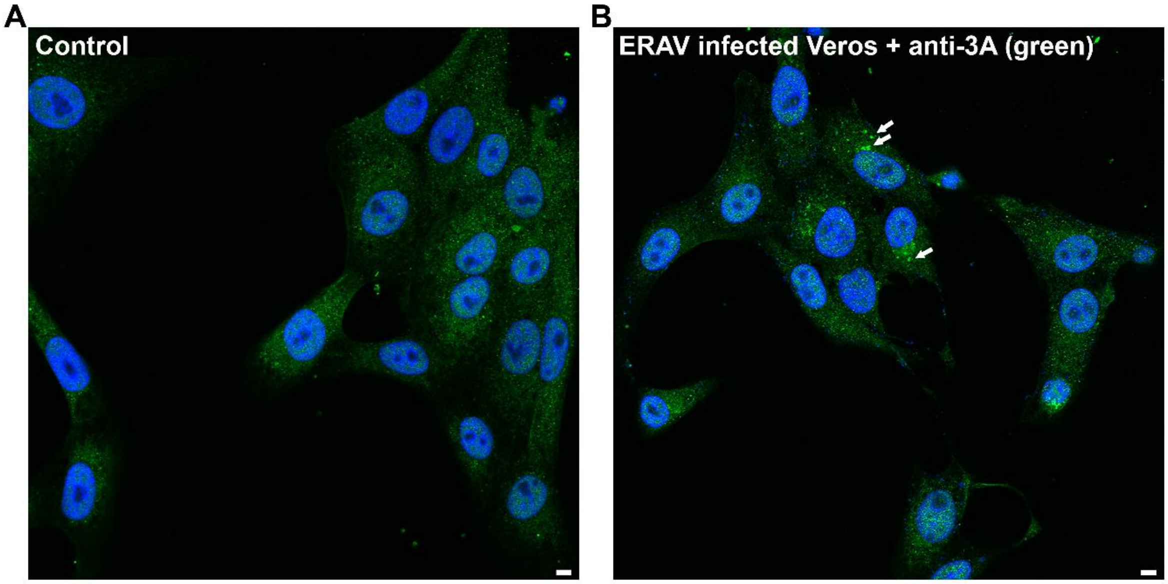

Figure 5.3 ERAV infected Vero fixed at 9 hours post infection.

(A) Uninfected Vero cells immunolabelled with ERAV anti-3A. **(B)** ERAV infected Vero cells fixed at 9hpi and then immunolabelled with ERAV anti-3A. Green puncta (3A; white arrows) appear in the cytoplasm; most strong signals appear within the perinuclear region. (Scale bar = 5 μm)

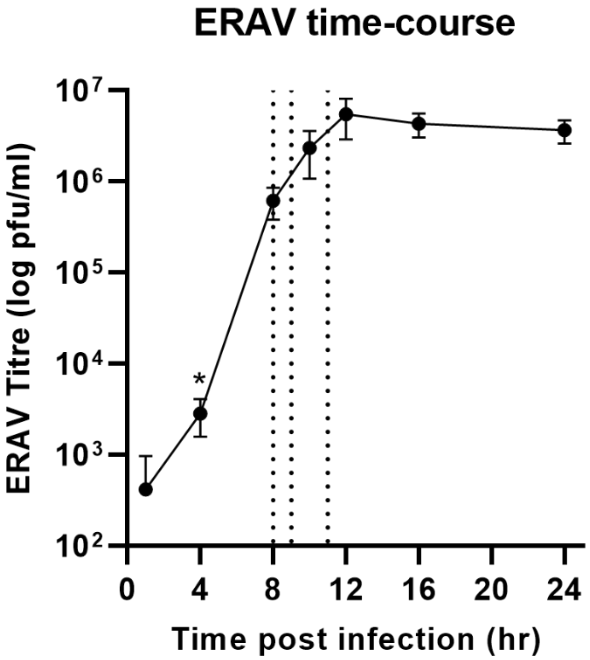

Figure 5.4 Equine rhinitis A virus (ERAV) replication time course based on pfu/ml. Supernatant and cell debris were harvested at 4, 8, 10, 12, 16, 20 and 24 hpi and titrated on Vero cells for 70 hours to produce viral plaques. Viral plaques were then stained with methylene blue and manually counted to determine the titre at each timepoint (pfu/ml). Each timepoint represented three replicates except at 4hpi (asterisk) where only two samples were available, hence one sample was used as a repeat. The dotted lines on the graph represent the three time points where our cryo-ET data were collected: 8, 9 and 11hpi respectively.

In conclusion, the anti-sera unfortunately did not work as well as expected, and our observations from the CPE experiment can confirm that infecting at this high MOI ensures a high infection rate as full CPE would be seen after 12hpi. The virus growth curve further reassured us that we are looking at timepoints that should enable us to visualise virus particles and rearranged membranes. Lastly, we optimised conditions for cryo-EM grid preparation, hence improving the pipeline to routinely perform cryo-EM on samples of infected cells. We then continued to prepare samples using conditions described in this section to collect our cryo-ET data.

5.4. Cryo-ET visualisation of ERAV infected cells

As described earlier in this chapter, the resolution that could be achieved in cryo-SXT was insufficient for us to detect ERAV particles. Thus, cryo-ET was preferred as it would overcome this issue. However, initially we noticed that the detection of these small particles in either high defocus, low dose, and low magnification search images or in the low dose tilt projections from the tilt series were extremely difficult. In fact, later in the study, we established that virus particles were only visible after the tilt series were reconstructed. Hence, without the fluorescent markers, it became increasingly important to ensure a high MOI infection to maximise the chances to observe virus particles and virus-induced structures in cells, which means a high throughput to produce data. We collected tilt series on a Titan Krios at eBIC using Tomo5 (Thermofisher Scientific), the microscope settings can be found in Table 5.1. These tilt series were corrected for the effects of the contrast transfer function (CTF) and reconstructed using WARP (Tegunov and Cramer, 2019)(Tegunov and Cramer, 2019). Resolution of the reconstruction was limited by the Nyquist frequency, which is half the sampling frequency of the imaging detector and is dependent on the magnification used. Our data was collected at 42k, at pixel size of ~3Å with the aim to detect virus particles, hence our Nyquist limit was 6Å. Following the optimisation of sample preparation and data collection, we successfully detected virus particles and virus induced rearranged membranes in our tomograms. We will present our data in two sections; we will first describe a sub-tomogram model reconstructed from our data in section 5.4.1. Then we will discuss about the virus particles observed in our tomograms and their association with membrane structures in section 5.4.2.

Table 5.1 Microscope settings

Microscope: Titan Krios III
Detector: Selectris Falcon IV
Accelerating Voltage: 300kV
Nanoprobe
Dose symmetric
C2 Aperture: 50 µm
Magnification: 42K
Pixel size ~2.9Å/pixel
Slit: 5eV
Tilt increment: 2
Tilt span: ±50°
Acquisition software: Tomo5

5.4.1. 3D model of intracellular ERAV

From our cryo-ET data, one of the outcomes was reconstructing a sub-tomogram 3D model of ERAV particles *in vivo*. Tomograms of infected cells were collected at 8hpi, 9hpi and 11hpi. Tomograms were reconstructed in WARP (Tegunov and Cramer, 2019). The defocus of the raw tilt data was estimated in WARP and outliers were deselected prior to stack alignment in IMOD. We then used a script that automates alignment of multiple stacked tilt series generated from WARP via patch tracking in IMOD (Kremer, Mastronarde and McIntosh, 1996). The contours were traced, and the residual error and mean were refined to a value ≤1.5nm. Stacks that reached the refinement limit were then returned to WARP for further processing or else reassessed in WARP to regenerate tilt series for alignments. Aligned tilt series that were reimported into WARP were reconstructed and denoised. Virus particles were then manually picked from the tomograms in IMOD. Virus particles were mostly detected in tomograms of infected cells at 11hpi with the exception of one tomogram at 9hpi that contained over 100 virus particles. The final data set contained 14 tomograms (listed in Table 8.1, Appendix), that gave the best alignment statistics and had clear virus particles. After manual picking of the virus particles, their coordinates were used to extract sub-tomograms in WARP. The sub-tomograms were then imported into RELION 3.1.2 (Zivanov *et al.*, 2018). Virus particles were separated by alignment and classification based on the presence or absence of RNA density in the centre of the sub-tomograms. There were two different classes of full particles identified, the outer density of the virus capsid was better defined in the first class of full virus particles (Figure 5.5A) compared to the second class of virus particles (Figure 5.5B). Moreover, the central density, which represents the RNA density seemed more structured in the first class of virus particles (Figure 5.5A-B). Empty particles would have much reduced density inside the capsid (Figure 5.5C). These three maps were then imported into M (Tegunov *et al.*, 2020), and further refined. Approximately 45 particles were extracted from a single tomogram from our best lamella which had a thickness of ~120nm. After M refinement and reconstruction, 45 full particles from this tomogram yielded a 3D reconstruction at a resolution of 7.2 Å, which was close to the Nyquist frequency of the dataset (6 Å) (Figure 5.5D). Interestingly, RELION 3D classification identified two classes of full particles; 45 full particles gave the high-resolution structure and the second class of virus particles containing 52 particles from the same tomogram had a much lower resolution (Figure 5.6). Details of the capsid could be clearly resolved in the higher resolution full class when compared to lower resolution full class. In addition, the lower resolution full class did not present any internal densities (Figure 5.5D and Figure 5.6). Due to the limited resolution of the second class of full particles, we were unable to determine if there was a significant difference in the capsid structure of the two classes of full particles.

We were able to take a deposited model for native ERAV, determined by X-ray crystallography (PDB ID 2WFF; Tuthill et al., 2009) and rigid-body dock this into our 7.2 Å electron density map (Figure 5.7A). The excellent agreement confirmed that the X-ray structure is an accurate representation of the *in-situ* structure of ERAV. The empty particles from this tomogram yielded a lower resolution reconstruction, therefore, we pooled all particles across the tomograms to further refine them. 127 empty particles were extracted, and put through two rounds of classification in RELION and further refinement in M. The refinement limit was reached, and the final structure yielded an 11.5 Å map (Figure 5.5E). Again, the X-ray structure for ERAV (PDB ID 2WFF) was rigid-body docked into our 3D model for confirmation (Figure 5.7B). The capsid proteins VP1 (blue), VP2 (green), VP3 (red) and VP4 (yellow) were coloured accordingly (Figure 5.8A). Lumps were observed internally in our reconstruction. The crystal structure did not fit into these empty regions (Figure 5.8B). This is the first time that these additional densities have been observed for ERAV. We then compared our full ERAV and empty STA ERAV models. In the full ERAV particle, the RNA was potentially in contact with the capsid, where these contact sites were seen in a similar location to the empty lumps (Figure 5.9). Hence, this suggested to us that we are seeing potential RNA contact sites in *Aphthoviruses* in situ. These contact sites would appear to be present in VP0 since the density appears adjacent to VP4 in the fitted model corresponding to uncleaved VP0 in these empty capsids. Lastly, the pooling of the full particles could only be refined to 8.5 Å suggestive of some heterogeneity. The pool of full particles did not reach the resolution of the first class of full particles refined to 7.2 Å, therefore the other class of full particle structures were probably heterogenous reflecting capsid rearrangements or dynamics.

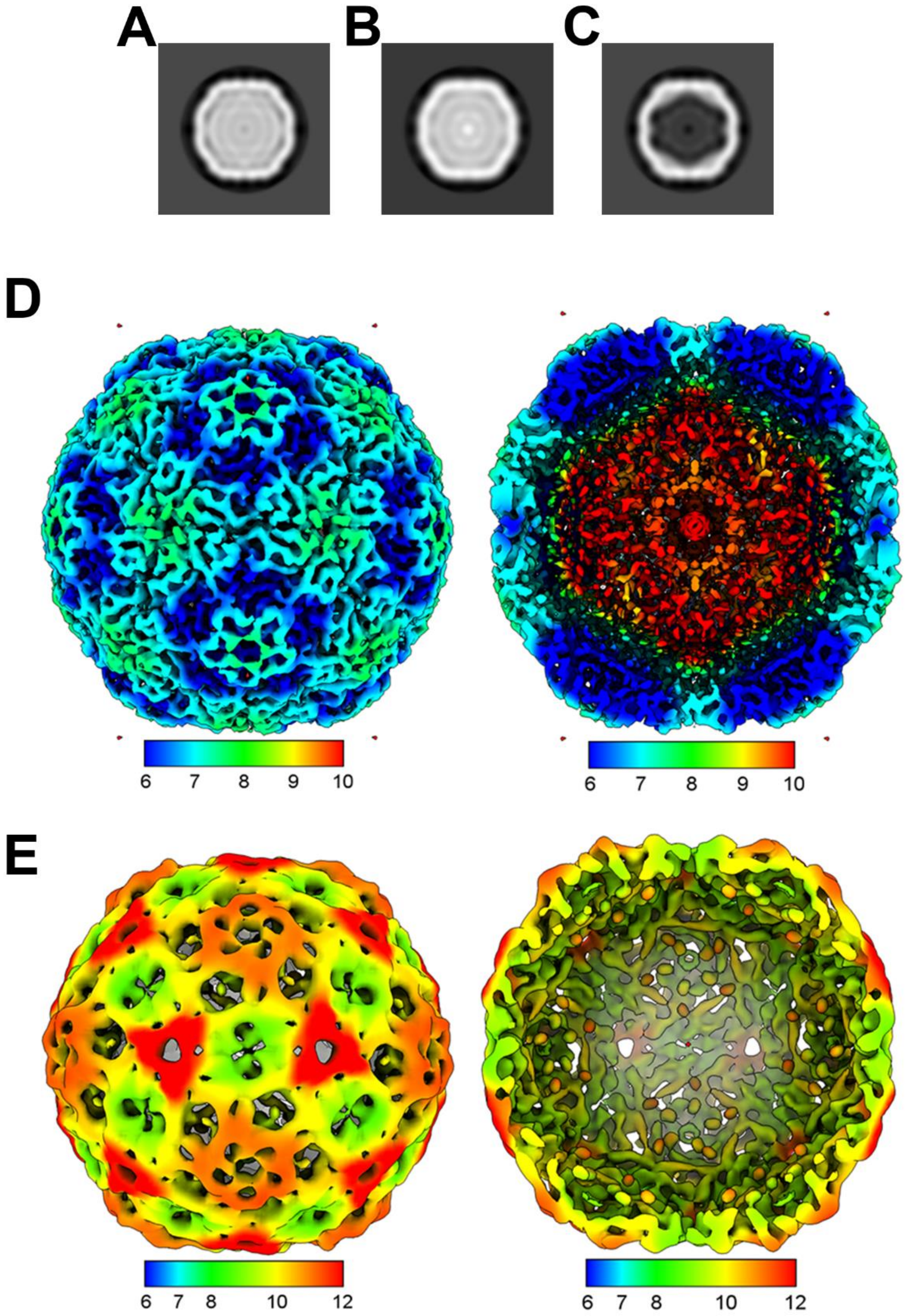

Figure 5.5 Overview of sub-tomogram averaged reconstructions.

(A-C) 3D classification of particles from one tomogram. Panel **A** represents the class of full particles that gave a 7.2 Å reconstruction. Panel **B** presents the second class of full virus particles identified in RELION while panel **C** represents the empty particles. **(D)** Map of the intracellular ERAV full particle at 7.2 Å obtained from one tomogram with front and mid-section views. **(E)** Map of the intracellular empty virus particle pooled from 14 tomograms at 11h post infection which gave an 11.5 Å reconstruction, both front and mid-section view presented. (Scale bar based on resolution in Angstrom).

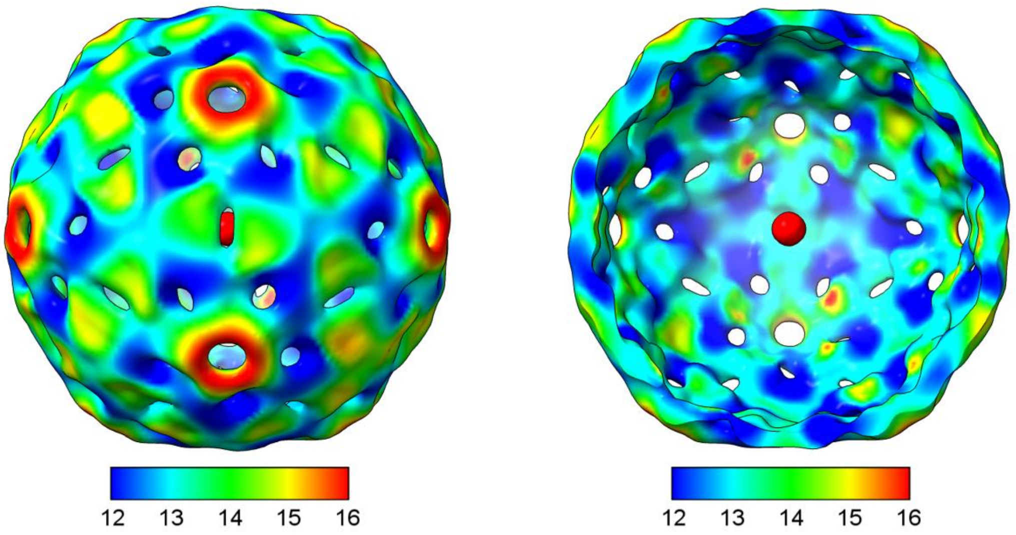

Figure 5.6 ERAV full particle reconstruction at 17.5Å.

Map of the second class of intracellular ERAV full particle reconstructed at 17.5Å with front (left panel) and mid-section view (right panel). (Scale bar based on resolution in Angstrom.)

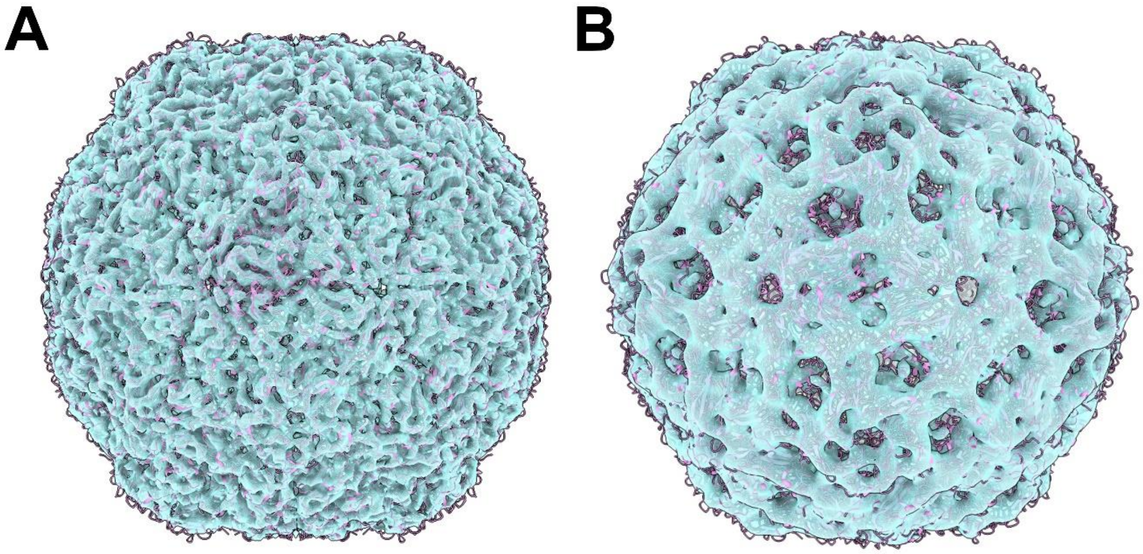

Figure 5.7 ERAV 3D reconstruction with X-ray crystal structure (PDB ID 2WFF) docked in.

Panel **A** shows the ERAV full particle reconstructed at 7.2Å with X-ray coordinates docked in. Panel **B** shows the ERAV empty particle reconstructed at 11.5Å with X-ray coordinates docked in.

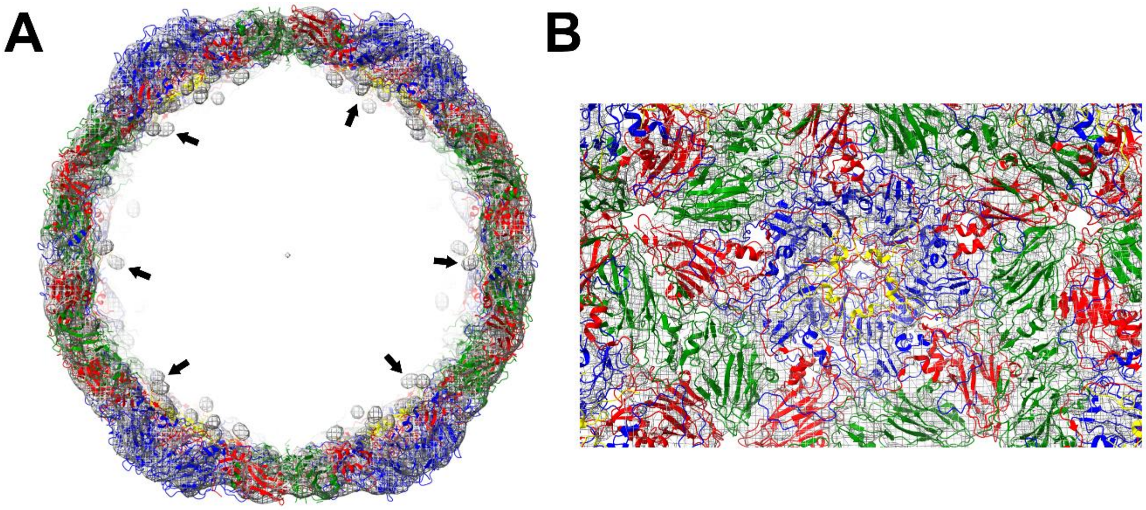

Figure 5.8 ERAV empty particle reconstruction.

ERAV coordinates were docked into the empty ERAV particle reconstructed at 11.5Å showing VP1 (blue), VP2 (green), VP3 (red) and VP4 (yellow). Empty lumps (black arrows) are observed in this slice through the reconstruction (Panel **A**). A close-up view down the icosahedral five-fold axis from the inside of the particle is shown in panel **B**.

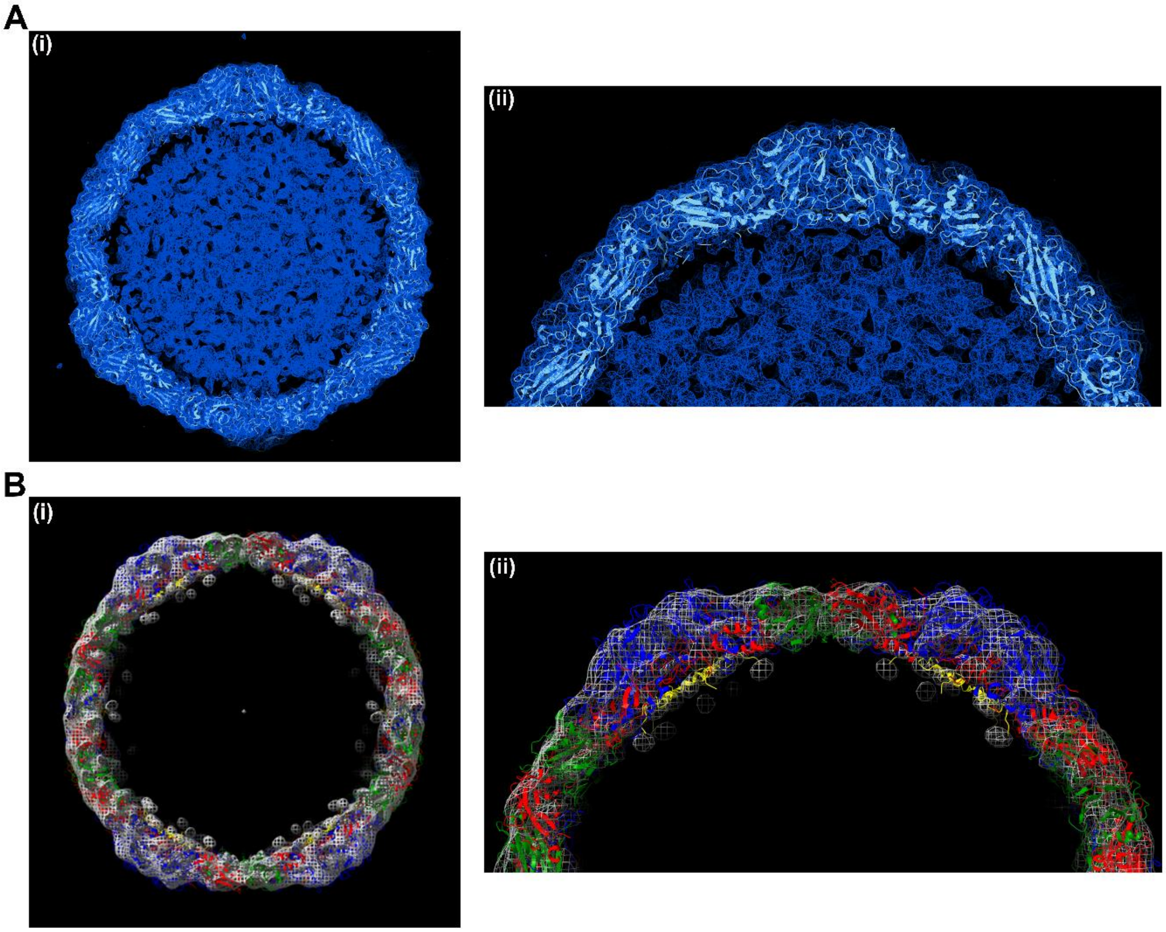

Figure 5.9 Comparison of potential RNA contact sites in full and empty ERAV particle.

(A) Full ERAV particle mid-section view down the icosahedral 3-fold axis with X-ray crystal structure docked in (PDB ID 2WFF). In panel (i), RNA inside the capsid potentially is in contact with the capsid, near the five-fold. (ii) Magnified view. **(B)** Empty ERAV particle mid-section view down the icosahedral 2-fold with X-ray crystal structure docked in (PDB ID 2WFF). Capsid proteins are coloured: VP1 (blue), VP2 (green), VP3 (red) and VP4 (yellow). In the absence of RNA, some empty density features were identified in the vicinity of VP4 possibly corresponding to an unmodelled residue(s) in VP0 in the region of RNA contacts with the capsid. (ii) Magnified view.

5.4.2. Virus induced membrane structures tethered to virus particles

Three classes of particles were seen in the tomograms

We then manually quantified the number of virus particles collected across timepoints from 8hpi to 11hpi. These particles were manually partitioned into three classes: full, partially full, and empty based on the difference in their central density. Full particles showed a dense inner structure compared to empty particles (Figure5.10A, B and D). The partially full particle was defined by the appearance of a ‘genomic-like’ structure inside the capsid (referred to as the genome hereafter; Figure 5.10C).

In the late stage of enterovirus replication, equivalent to 6hpi, the rearrangement of cytoplasmic membranes to support replication was significant and there was a substantial increase in empty and full enterovirus particles (Dahmane *et al.*, 2022). Enterovirus capsid assembly occurs on membranes and half capsid intermediate were observed on membrane surfaces with luminal density (Dahmane *et al.*, 2022). In addition, both empty and full enterovirus particles were seen to have densities that tether them to the membranes (Dahmane *et al.*, 2022). Based on this we hypothesised that partially full particles could be either intermediates during assembly of particles or during disassembly/uncoating stage in late replication. Firstly, our data reassured us that ERAV replication was much slower than FMDV. We observed an increase in empty particles over time: there were no empty virus particles observed at 8hpi; full and empty virus particles were observed at 9hpi. Partially full particles seen at 8hpi might suggest that virus particles were assembling. Assembly then formed both RNA loaded virions and empty particles at 9hpi, where the peak timepoint was reached. There was an exponential increase in the number of virus particles at 11hpi (Figure 5.10E). A small data set was analysed in this study, especially information available at earlier timepoints was limited, however a notable increase in the number of both partially full and empty particles across timepoints was observed. The current model being proposed to explain this trend was that we captured a number of viruses in the process of uncoating towards late timepoint. Another possible explanation is that we see an accumulation of empty particles due to cellular materials associated with replication was being used up and hence they cannot make any further genome to produce RNA-loaded virions.

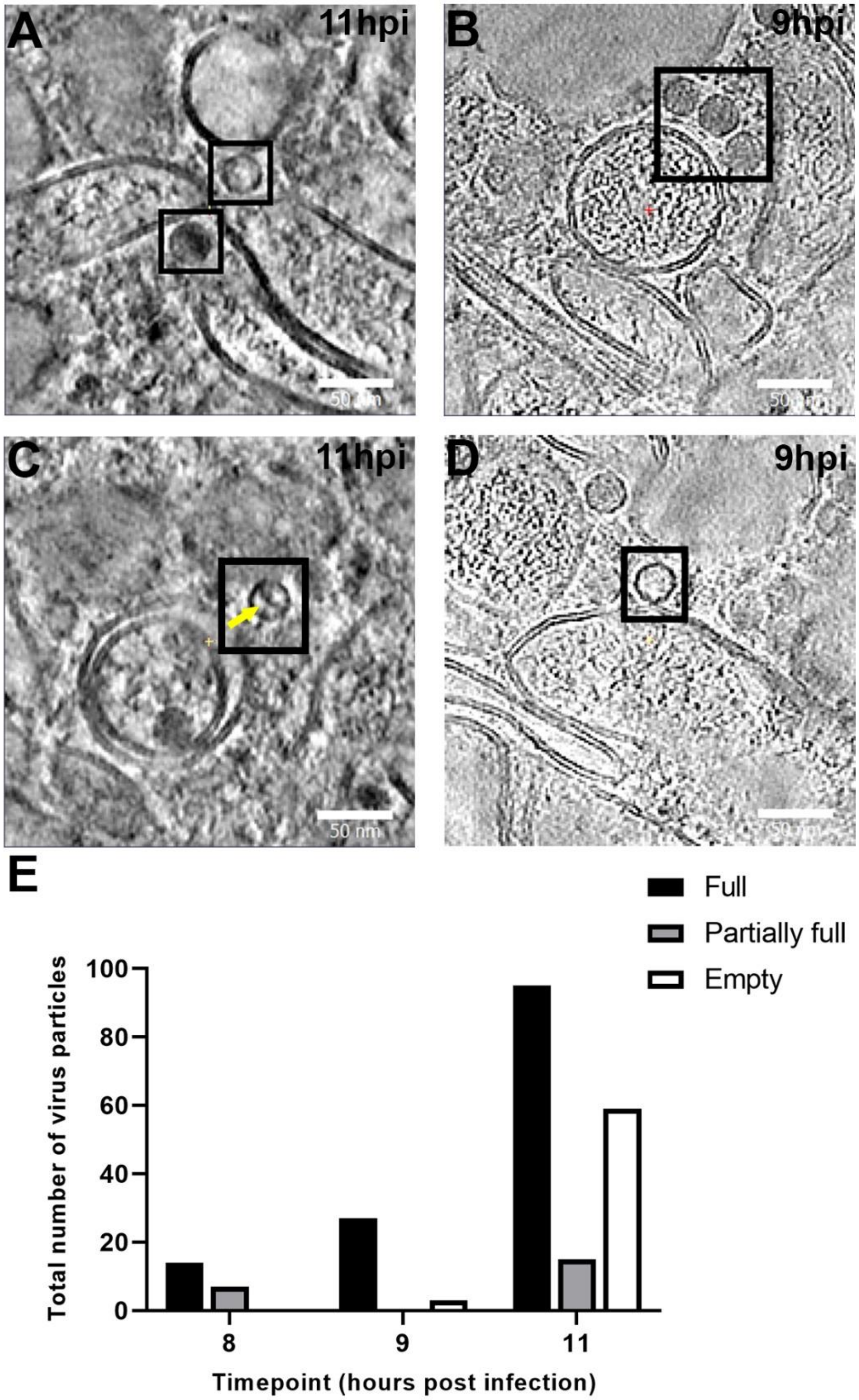

Figure 5.10 Overview of three classes of virus particles.

A-D Example tomograms of the three classes of virus particles: full, partially full and empty particles (boxes highlight the virus particles). These are defined based on the differences in density level within the capsid. Panels **A** and **C** are tomograms slices from ERAV infected cells at 11hpi whereas panels **B** and **D** are tomogram slices from ERAV infected Vero cells at 9hpi. In Panel **A**, the boxes highlighted one empty (top) and full (bottom) particle sitting opposite to each other. Panel **B** presents examples of full particles aligning to the cytoplasmic side of the single membrane structure, although the lower particle looks partially assembled. Panel **C** is an example of a partially full particle, where the inner density is empty but contains genome-like structure (yellow arrow). Panel **D** represents a classic example of empty particle tethered to a single membrane structure. Scale bars are 50nm. **(E)** Graph presenting the total number of virus particles at 8hpi, 9hpi and 11hpi that were manually counted. There is an increase in empty particles over time while partially full particles were not observed at 9hpi.

Double membrane vesicles and autophagic membranes

As previously mentioned, the predominant cellular features in our data were single membrane structures or single membrane vesicles. Most of our information related to membranes organisation came from 11hpi, as more virus particles and associated remodelled membrane structures were observed. We are yet to observe a trend in the increase in complexity of vesicles over time, perhaps in part due to a limited data set. Nonetheless, we find that the number of single membrane vesicles seen at a late replication timepoint is abundant compared to DMVs, especially those tethered to virus particles. This suggests to us that there is potentially a difference between ERAV and poliovirus infection.

We then looked at the DMV as it is a unique feature in picornavirus infection. Enteroviruses induce the formation of vesicles by rearranging cytoplasmic membranes; and overtime there is an increase from single membrane to DMVs (Belov et al., 2012). Enterovirus assembly and replication mainly occur on replication membranes, for example, the intermediate capsid was seen to be tethered to both SMVs and DMVs (Dahmane *et al.*, 2022). Also, it was suggested that full/RNA-loaded virions were selected to be secreted in autophagy like membranes i.e DMVs (Dahmane *et al.*, 2022). Our data showed a slight difference. We observed fewer DMVs, and we did not see a high number of virus particles being engulfed into the DMVs. Empty and full virions appeared both on the luminal and cytoplasmic side of the DMVs (Figure 5.11 A-C). We have seen two examples of empty virions inside DMVs; one was potentially being engulfed (Figure 5.11D) while the other DMV contained two empty particles (Figure 5.11E). Contrary to what was suggested for poliovirus, that only RNA loaded virions were selected for secretion (Dahmane *et al.*, 2022), we have observed that both full and empty virions can be found inside DMVs. It was proposed that engulfment and secretion has favoured RNA-loaded virions and suggested that autophagic membranes play an important role in the virus life cycle (Dahmane *et al.*, 2022). We observed various potential autophagic membranes, one was likely to be engulfing the virion (Figure 5.12A). Virions were also tethered to the autophagic membrane (Figure

5.12B). We have observed an infected cell at 11hpi that contains a significant number of autophagic-like structures (Figure 5.12E, magnified examples in Figure 5.12C-D).

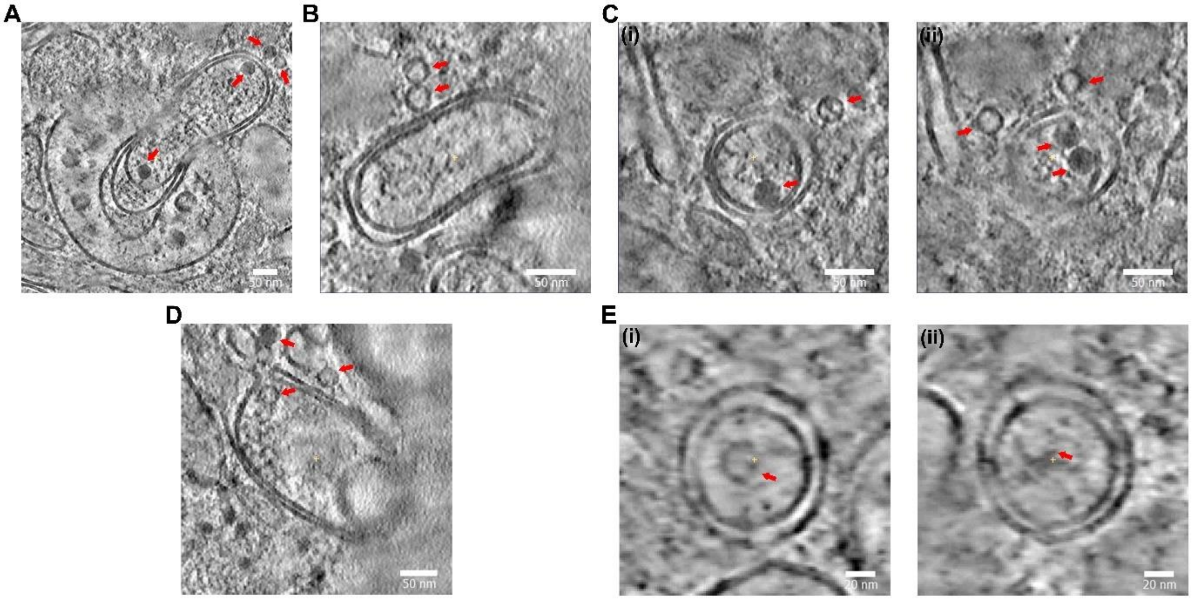

Figure 5.11 Double membrane vesicles induced by ERAV that are tethered to ERAV virions at 11hpi.

(A) DMV being surrounded by a lysosome like structure. There were two full virions recorded inside the DMV. An empty and full particle were seen tethered outside the DMV. (Scale bar = 50 µm) **(B)** Two empty virions were tethered to the DMV. (Scale bar = 50 µm) **(C(i) and (ii))** There were three full virions observed in the DMV. This DMV was also surrounded by three other virions, with one partially full and one empty tethered to the membrane and another empty particle sitting adjacent to the DMV. (Scale bar = 50 µm) **(D)** This DMV could be engulfing particles in a small queue; one empty particle was inside DMV and a full virion was following that. An empty particle was then tethered to the DMV.

(Scale bar = 50 μm) **(E(i) and (ii))** Two empty particles were recorded inside a DMV. (Scale bar = 20 μm)

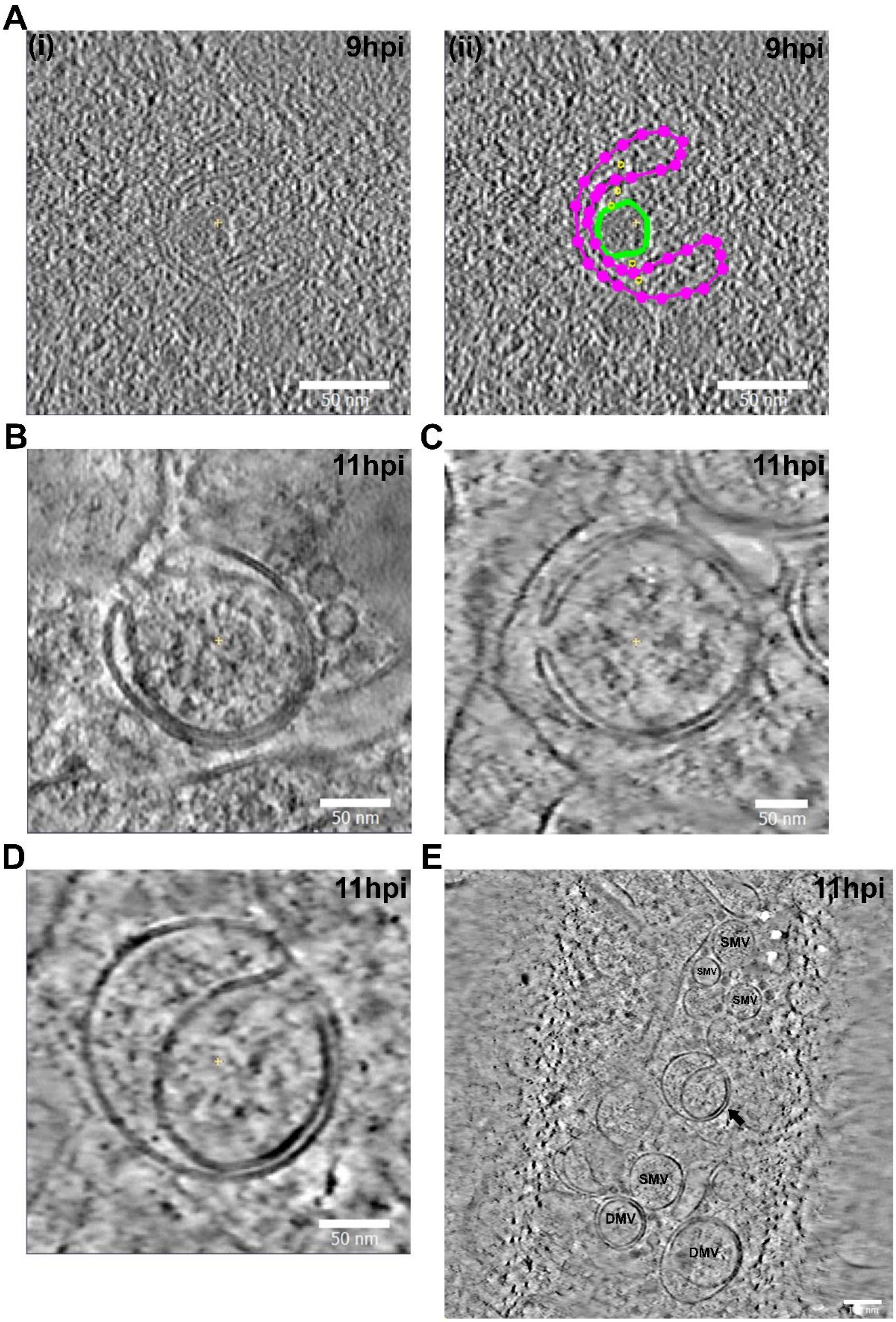

Figure 5.12 Potential autophagic membranes recorded at 9hpi and 11hpi.

(A) Both panels are example from the same tomogram in ERAV infected Vero cell at 9hpi. the same structure with the segmented model displayed on (ii), purple represents the membrane structure and green the outer diameter of the capsid structure. This full virion appeared to be engulfed by the potential autophagic membrane (Scale bar = 50 µm) **(B-E)** Examples of autophagic membranes in ERAV infected Vero at 11hpi. **(B)** Two virions were tethered to this autophagophore-like structure at 11pi (Scale bar = 50 µm) **(C)** Magnified view of an autophagophore captured at 11hpi. No virus was seen inside or tethered but unknown luminous densities were recorded inside this structure (Scale bar = 50 µm) **(D)** Magnified view of an autophagophore-like structure at 11hpi (Scale bar = 50 µm) **(E)** Lamella recorded at 11hpi where various virus induced structures including SMV and DMV were seen. There were also various autophagophore captured within this cluster of rearranged membrane structures. (Scale bar = 100 µm)

Distance between membrane and virus particles

We pooled all the particles based on the classification in RELION. The overall aim of this analysis was to investigate the differences in the distance between virus particles and their tethered or associated membranes. We segmented the membranes from an ERAV infected Vero cell at 11hpi using EMAN2 (Tang *et al.*, 2007). The coordinates of the empty particles and the two classes of full particles: the class that gave a high-resolution reconstruction at 7.2 Å (full1) and the class that gave a lower resolution reconstruction of full virus particles (full2), were extracted from IMOD. These were then presented in ChimeraX where the distance between virus particles and membranes was measured. In this segmented tomogram, there was a small cluster of SMVs next to a mitochondrion, most of the virus particles were aligned along the outer surface of the vesicles (Figure 5.13). We then further analysed the data pooling the two groups of full particles (full1 and full2) and measured the distance between full virus particles and empty particles. We present a series of examples, both full and empty particles, that were in close proximity with the membranes in Figure 5.14A-H. We then separated these particles into one group that were closer to membranes (Figure 5.14I-N) and those that appeared to have a longer tether and appeared further away from membranes (Figure 5.14Q-R). It was shown in the enterovirus reconstruction that tethers were approximately 6nm from the membrane (Dahmane *et al.*, 2022). We measured the length of tether, the distance between the center of the virus particle and the center of the membrane, across 14 tomograms. Our analysis showed that the distance between empty particles was approximately 226Å (equivalent to 22.6 nm) while full particles were approximately 250Å (equivalent to 25 nm). Empty particles were slightly closer to the membranes compared to the full particles (Figure 5.14S). Assuming a capsid diameter of 30nm and membrane width of 4nm, the surface-to-surface tether separations are roughly 5.6 nm for empty particles and 8 nm for full particles i.e. a similar span to the tethers measured by Dahmane et al. for poliovirus (Dahmane *et al.*, 2022).

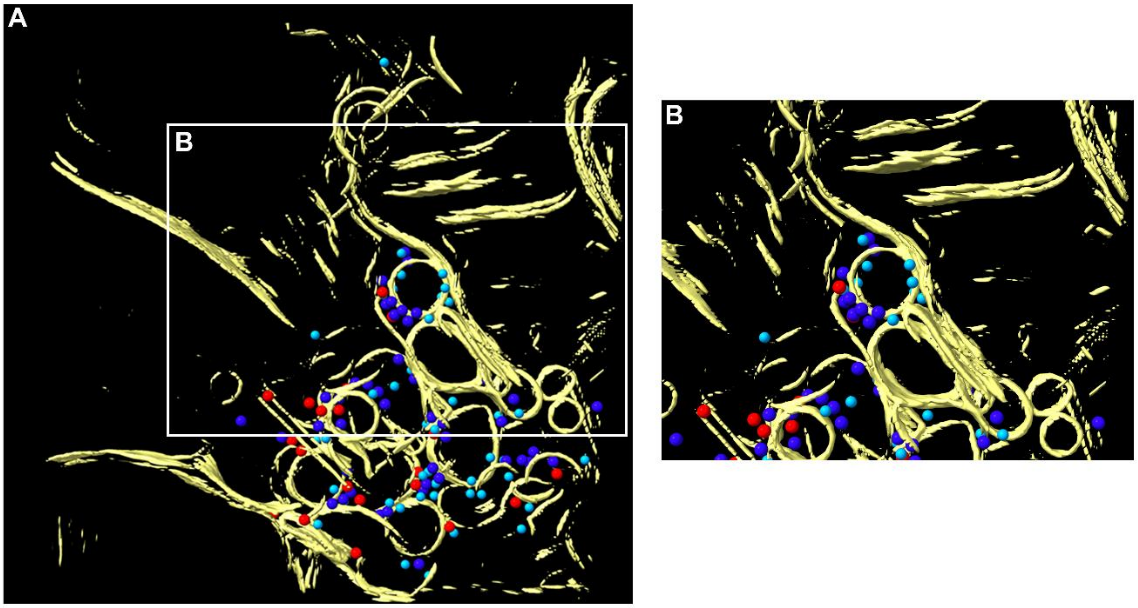

Figure 5.13 Segmentation of ERAV infected Vero at 11 hours post infection.

Panel **A** is the segmentation of membranes from lamella of an ERAV infected Vero cell at 11 hpi with virus particles coordinates docked in. Membranes (yellow) highlighted SMVs surrounded by three classes of virus particles: empty (red) and two different classes of full particles (dark and light blue respectively). Panel **B** is a magnified image of the virus particles aligning with the virus induced membrane structure.

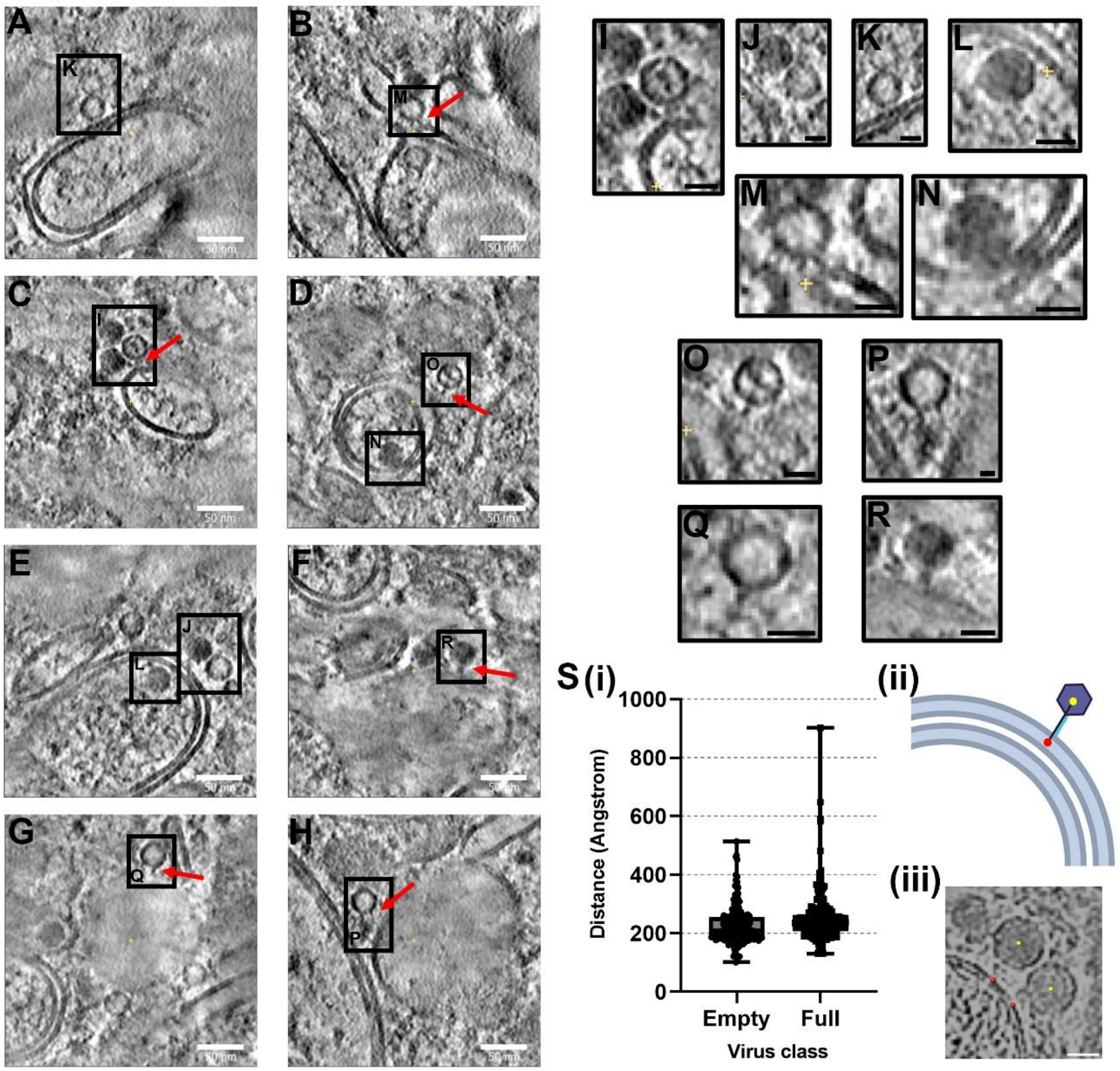

Figure 5.14 Example tomograms of virus particles tethered to membranes.

(A-H) Representative tomograms of virus particles tethered to the membrane at different distances. **I-N** represents examples of virus particles that are defined as close to membranes. **Q-R** represents examples of virus particles that are further away from membranes. **(S) (i)** Box and whisker plot showing the distribution of empty and full particles, across 14 tomograms, while the error bar shows the min and max value of the distances between virus particle and membranes in Å. Panel **S(ii)** is a cartoon schematic of how distances were measured. The center of the virus particle (yellow), where coordinates were extracted from IMOD, was docked into the tomogram and segmentation in ChimeraX, then a point was placed in the centre of the membrane (red dot), and distance was then measured in ChimeraX. An example of a tomogram slice is shown in **S(iii)**. (Scale bar **A-H** = 50nm, **Q-R** and **S(ii)** = 20nm) (**S(ii)** created with Biorender.com).

5.5. Discussion

In preliminary cryo-EM studies, two technical issues were encountered. Firstly, ice contamination that obscured views and prevented us from collecting high quality data. Secondly, the lack of virus particles seen in cells due to the lack of fluorescent marker limited our ability to target viruses and RO precisely in cryo-FIB/SEM. Both were factors limiting the size of our data set for further analysis. However, in this study, we have optimised the conditions for infection and grid preparation, a pipeline is available to routinely generate grids with a suitable thickness of ice and infection rate for cryo-FIB and cryo-ET. However, ice contamination is not only affected by sample handling, but also within the microscopes. There are various sample transfer steps between the cryo-FIB/SEM and the cryo-EM. A high vacuum is maintained in the cryo-FIB/SEM chamber, however, lamella sitting inside this chamber for several hours during milling are prone to redeposition of removed materials on the lamella.

Initially, very few particles were seen in our tomograms hence preventing us from more meaningful analysis such as STA and to demonstrate any potential link between viruses and RO. We lack a fluorescently tagged form of ERAV nsp to identify sites of viral replication, similar to the 3A-tagged FMDVs generated in Chapter 3. The lack of fluorescent signal for ERAV resulted in the ‘blind’ milling of cells. We therefore infected cells with a high MOI, however, if a fluorescent signal was present, this would greatly improve the targeting accuracy and efficiency of the lamella preparation and ultimately yield a better chance of seeing virus particles in cells for further analysis such as observing replication structures associated with virus particles. Lastly, the thickness of lamella varies in each experiment, as this is dependent on the sample preparation of grids, ice thickness that affects the milling process and the final thinning down step to polish the lamella. This was controlled between 120nm and 200nm, which should be sufficient to identify cellular structures such as vesicles in the microscope prior to data collection. This was helpful in targeting regions for data collection which maximise chances to observe virus particles. Although parameters used in cryo-FIB were consistent, lamella thickness is still a factor that limits resolution. These technical issues await for further improvements, if they were to be resolved in the future, more lamella from infected cells could be produced increasing the size of data set in cryo-ET. Alternatively, a high throughput approach is to use the automated software AutoTEM, enabling automatic milling of a large number of samples. With this approach, the target region for milling can be roughly estimated and we can aim for a thin lamella to optimise signal to noise. This would also improve the yield and chances to obtain more data increasing the size of data set for analysis.

Advances in the EM imaging field have elucidated more details on the formation and presence of DMVs during viral replication over the past decade. While other +RNA viruses such as coronaviruses induce DMVs that appear within compartments of a connected network, picornavirus induced DMVs are separated lacking this connection. Such replication details have been extensively revealed in enterovirus studies. For example, studies on enteroviruses such as poliovirus and coxsackievirus B3 have revealed the progression of how SMVs or tubules transform into DMVs (Limpens *et al.*, 2011; Belov *et al.*, 2012; Neufeldt and Cortese, 2022). In our study, SMVs predominated in the cytoplasm of infected cells, across all three timepoints, with only a slight increase in proportion of DMVs over time. This was unexpected, suggesting that a considerably large amount of single membrane vesicles induced earlier in the infection did not invaginate into DMVs as seen in studies with enteroviruses. However, this is similar to what was observed in FMDV (also discussed in Chapter 4). In FMDV infected cells, vesicles including DMVs appeared in much lower quantities and were not found in densely packed clusters (Monaghan *et al.*, 2004). Thus, this possibly suggested that there is a difference between enterovirus and aphthovirus induced membrane remodelling during infection. A possible explanation for this is the different autophagy pathways employed by the viruses. As previously explained in Chapter 1.6.1, there are variations of autophagy pathways, an example is non-canonical autophagy. Non-canonical autophagy does not require a complete set of ATG proteins to form autophagosomes. Moreover, contrary to canonical autophagy, non-canonical autophagy is a selective process that targets specific cellular substrates, an example is LC3-associated phagocytosis. This pathway is triggered by receptors present in extracellular pathogens such as bacteria and viruses. It recruits SMVs which later conjugate with LC3 prior to lysosomal fusion and degradation. Hence, it is likely that aphthoviruses utilise non-canonical pathway, as SMVs were the predominant feature observed in infected cells, whilst enteroviruses may utilise canonical autophagy which explains abundance of DMVs observed in enterovirus infected cells.

As mentioned earlier, non-canonical autophagy is a selective process, and it is likely that aphthoviruses utilise this pathway. A recent study suggested that enterovirus induced autophagy-like membranes undergo this process of selective autophagy for non-lytic release of RNA-loaded virions only (Dahmane *et al.*, 2022). Could this selective mechanism potentially reveal how the virus maximises infectivity by exporting RNA-loaded virions only? Do aphthoviruses utilise the same mechanism to maximise infectivity? In our study, we observed a small quantity of DMVs. The virions found inside the DMV were not exclusively ERAV virions. A couple of examples showed an empty particle possibly in the process of entering a DMV and a full virion potentially being engulfed by an autophagic membrane. With our limited data set, we could not define whether selective autophagy occurs in aphthovirus replication, but this may be a difference between entero- and aphthovirus infection. In the enterovirus study, they observed an accumulation of full virions after inhibiting ULK1/ULK2 protein kinases, which are important kinases in initiating canonical autophagy (Petherick *et al.*, 2015; Dahmane *et al.*, 2022).

However, we have not used any inhibitors to investigate the extracellular virus titres over time. This could perhaps be used in the future as it gives an indication of whether there were RNA-loaded virions exported earlier in the time course leaving empty particles. This possibly could explain the observation of the accumulation of empty particles over time. Some of the full virions potentially could have been secreted earlier in the replication cycle and if this occurred, we could then see a build-up of full virions in infected cells when inhibitors are used. Although, non-lytic release of infectious virions only accounts for a minority of infectious virions. There has been increasing evidence showing the autophagy pathway assists viral replication and that potentially supports non-lytic release of virions (Jackson *et al.*, 2005; Kirkegaard and Jackson, 2005; Taylor and Kirkegaard, 2007; O'Donnell *et al.*, 2011; Dahmane *et al.*, 2022). If this happens early in the infection, it would probably protect cells from lysing and thus contribute to a more efficient and successful infection.

Although selective autophagy for enteroviruses is being proposed, the exact mechanism is still unknown. If selective autophagy takes place, could this suggest that there are differences in the capsid structure which are used to trigger this selection? We have identified two classes of full virions; one was at a lower resolution preventing further analysis to identify the differences between the two classes. The low resolution of the second class of full particles suggested that there were some limiting factors imposed during alignment and reconstruction. One possibility is that the full particles within this class were damaged, for example during FIB milling they were damaged by the ion beam. Half capsid checkpoints were previously captured in enterovirus replication, i.e. an intermediate form of capsid formed during assembly (Dahmane *et al.*, 2022). Therefore, could the second possibility be that the second class of full particles were heterogenous and may contain viruses in different conformations, perhaps suggesting they were undergoing different processes such as assembly? Unfortunately, separating out conformational changes was not possible due to the small size of data set. Either of these possibilities would result in a disordered structure and therefore limited resolution of the final average. We have also seen full virions inside and outside DMVs. Could they represent the two different classes of full particles? This could be further investigated with a larger data set where further classification of the virus particles could potentially reveal more details on the different structure of the full particles and enable us to make a comparison.

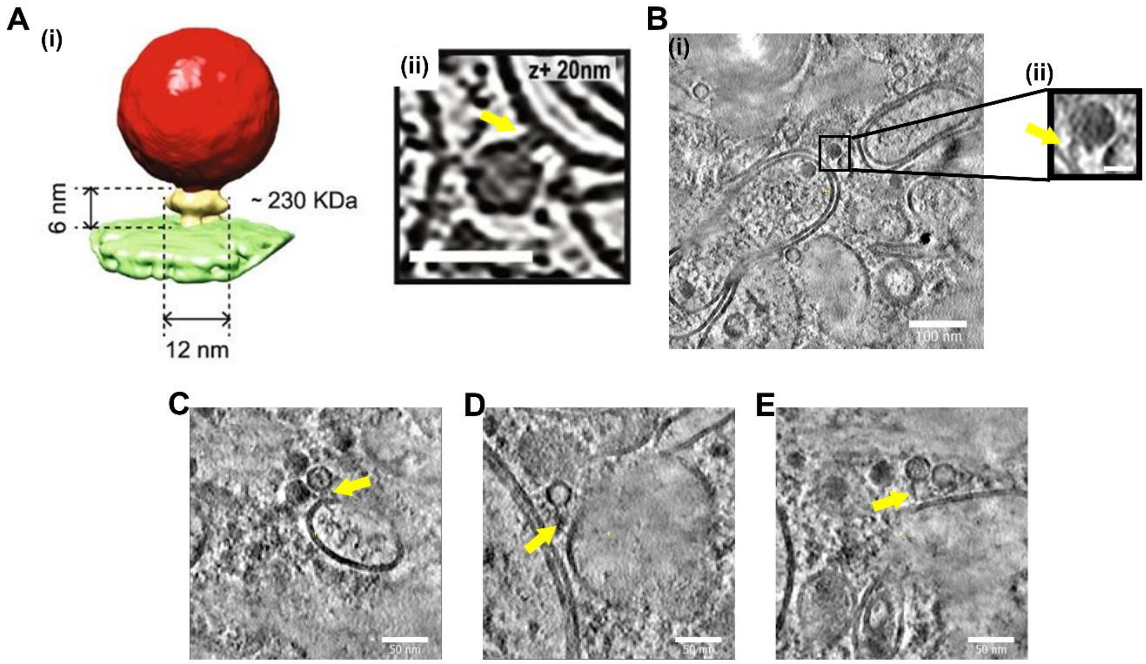

Figure 5.15 Examples of tether in poliovirus and ERAV.

(A) Tether between poliovirus and membrane. **(i)** STA of tethered poliovirus capsid with length and width of tether marked. The length of tether is 6nm between the virus capsid and the membrane. **(ii)** A tomogram slice through poliovirus with tether (yellow arrow). **(B)** Example of tether in ERAV infected Vero cell at 11hpi. **(i)** Tomogram slice through an ERAV infected Vero cell. **(ii)** Magnified view of an ERAV particle that is tethered (yellow arrow) to membrane. **(C-E)** Tomogram slices of ERAV infected Vero at 11hpi. These are examples of virus particles tethered to membranes. (Scale bar **A(ii)** = 50nm, **B(i)** = 100nm and **B(ii) and C-E** = 20nm) Panels **A (i)** and **(ii)** adapted from Dahmane et al., 2022.

ERAV particles tethered to membranes was observed in our tomograms, where the tethers were of variable length. Contrarily, tethers in enteroviruses seemed to be less heterogenic, in fact, in their reconstruction of tethered capsids, the tether was shown to be 6nm in length and 12nm wide (Figure 5.15A, Dahmane et al., 2022). This is unlike the tethers we observed for the ERAV particles (Figure 5.15B-E). ERAV tethers appeared to vary in lengths and potentially in width, hence making it difficult to be averaged and reconstructed as we have a limited data set. We have seen some tethers that maybe like the ones observed for enteroviruses. Could it suggest that the tethers observed are different structures, or different types of tethers? Could some of these tethers we see in ERAV be their genome? The long umbilical tethers are potentially a genome which is captured when RNA was being packaged into a capsid, hence tethering the capsid to the membrane. Whilst shorter tethers could be proteinaceous material, when the virus particles are in close contact with the membrane. In summary, it brings up two possibilities: (i) RNA packaging was captured hence longer tethers were seen connecting the virus capsid to the membrane (ii) the short tethers, that are potentially proteinaceous, were capsid intermediates suggesting that ERAV virions were assembling on RO, which is similar to enteroviruses. To further investigate the tethers, we should stall the replication cycle and use timepoints in a smaller range looking for capsid intermediates. This data may contribute to understanding the details of aphthovirus replication. Nevertheless, our data suggested that it is likely that ERAV utilises non-canonical autophagy in contrast to enteroviruses, facilitating viral replication.

We observed three classes of particles in our study, which were manually classified into full, partially full, and empty particles. Their quantity appeared to be different across the timepoints in our analysis. One hypothesis to explain the existence of the partially full particles is that following assembly of pentamers and genome, there is an intermediate stage or incomplete form where the viral genome is not yet fully packaged, representing this ‘partially full’ form. This partially full form appeared to be different from the intermediate capsid in enteroviruses (Dahmane *et al.*, 2022). Our partially full capsid appeared to be more fully assembled but with a tether, which is possibly the genome, that penetrates through the capsid. An alternative hypothesis is that since this is a late stage in replication that these were once fully assembled virions that have undergone aberrant partial uncoating and/or disassembly. A possible explanation is that they potentially have partially released the genome into neighbouring vesicles or to the cytoplasm as these particles are tethered to the membrane through a string-like structure, which we suspect is their genome. As in polioviruses, during cell entry virions experience a conformational change in the capsid losing the VP4 and exposing the N-terminus of VP1, ultimately leading to release of the genome (Fricks and Hogle, 1990; Belnap et al., 2000; Tuthill et al., 2010; Shah et al., 2020). Naturally occurring empty capsids can be produced in FMDV infected cells, but such empties often contain uncleaved VP0, suggesting they are particles which have not packaged RNA**.** We reconstructed an empty ERAV model at 11.5Å from the empty capsids imaged by cryo-ET. This model fitted very closely with the existing X-ray crystal structure of ERAV suggesting that the empty particles were was the same size as the mature virus and was a true representation of ERAV. The status of VP0 could not be resolved. Whilst the mechanism of genome release is not well studied for aphthoviruses. Otherwise, the reason for the accumulation of empty capsid remains unknown but it could likely be that the number of pentamers in the cells exceed the amount of viral genome present after peak replication timepoint, thus resulting in more empty particles being produced. Alternatively, the last possible explanation mentioned earlier, is that full virions were secreted earlier during replication and hence more empties were observed in late stages. Nevertheless, we observed an increase in empty particles over ERAV time course. Partially full particles were seen at timepoints except the peak replication time point 9hpi. We proposed a potential model to explain the accumulation of empty particles over time however this requires further investigation in the future.

Additional densities inside ERAV empty capsid were observed and is potentially an RNA binding site. For genome packaging to take place, the viral genome contains a specific region to initiate the process. This process is highly specific and involves structures within the viral genome, known as the packaging signals, to produce infectious virions (Stockley *et al.*, 2013; Shakeel *et al.*, 2017; Logan *et al.*, 2018; Ward *et al.*, 2022). The packaging signals interact with capsid proteins causing a conformational change and lead to the formation of an RNA-capsid protein conformer, which leads to a more efficient assembly of virions (Stockley *et al.*, 2013). Picornaviruses in the *parechovirus* genus have capsids composed of only three subunits: VP0, VP1 and VP3, there is no maturation cleavage. The interaction between capsid and packaging signals have been well established in parechoviruses. For example, it has been reported that encapsidation of Ljungan virus is associated with VP3 and packaging signals through electrostatic interactions (Zhu *et al.*, 2015). Whilst VP1 and VP3 in human parechovirus 1 (HPeV-1) capsids interact with the RNA genome and that the binding sites were found conserved across parechoviruses (Kalynych, Pálková and Plevka, 2016; Shakeel *et al.*, 2017). Therefore, have addressed that the viral RNA genome plays a key role in this specific process. We observed additional densities inside the capsid in the reconstruction of empty ERAV, however these densities were not observed in ERAV virions. Therefore, we are proposing a hypothesis that the empty lumps in empty ERAV capsids represents a conformation of an assembly competent pentamer. During virion assembly, these empty lumps would contact the vRNA packaging signals aiding particle assembly. Following maturation cleavage of VP0, resulting in a conformational change, these lumps would be absent in the mature virion. These densities have not previously been observed in aphthoviruses. If genome was once inside these empty particles and released due to an unknown mechanism, then VP0 would be cleaved into VP2 and VP4. Else, the VP0 precursor should have remained, instead of VP2 and VP4, or perhaps conformation changes in the capsid structure should be observed.

5.6. Summary

In summary, selective engulfment and the abundance of SMVs observed in our data suggested that the autophagy pathway involved in ERAV infection is highly likely to lean towards the non-canonical pathway. We identified, for the first time, an intracellular 3D model of ERAV full and empty particles and confirmed that this was closely similar to the X-ray crystal structure of purified ERAV. From our reconstructions of empty ERAV, we observed additional density on the inside surface of capsids, which may represent a novel packaging competent conformation of the capsid. The analysis of the partially full particles and the quantification of different classes of particles over the course of replication requires more data and further investigation.

Chapter 6 : Final discussion and future work

6.1. Discussion

The details of viral replication are crucial to understanding the virus life cycle. In +strand RNA viruses, rearrangement of host cell membrane is a common feature observed to facilitate virus replication. These rearranged membranes ultimately form a site that allow efficient replication and production of infectious virions. Such platforms for virus genome replication are known as the RO. The association between virus proteins, RO and the biogenesis of RO is better understood in enteroviruses than aphthoviruses and the aim of this study was to begin to address this imbalance by investigating the connection between aphthovirus induced membrane rearrangement, the site of genome replication and assembly of virus particles in infected cells using microscopy.

We generated a range of recombinant FMDV where tags that can be visualised using microscopy were inserted into 3A. These tags include short epitope HA and FLAG tags, tetracysteine and metallothionein tags that can be directly visualised in EM and GFP11, which is part of the split-GFP system. These recombinant viruses were proven to be functional and no change in the sequences was observed throughout passages of viruses. HA and FLAG tags were reported to be successfully used in a FMDV replicon study (Herod *et al.*, 2015). Tetracysteine and metallothionein 3A-tagged viruses were not carried forward as various issues including usage of metallothionein could lead to the build-up of toxicity in cells and the tetracysteine tags, although functional, do not have the most direct protocol for them to be used in both LM and EM. We took forward the split-GFP system to study the localisation of 3A proteins in FMDV infected cells. Such systems have previously been used in enterovirus studies in live cells (Schaar *et al.*, 2016a) and have been used to study enterovirus replication and the formation of RO in cells (Schaar *et al.*, 2016a). To summarise, we generated and characterised the first FMDV engineered with a tagged-3A protein to allow fluorescent signal for localisation of viral replication in live cells and in CLEM.

Taking forward the split-GFP system in this study, we investigated the use of membrane tracker to study the remodelling of host cell membranes upon infection. Both ER and Golgi membranes have been shown in different viruses to play a role in formation of RO as described and discussed in Chapter 1.6. Our ER tracker protocol was not fully optimised hence the potential link between ER membranes and site of replication was not observed. Another possibility for this is that the ER membrane had dispersed and remodelled into RO, and this was not captured in our data. Although ER membrane tracker was not followed up in our project as connection between ER membranes and 3A was not observed, this could still be further investigated as ER has been reported to be remodelled during FMDV replication resulting in the formation of vesicles (Lee *et al.*, 2022). Interestingly, these were reported to be vesicles different from COPII vesicles (Midgley *et al.*, 2013) or autophagosomes (Lee *et al.*, 2022) in FMDV infected cells. ER is still a potential source for the formation of RO and is directly involved in the lipid droplet storage and trafficking network (Prinz, 2010; Henne, 2019). In other +RNA viruses such as flaviviruses ER has been reported as involved in the massive remodelling to form RO and play a key role in the rearrangement of membranes (Gillespie *et al.*, 2010; Cortese *et al.*, 2017). For example, in the case of Zika virus, ER remodelled into clusters of vesicles and convoluted membranes, presumably where the site of viral RNA replication take place, and zippered ER, which makes this a unique feature of Zika virus RO in the *Flavivirus* family (Cortese *et al.*, 2017), although they could be found in a coronavirus, infectious bronchitis virus (IBV) (Maier *et al.*, 2013). Other +strand RNA virus examples including coronavirus (Knoops *et al.*, 2008) and HCV (Romero-Brey *et al.*, 2012) have demonstrated the link between ER and formation of RO. In picornaviruses, ROs were in separate compartments, hence it is more difficult to trace the origins of the membranes. Nevertheless, ER and Golgi membranes was shown to contribute to the formation of RO in enterovirus coxsackie B virus (CVB3) (Melia *et al.*, 2019). Collectively, this highlights the importance of investigating the role of ER in aphthovirus induced membrane remodelling in the future. The Golgi membrane tracker remains an interesting tool to discover whether they serve as an additional source of membrane to form ROs. In summary, Golgi tracker was non-specific and requires further optimisation and investigation. However, the use of this lipid reactive fluorescent dye is a volte-face from our expectation about dispersal of Golgi membranes, and thus is a potential CLEM signal for sites of replication.

We also mentioned the potential of lipid droplets (LDs) playing a key role in replication. More details of how picornaviruses utilise or alter lipid metabolism to support replication have been elucidated in the last few years. For example, it was shown that polioviruses recruit lipid droplets to replication organelles (Laufman, Perrino and Andino, 2019), while lipids play a key role in enterovirus A71 (EV-A71) replication through supplying energy to support viral protein synthesis (Yang *et al.*, 2022). CVB3 has also reported the recruitment of LDs to RO supporting its proliferation (Melia *et al.*, 2019). There are also other +strand RNA viruses that have reported an important role in replication for the lipid droplets. In fact, for HCV LDs have a crucial role in viral replication, LDs are not just recruited to the replication complexes, they also play a key role in virus assembly (Miyanari *et al.*, 2007; Shavinskaya *et al.*, 2007). The non-specific Golgi tracker used in this study was potentially staining LDs or other lipids in cells. These signals were seen adjacent to the replication foci, suggesting that LDs could potentially be recruited to the ROs supporting viral replication. Moreover, we have seen an example in cryo-ET data for ERAV where LDs were surrounded by virus particles and some tethered particles were seen (Chapter 8 Appendix Figure 7.3). However, due to the limited data size, it is insufficient to make a conclusion at this stage. Nonetheless, this sheds light on future work to investigate the role of LDs in aphthovirus replication. The understanding between LDs and viruses further enhances our knowledge of the differences between enterovirus replication and aphthovirus replication.

We compared FMDV and ERAV replication details using conventional EM. We first infected hamster cells using WT viruses and confirmed that we saw similar ultrastructural features compared to another study (Monaghan *et al.*, 2004), thus confirming that SMVs, DMVs, polysomes and ribosomes clusters are features indicating FMDV infection. We then wanted to compare ERAV and FMDV infected cells to confirm that both FMDV and ERAV induce similar features in infected cells. Both SMVs and DMVs were seen in FMDV and ERAV infected Vero cells although minor differences were observed, for example, the presence of polysomes and ribosomes, and the condensed replication site were not as obvious in ERAV infected Vero cells compared to FMDV infected Vero cells. Interestingly, an unknown structure, the membranous web (described in Chapter 4.2.1) was seen in ERAV infected Vero but not FMDV infected Vero cells. This structure was potentially derived from ER and, the analysis of this structure and its potential link to ERAV is due for future work. Vero cells are not a natural host for FMDV, so even though we have seen similar features in FMDV infected BHK and FMDV infected Vero cells, our hallmark of infection remains SMVs and DMVs.

Both FMDV and ERAV are highly pH sensitive (Curry *et al.*, 1995; Berryman *et al.*, 2005; Tuthill *et al.*, 2009; Groppelli, Tuthill and Rowlands, 2010; Caridi *et al.*, 2016), thus any conventional fixatives such as PFA and GA would dissociate the capsids, hence virus particles were not seen in EM through conventional fixation methods, justifying the use of ERAV as an FMDV surrogate in our cryo-ET study. A goal for future work would be analysing FMDV samples in cryo-EM. However, this requires the fulfilment of biosecurity requirements, which means samples must be fixed so viruses are inactivated. Unpublished data in our lab has shown that intact capsids can be fixed at low percentage PFA, and this was visualised in LM, even though a higher percentage, which was standard 4% PFA used for biosecurity requirement, was used after the initial low-fixation step. Therefore, a double fixation protocol was developed helping to cross-link intact capsids. This then subsequently allowed us to visualise intact capsids in conventional EM without the need to use heavy metals such as metallothionein and gold. In addition, samples could then be prepared on cryo-EM grids, and we could analyse FMDV-infected cells. An osmolarity mismatch between cells and fixatives and low pH in fixatives found to affect the preservation of intact capsid and the ultrastructure of cells. Hence, if this were resolved, it would be very useful in the development of a CLEM system. This would enable us to localise viral proteins in cells in LM and localise assembled capsids and RO in EM. Thus, the information gap of the connection between sites of replication, RO and site of capsid assembly would be filled in.

We showed that single membrane vesicles are abundant in infected cells in Chapter 4 and 5. The lack of DMVs could be due to aphthoviruses inducing a non-canonical autophagy pathway that predominantly utilises single membrane vesicles instead of DMV. Moreover, we preliminarily analysed the virus particles that are tethered to membrane structures. We have seen a small number of full particles appearing within the DMVs, potentially engulfed by the autophagosome. The exact mechanism or trigger of this engulfment will be further investigated. Most particles are tethered to the vesicles through a connector that is likely to be the viral genome but yet to be confirmed. Our analysis showed that empty particles are more likely to appear closer to the membranes. This can be further characterised and analysed in the future when more data is available. Ultimately, there needs to be a more standardised system of segregating and quantifying the particles classes, such as full and empty particles and their associated membrane structures or improving on the definition of close contact between a virus particle and the membrane. We observed an accumulation of empty particles over time, which we hypothesised may be because full ERAV particles might have been secreted earlier. This would then show a similar feature between enterovirus replication and aphthovirus replication, as it has recently been suggested that enteroviruses undergo a selection by autophagic membranes and that only RNA-loaded (full) virions are secreted (Dahmane *et al.*, 2022). Lastly, we identified potential contact sites between the RNA packaging signal and the capsid in our empty ERAV reconstruction. RNA contact sites in the capsid were previously reported in Ljungan viruses (Zhu *et al.*, 2015) and HPeV-1 (Kalynych, Pálková and Plevka, 2016), this is potentially the first hint of a similar structure in aphthoviruses.

6.2. Future work

Recombinant FMDV containing short epitope tags has been used in our lab for coinfection studies. Recombinant viruses containing a tetracysteine tag and a metallothionein tag requires further optimisation, but both are potentially useful tools to directly visualise and localise 3A proteins in EM. Further optimisation of split GFP system could be performed to improve the transfection efficiency.

ER membrane tracker protocols have been refined in this study but required further optimisation in the future. Golgi membrane tracker needs further optimisation to segregate LDs and Golgi membranes. This could potentially be resolved by using a marker for LD and comparing by correlating signals of LDs and Golgi membranes during FMDV replication. Moreover, to investigate the connection between LD and FMDV replication, FMDV 2C could be used as the replication marker instead of 3A. If this is similar to polioviruses', then the LD is recruited to the RO by 2C (Laufman, Perrino and Andino, 2019), we would then expect 2C and LD signals to appear in close proximity. Both ER membrane tracker and Golgi membrane tracker led to live-cell imaging to record the dispersal or remodelling of membranes. Information could then be correlated with EM data to further develop a CLEM system for aphthovirus study.

Secondly, more conventional TEM data for both FMDV- and ERAV-infected cells, including time course, should be collected. In addition to that, high pressure freezing of FMDV infected and ERAV infected cells. These two approaches would provide more details of the rearrangement of membranes, thus providing details to compare the differences between FMDV and ERAV replication. Secondly, we should aim to export samples out of high containment which allows us to collect cryo-ET data on FMDV-infected cells. Objectives would be first to investigate UV inactivation of samples. This would then eliminate technical issues encountered in the double-fixation protocol. However, while that is in development, further improvement of the double fixation protocol should not be left aside. This should be further optimised with the aim (i) to visualise FMDV and ERAV capsids in conventional EM (ii) to resolve the osmolarity issue during EM sample preparation to better preserve ultrastructure of cells.

More cryo-ET data are required to generate a higher resolution ERAV STA model and to better understand the link between virus particles and tethered membrane structures. Also, collecting data in a shorter timeframe could be used to study processing such as assembly of virus particles, potentially enabling us to capture any intermediate form of capsid during the assembly process. The use of drugs to inhibit parts of the virus life cycle can elucidate information in regard to virus particles and tethered membranes. For example, guanidine hydrochloride can inhibit replication of aphthoviruses (Pringle, 1964; Nettleton, Davies and Rweyemamu, 1982; Saunders and King, 1982; Klein *et al.*, 2000) which allows us to observe an accumulation of empty particles over time. We can also use drugs to inhibit autophagy with the aim to observe accumulation of ERAV virions overtime. This would ultimately reveal more detail in how autophagy plays its role in replication. In addition to that, the infectious particles secreted should be measured by plaque assay, as we have only measured the total titre of virus, hence this piece of information is still missing in our study. A higher resolution STA model allows us to do a more detailed structural analysis between two full classes of ERAV particles and empty ERAV particles. This would enable us to further investigate the empty densities identified and the connection between RNA and capsid.

Ultimately, the goal is to study FMDV infected cells using cryo-EM. Therefore, investigation in the use of cross-linkers and further optimisation of fixatives would aid visualisation of intact FMDV capsids in conventional fixed EM samples. This would benefit us in developing a CLEM system and elucidate information of replication foci and capsid assembly foci. Since an infectious clone exists for FMDV this provides more opportunities for study than ERAV for which an infectious clone still has not been developed. By analysing FMDV-infected cells in cryo-EM, we could then reconstruct an *in-situ* 3D model of FMDV and analyse the connection between virus particles and RO. Furthermore, we could also analyse these samples in cryo-SXT, this enables us to compare a whole FMDV infected cell and ERAV infected cell. Reconstruction from cryo-SXT would then enable us to reconstruct the ultrastructural changes of aphthovirus infected cells. The comparison analysis is not limited to comparing FMDV and ERAV infected cells but would also enable us to compare aphthovirus replication to other picornaviruses.

6.3. Conclusion

In summary, recombinant FMDVs were generated with the aim of facilitating the development of a CLEM system for an FMDV replication study. The split GFP system was employed in this study using our recombinant FMDV containing two copies of GFP11. This has revealed that sites of replication appear contiguous to the Golgi membranes and potentially lipid droplets, which requires further investigation. ER remains as a potential source for the formation of replication organelles but requires further investigation as we did not observe any specific links between the site of replication and ER membrane signals.

We identified ROs, both SMVs and DMVs, in FMDV and ERAV infected cells. These vesicles appeared in small clusters and the number of vesicles seen were not abundant. In our cryo-ET data, we observed a similar trend where vesicles, or virus induced remodelled membrane structures appeared in clusters. The predominant feature in ERAV infected cells appeared to be SMVs, with a small number of DMVs observed. This suggested to us that aphthoviruses potentially employs the non-canonical autophagy pathway, hence less DMVs were seen. Most virus particles seen in our tomograms were found tethered to a membrane structure. The tethers were of different lengths, but empty particles appeared to be slightly closer to membranes compared to full particles. The exact reason remains unknown, also, more data is required to further confirm this and further analyse the structure and identity of the tether, i.e. whether or not these tethers are genome? This is the first time, an in situ ERAV STA model is presented. We reconstructed two classes of ERAV virions and an ERAV empty particle. A novel finding was the empty densities (empty lumps) observed in our STA model. This could potentially be revealing an RNA contact site in the capsid of aphthoviruses. Lastly, our project has set out a complete pipeline on an *in vitro* study for aphthovirus replication. This includes a CLEM system to be further developed and optimised, from cryo-EM sample preparation to data processing. This will contribute to future projects in revealing more details of aphthovirus replication and ultimately enable us to compare replication details between aphthoviruses and other picornaviruses.

Chapter 7 Bibliography

Abernathy, E. *et al.* (2019) ‘Differential and convergent utilization of autophagy components by positive-strand RNA viruses’. Available at: https://doi.org/10.1371/journal.pbio.2006926.

Acharya, R. *et al.* (1989) ‘The three-dimensional structure of foot-and-mouth disease virus at 2.9 Å resolution’, *Nature 1989 337:6209*, 337(6209), pp. 709–716. Available at: https://doi.org/10.1038/337709a0.

Adeyemi, O.O. *et al.* (2021) ‘Functional advantages of triplication of the 3B coding region of the FMDV genome’, *The FASEB Journal*, 35(2), p. e21215. Available at: https://doi.org/10.1096/FJ.202001473RR.

Al-Amoudi, A. *et al.* (2004) ‘Cryo-electron microscopy of vitreous sections’, *The EMBO Journal*, 23(18), pp. 3583–3588. Available at: https://doi.org/10.1038/SJ.EMBOJ.7600366.

Al-Amoudi, A., Norlen, L.P.O. and Dubochet, J. (2004) ‘Cryo-electron microscopy of vitreous sections of native biological cells and tissues’, *Journal of Structural Biology*, 148(1), pp. 131–135. Available at: https://doi.org/10.1016/J.JSB.2004.03.010.

Al-Amoudi, A., Studer, D. and Dubochet, J. (2005) ‘Cutting artefacts and cutting process in vitreous sections for cryo-electron microscopy’, *Journal of Structural Biology*, 150(1), pp. 109–121. Available at: https://doi.org/10.1016/J.JSB.2005.01.003.

Aldabe, R., Irurzun, A. and Carrasco, L. (1997) ‘Poliovirus protein 2BC increases cytosolic free calcium concentrations’, *Journal of Virology*, 71(8), pp. 6214–6217. Available at: https://doi.org/10.1128/JVI.71.8.6214-6217.1997.

Ao, D. *et al.* (2015) ‘Viroporin Activity of the Foot-and-Mouth Disease Virus Non-Structural 2B Protein’, *PLOS ONE*, 10(5), p. e0125828. Available at: https://doi.org/10.1371/JOURNAL.PONE.0125828.

Avilov, S. v. *et al.* (2012) ‘Replication-Competent Influenza A Virus That Encodes a Split-Green Fluorescent Protein-Tagged PB2 Polymerase Subunit Allows Live-Cell Imaging of the Virus Life Cycle’, *Journal of Virology*, 86(3), pp. 1433–1448. Available at: https://doi.org/10.1128/JVI.05820-11/SUPPL_FILE/SUPPMOVIELEGENDS.DOC.

Bakrač, B. *et al.* (2010) ‘A toxin-based probe reveals cytoplasmic exposure of Golgi sphingomyelin’, *Journal of Biological Chemistry*, 285(29), pp. 22186–22195. Available at: https://doi.org/10.1074/jbc.M110.105122.

Beard, C.W. and Mason, P.W. (2000) ‘Genetic Determinants of Altered Virulence of Taiwanese Foot-and-Mouth Disease Virus’, *Journal of Virology*, 74(2), pp. 987–991. Available at: https://doi.org/10.1128/JVI.74.2.987-991.2000/ASSET/D8EC71E9-7B62-43BC-8630-DD37D914C1BB/ASSETS/GRAPHIC/JV0201026003.JPEG.

Belnap, D.M. *et al.* (2000) ‘Molecular Tectonic Model of Virus Structural Transitions: the Putative Cell Entry States of Poliovirus’, *Journal of Virology*, 74(3), pp. 1342–1354. Available at: https://doi.org/10.1128/JVI.74.3.1342-

1354.2000/ASSET/0CD90A11-8E10-48AB-8E06-B1F3BE4AFEA9/ASSETS/GRAPHIC/JV0301353007.JPEG.

Belov, G.A. *et al.* (2012) ‘Complex dynamic development of poliovirus membranous replication complexes.’, *Journal of virology*, 86(1), pp. 302–12. Available at: https://doi.org/10.1128/JVI.05937-11.

Belov, G.A. and Sztul, E. (2014) ‘Rewiring of Cellular Membrane Homeostasis by Picornaviruses’, *Journal of Virology*, 88(17), pp. 9478–9489. Available at: https://doi.org/10.1128/JVI.00922-14.

Belsham, G.J. (2015) ‘Translation and replication of FMDV RNA Translation and Replication of FMDV RNA’, *Current topics in microbiology and immunology*, 288(July), pp. 43–70. Available at: https://doi.org/10.1007/3-540-27109-0.

Belsham, G.J. (2020) ‘Towards improvements in foot-and-mouth disease vaccine performance’, *Acta Veterinaria Scandinavica*, 62(1), p. 20. Available at: https://doi.org/10.1186/S13028-020-00519-1.

Belsham, G.J., McInerney, G.M. and Ross-Smith, N. (2000) ‘Foot-and-Mouth Disease Virus 3C Protease Induces Cleavage of Translation Initiation Factors eIF4A and eIF4G within Infected Cells’, *Journal of Virology*, 74(1), p. 272. Available at: https://doi.org/10.1128/JVI.74.1.272-280.2000.

Berryman, S. *et al.* (2005) ‘Early Events in Integrin αvβ6-Mediated Cell Entry of Foot-and-Mouth Disease Virus’, *Journal of Virology*, 79(13), pp. 8519–8534. Available at: https://doi.org/10.1128/jvi.79.13.8519-8534.2005.

Berryman, S. *et al.* (2012) ‘Foot-and-Mouth Disease Virus Induces Autophagosomes during Cell Entry via a Class III Phosphatidylinositol 3-Kinase-Independent Pathway’, *Journal of Virology*, 86(23), pp. 12940–12953. Available at: https://doi.org/10.1128/JVI.00846-12.

Berryman, S. *et al.* (2016) ‘Foot-and-mouth disease virus replicates independently of phosphatidylinositol 4-phosphate and type III phosphatidylinositol 4-kinases.’, *The Journal of general virology*, 97(8), pp. 1841–52. Available at: https://doi.org/10.1099/jgv.0.000485.

Bouchet-Marquis, C. *et al.* (2012) ‘Metallothionein as a clonable high-density marker for cryo-electron microscopy’, *Journal of Structural Biology*, 177(1), pp. 119–127. Available at: https://doi.org/10.1016/j.jsb.2011.10.007.

Brooksby, J.B. (1982) ‘Portraits of Viruses: Foot-and-Mouth Disease Virus’, *Intervirology*, 18(1–2), pp. 1–23. Available at: https://doi.org/10.1159/000149299.

Brown, F. *et al.* (1974) ‘Poly(C) in animal viral RNAs’, *Nature 1974 251:5473*, 251(5473), pp. 342–344. Available at: https://doi.org/10.1038/251342a0.

Burman, A. *et al.* (2006) ‘Specificity of the VP1 GH Loop of Foot-and-Mouth Disease Virus for αv Integrins’, *Journal of Virology*, 80(19), p. 9798. Available at: https://doi.org/10.1128/JVI.00577-06.

Büttner, C.R. *et al.* (2022) ‘Cryo-electron microscopy and image classification reveal the existence and structure of the coxsackievirus A6 virion’, *Communications Biology 2022 5:1*, 5(1), pp. 1–10. Available at: https://doi.org/10.1038/s42003-022-03863-2.

Campanella, M. *et al.* (2004) ‘The Coxsackievirus 2B Protein Suppresses Apoptotic Host Cell Responses by Manipulating Intracellular Ca2+ Homeostasis’, *Journal of Biological Chemistry*, 279(18), pp. 18440–18450. Available at: https://doi.org/10.1074/jbc.M309494200.

Caridi, F. *et al.* (2016) ‘Equine Rhinitis A Virus Mutants with Altered Acid Resistance Unveil a Key Role of VP3 and Intrasubunit Interactions in the Control of the pH Stability of the Aphthovirus Capsid’, *Journal of Virology*, 90(21), pp. 9725–9732. Available at: https://doi.org/10.1128/jvi.01043-16.

Caspar, D.L. and Klug, A. (1962) ‘Physical Principles in the Construction of Regular Viruses’, *Cold Spring Harbor Symposia on Quantitative Biology*, 27, pp. 1–24. Available at: https://doi.org/10.1101/SQB.1962.027.001.005.

Chen, L. *et al.* (2014) ‘Heavy Metal-induced Metallothionein Expression Is Regulated by Specific Protein Phosphatase 2A Complexes’, *The Journal of Biological Chemistry*, 289(32), p. 22413. Available at: https://doi.org/10.1074/JBC.M114.548677.

Chen, M. *et al.* (2017) ‘Convolutional neural networks for automated annotation of cellular cryo-electron tomograms’, *Nature Methods 2017 14:10*, 14(10), pp. 983–985. Available at: https://doi.org/10.1038/nmeth.4405.

Childs, K. *et al.* (2021) ‘Demonstration of co-infection and trans-encapsidation of viral RNA in vitro using epitope-tagged foot-and-mouth disease viruses’, *Viruses*, 13(12). Available at: https://doi.org/10.3390/v13122433.

Chow, M. *et al.* (1987) ‘Myristylation of picornavirus capsid protein VP4 and its structural significance’, *Nature 1987 327:6122*, 327(6122), pp. 482–486. Available at: https://doi.org/10.1038/327482a0.

Clarke, B.E. *et al.* (1987) ‘Potential secondary and tertiary structure in the genomic RNA of foot and mouth disease virus’, *Nucleic Acids Research*, 15(17), pp. 7067–7079. Available at: https://doi.org/10.1093/NAR/15.17.7067.

Cortese, M. *et al.* (2017) ‘Ultrastructural Characterization of Zika Virus Replication Factories’, *Cell Reports*, 18(9), pp. 2113–2123. Available at: https://doi.org/10.1016/J.CELREP.2017.02.014.

Curry, S. *et al.* (1995) ‘Viral RNA modulates the acid sensitivity of foot-and-mouth disease virus capsids’, *Journal of Virology*, 69(1), pp. 430–438. Available at: https://doi.org/10.1128/JVI.69.1.430-438.1995.

Curry, S. *et al.* (1997) ‘Dissecting the roles of VP0 cleavage and RNA packaging in picornavirus capsid stabilization: the structure of empty capsids of foot-and-mouth disease virus.’, *Journal of Virology*, 71(12).

Dahmane, S. *et al.* (2022) ‘Membrane-assisted assembly and selective secretory autophagy of enteroviruses’, *Nature Communications 2022 13:1*, 13(1), pp. 1–14. Available at: https://doi.org/10.1038/s41467-022-33483-7.

Danev, R., Yanagisawa, H. and Kikkawa, M. (2019) ‘Cryo-Electron Microscopy Methodology: Current Aspects and Future Directions’, *Trends in Biochemical Sciences*, 44(10), pp. 837–848. Available at: https://doi.org/10.1016/J.TIBS.2019.04.008.

Devaney,’, M.A. *et al.* (1988) ‘Leader protein of foot-and-mouth disease virus is required for cleavage of the p220 component of the cap-binding protein complex’, *Journal of Virology*, 62(11), pp. 4407–4409. Available at: https://doi.org/10.1128/JVI.62.11.4407-4409.1988.

DiCara, D. *et al.* (2008) ‘Foot-and-Mouth Disease Virus Forms a Highly Stable, EDTA-Resistant Complex with Its Principal Receptor, Integrin αvβ6: Implications for Infectiousness’, *Journal of Virology*, 82(3), pp. 1537–1546. Available at: https://doi.org/10.1128/JVI.01480-07/ASSET/45D323EA-CC8E-40C6-A8F3-B87CF67651C4/ASSETS/GRAPHIC/ZJV0030802040008.JPEG.

De Diego, M. *et al.* (1997) ‘The non-structural polyprotein 3ABC of foot-and-mouth disease virus as a diagnostic antigen in ELISA to differentiate infected from vaccinated cattle’, *Archives of Virology*, 142(10), pp. 2021–2033. Available at: https://doi.org/10.1007/S007050050219/METRICS.

Diestra, E. *et al.* (2009) ‘Visualization of proteins in intact cells with a clonable tag for electron microscopy’, *Journal of Structural Biology*, 165(3), pp. 157–168. Available at: https://doi.org/10.1016/J.JSB.2008.11.009.

Doerflinger, S.Y. *et al.* (2017) ‘Membrane alterations induced by nonstructural proteins of human norovirus’, *PLOS Pathogens*, 13(10), p. e1006705. Available at: https://doi.org/10.1371/JOURNAL.PPAT.1006705.

Donnelly, M.L.L., Luke, G., *et al.* (2001) ‘Analysis of the aphthovirus 2A/2B polyprotein “cleavage” mechanism indicates not a proteolytic reaction, but a novel translational effect: A putative ribosomal “skip”’, *Journal of General Virology*, 82(5), pp. 1013–1025. Available at: https://doi.org/10.1099/0022-1317-82-5-1013/CITE/REFWORKS.

Donnelly, M.L.L., Hughes, L.E., *et al.* (2001) ‘The “cleavage” activities of foot-and-mouth disease virus 2A site-directed mutants and naturally occurring “2A-like” sequences’, *Journal of General Virology*, 82(5), pp. 1027–1041. Available at: https://doi.org/10.1099/0022-1317-82-5-1027/CITE/REFWORKS.

Doyle, N. *et al.* (2021) ‘Coronavirus RNA Synthesis Takes Place within Membrane-Bound Sites’, *Viruses*, 13(12). Available at: https://doi.org/10.3390/V13122540/S1.

Ellisman, M.H. *et al.* (2012) ‘Picking Faces out of a Crowd: Genetic Labels for Identification of Proteins in Correlated Light and Electron Microscopy Imaging’, *Methods in Cell Biology*, 111, pp. 139–155. Available at: https://doi.org/10.1016/B978-0-12-416026-2.00008-X.

Erickson, H.P. and Klug, A. (1970) ‘The Fourier Transform of an Electron Micrograph: Effects of Defocussing and Aberrations, and Implications for the Use of Underfocus Contrast Enhancement’, *Berichte der Bunsengesellschaft für* *physikalische Chemie*, 74(11), pp. 1129–1137. Available at: https://doi.org/10.1002/BBPC.19700741109.

Erickson, H.P. and Klug, A. (1971) ‘Measurement and compensation of defocusing and aberrations by Fourier processing of electron micrographs’, *Philosophical Transactions of the Royal Society of London. B, Biological Sciences*, 261(837), pp. 105–118. Available at: https://doi.org/10.1098/RSTB.1971.0040.

EXPASY (2023) *Icosahedric capsids, Caspar and Klug ~ ViralZone*. Available at: https://viralzone.expasy.org/8577 (Accessed: 19 April 2023).

Ferrer-Orta, C. *et al.* (2004) ‘Structure of foot-and-mouth disease virus RNA-dependent RNA polymerase and its complex with a template-primer RNA’, *Journal of Biological Chemistry*, 279(45), pp. 47212–47221. Available at: https://doi.org/10.1074/jbc.M405465200.

Ferrer-Orta, C. *et al.* (2006) ‘The structure of a protein primer–polymerase complex in the initiation of genome replication’, *The EMBO Journal*, 25(4), pp. 880–888. Available at: https://doi.org/10.1038/SJ.EMBOJ.7600971.

Foot and mouth disease - WOAH - World Organisation for Animal Health (no date). Available at: https://www.woah.org/en/disease/foot-and-mouth-disease/#ui-id-2 (Accessed: 5 April 2023).

Forss, S. and Schaller, H. (1982) ‘A tandem repeat gene in a picornavirus.’, *Nucleic Acids Research*, 10(20), p. 6441. Available at: https://doi.org/10.1093/NAR/10.20.6441.

Fricks1, C.E. and Hogle2, J.M. (1990) ‘Cell-induced conformational change in poliovirus: externalization of the amino terminus of VP1 is responsible for liposome binding’, *Journal of Virology*, 64(5), pp. 1934–1945. Available at: https://doi.org/10.1128/JVI.64.5.1934-1945.1990.

Fu, S. zu *et al.* (2019) ‘DDX56 cooperates with FMDV 3A to enhance FMDV replication by inhibiting the phosphorylation of IRF3’, *Cellular Signalling*, 64. Available at: https://doi.org/10.1016/J.CELLSIG.2019.109393.

Gamarnik, A. V. and Andino, R. (1998) ‘Switch from translation to RNA replication in a positive-stranded RNA virus’, *Genes & Development*, 12(15), p. 2293. Available at: https://doi.org/10.1101/GAD.12.15.2293.

Gao, Y., Sun, S.-Q. and Guo, H.-C. (2016) ‘Biological function of Foot-and-mouth disease virus non-structural proteins and non-coding elements.’, *Virology journal*, 13, p. 107. Available at: https://doi.org/10.1186/s12985-016-0561-z.

García-Briones, M. *et al.* (2006) ‘Differential distribution of non-structural proteins of foot-and-mouth disease virus in BHK-21 cells’, *Virology*, 349(2), pp. 409–421. Available at: https://doi.org/10.1016/J.VIROL.2006.02.042.

Gazina, E. V. *et al.* (2002) ‘ Differential Requirements for COPI Coats in Formation of Replication Complexes among Three Genera of Picornaviridae ’, *Journal of Virology*, 76(21), pp. 11113–11122. Available at: https://doi.org/10.1128/JVI.76.21.11113-11122.2002/ASSET/4256E3B7-2F32-47EE-BB65-DCFFDC027AE5/ASSETS/GRAPHIC/JV2120327007.JPEG.

Gazina, E. v *et al.* (2002) ‘Differential Requirements for COPI Coats in Formation of Replication Complexes among Three Genera of Picornaviridae’, *JOURNAL OF VIROLOGY*, 76(21), pp. 11113–11122. Available at: https://doi.org/10.1128/JVI.76.21.11113-11122.2002.

Ghadially, F.N. (1988) ‘Mitochondria’, *Ultrastructural Pathology of the Cell and Matrix*, pp. 191–328. Available at: https://doi.org/10.1016/B978-0-407-01571-5.50010-0.

Gillespie, L.K. *et al.* (2010) ‘The Endoplasmic Reticulum Provides the Membrane Platform for Biogenesis of the Flavivirus Replication Complex’, *Journal of Virology*, 84(20), pp. 10438–10447. Available at: https://doi.org/10.1128/JVI.00986-10/SUPPL_FILE/SUPPL__FIG____MOVIE_LEGENDS.DOC.

Gladue, D.P. *et al.* (2012) ‘Foot-and-Mouth Disease Virus Nonstructural Protein 2C Interacts with Beclin1, Modulating Virus Replication’, *Journal of Virology*, 86(22), p. 12080. Available at: https://doi.org/10.1128/JVI.01610-12.

Gladue, D.P. *et al.* (2018) ‘Molecular Characterization of the Viroporin Function of Foot-and-Mouth Disease Virus Nonstructural Protein 2B’, *Journal of Virology*, 92(23), pp. 1360–1378. Available at: https://doi.org/10.1128/JVI.01360-18/ASSET/40EAD7D2-95A3-49FD-93C7-3867F25F56C6/ASSETS/GRAPHIC/ZJV0231840280009.JPEG.

Golde, W.T. *et al.* (2005) ‘Vaccination against foot-and-mouth disease virus confers complete clinical protection in 7 days and partial protection in 4 days: Use in emergency outbreak response', *Vaccine*, 23(50), pp. 5775–5782. Available at: https://doi.org/10.1016/j.vaccine.2005.07.043.

Goodfellow, I. *et al.* (2000) ' Identification of a cis -Acting Replication Element within the Poliovirus Coding Region ', *Journal of Virology*, 74(10), pp. 4590–4600. Available at: https://doi.org/10.1128/JVI.74.10.4590-4600.2000/ASSET/13D797B4-3899-43BE-B0A3-B9915A27E7CD/ASSETS/GRAPHIC/JV1001735005.JPEG.

Gorelick, S. *et al.* (2011) 'High-efficiency Fresnel zone plates for hard X-rays by 100 keV e-beam lithography and electroplating', *Journal of Synchrotron Radiation*, 18(Pt 3), p. 442. Available at: https://doi.org/10.1107/S0909049511002366.

Groppelli, E. *et al.* (2017) 'Picornavirus RNA is protected from cleavage by ribonuclease during virion uncoating and transfer across cellular and model membranes', *PLOS Pathogens*, 13(2), p. e1006197. Available at: https://doi.org/10.1371/JOURNAL.PPAT.1006197.

Groppelli, E., Tuthill, T.J. and Rowlands, D.J. (2010) 'Cell Entry of the Aphthovirus Equine Rhinitis A Virus Is Dependent on Endosome Acidification', *Journal of Virology*, 84(12), pp. 6235–6240. Available at: https://doi.org/10.1128/JVI.02375-09.

Grubman, M.J. and Baxt, B. (2004) 'Foot-and-Mouth Disease', *Clinical Microbiology Reviews*, 17(2), pp. 465–493. Available at: https://doi.org/10.1128/CMR.17.2.465-493.2004/ASSET/E282E55E-2BF2-49DD-9A19-5DC8A97AF952/ASSETS/GRAPHIC/ZCM0020400610004.JPEG.

Hackstadt, T. *et al.* (2021) ‘Disruption of the Golgi Apparatus and Contribution of the Endoplasmic Reticulum to the SARS-CoV-2 Replication Complex’, *Viruses*, 13(9). Available at: https://doi.org/10.3390/V13091798.

Hagen, W.J.H., Wan, W. and Briggs, J.A.G. (2017) ‘Implementation of a cryo-electron tomography tilt-scheme optimized for high resolution subtomogram averaging’, *Journal of Structural Biology*, 197(2), pp. 191–198. Available at: https://doi.org/10.1016/J.JSB.2016.06.007.

Han, S.C. *et al.* (2016) ‘Productive Entry of Foot-and-Mouth Disease Virus via Macropinocytosis Independent of Phosphatidylinositol 3-Kinase’, *Scientific Reports 2016 6:1*, 6(1), pp. 1–22. Available at: https://doi.org/10.1038/srep19294.

Han, S.C., Guo, H.C. and Sun, S.Q. (2015) ‘Three-dimensional structure of foot-and-mouth disease virus and its biological functions’, *Archives of Virology*, 160(1), pp. 1–16. Available at: https://doi.org/10.1007/S00705-014-2278-X/FIGURES/5.

Harkiolaki, M. *et al.* (2018) ‘Cryo-soft X-ray tomography: using soft X-rays to explore the ultrastructure of whole cells’, *Emerging Topics in Life Sciences*, 2(1), pp. 81–92. Available at: https://doi.org/10.1042/ETLS20170086.

Harmsen, M.M. *et al.* (2007) ‘Passive immunization of guinea pigs with llama single-domain antibody fragments against foot-and-mouth disease’, *Veterinary Microbiology*, 120(3–4), pp. 193–206. Available at: https://doi.org/10.1016/J.VETMIC.2006.10.029.

Harmsen, M.M. *et al.* (2011) 'Effect of thiomersal on dissociation of intact (146S) foot-and-mouth disease virions into 12S particles as assessed by novel ELISAs specific for either 146S or 12S particles', *Vaccine*, 29(15), pp. 2682–2690. Available at: https://doi.org/10.1016/J.VACCINE.2011.01.069.

Harris, K.S. *et al.* (1992) 'Purification and characterization of poliovirus polypeptide 3CD, a proteinase and a precursor for RNA polymerase', *Journal of Virology*, 66(12), pp. 7481–7489. Available at: https://doi.org/10.1128/JVI.66.12.7481-7489.1992.

Harris, T.J.R. and Brown, F. (1977) 'Biochemical analysis of a virulent and an avirulent strain of foot and mouth disease virus', *Journal of General Virology*, 34(1), pp. 87–105. Available at: https://doi.org/10.1099/0022-1317-34-1-87/CITE/REFWORKS.

Hayat, M.A. (1989) *Principles and Techniques of Electron Microscopy*. Third Edit.

Henne, M. (2019) 'And three's a party: lysosomes, lipid droplets, and the ER in lipid trafficking and cell homeostasis', *Current Opinion in Cell Biology*, 59, pp. 40–49. Available at: https://doi.org/10.1016/J.CEB.2019.02.011.

Herod, M.R. *et al.* (2015) 'Employing transposon mutagenesis to investigate foot-and-mouth disease virus replication', *Journal of General Virology*, 96(12), pp. 3507–3518. Available at: https://doi.org/10.1099/jgv.0.000306.

Hoffman, E.A. *et al.* (2015) ‘Formaldehyde Crosslinking: A Tool for the Study of Chromatin Complexes *’, *THE JOURNAL OF BIOLOGICAL CHEMISTRY*, 290(44), pp. 26404–26411. Available at: https://doi.org/10.1074/jbc.R115.651679.

Hong, H.Q. *et al.* (2018) ‘Bidirectional regulation of adenosine-to-inosine (A-to-I) RNA editing by DEAH box helicase 9 (DHX9) in cancer’, *Nucleic Acids Research*, 46(15), pp. 7953–7969. Available at: https://doi.org/10.1093/NAR/GKY396.

Hsu, N.Y. *et al.* (2010) ‘Viral reorganization of the secretory pathway generates distinct organelles for RNA replication’, *Cell*, 141(5), pp. 799–811. Available at: https://doi.org/10.1016/J.CELL.2010.03.050.

Jackson, T. *et al.* (1996) ‘Efficient infection of cells in culture by type O foot-and-mouth disease virus requires binding to cell surface heparan sulfate.’, *Journal of Virology*, 70(8), p. 5282. Available at: https://doi.org/10.1128/JVI.70.8.5282-5287.1996.

Jackson, T. and Belsham, G.J. (2021) ‘Picornaviruses: A View from 3A’. Available at: https://doi.org/10.3390/v13030456.

Jackson, V. (1978) ‘Studies on histone organization in the nucleosome using formaldehyde as a reversible cross-linking agent’, *Cell*, 15(3), pp. 945–954. Available at: https://doi.org/10.1016/0092-8674(78)90278-7.

Jackson, W.T. *et al.* (2005) ‘Subversion of Cellular Autophagosomal Machinery by RNA Viruses’, *PLOS Biology*, 3(5), p. e156. Available at: https://doi.org/10.1371/JOURNAL.PBIO.0030156.

Jamal, S.M. and Belsham, G.J. (2013) ‘Foot-and-mouth disease: Past, present and future’, *Veterinary Research*. BioMed Central, p. 116. Available at: https://doi.org/10.1186/1297-9716-44-116.

Johnson, T.J.A. (1985) ‘Aldehyde fixatives: Quantification of acid-producing reactions’, *Journal of Electron Microscopy Technique*, 2(2), pp. 129–138. Available at: https://doi.org/10.1002/JEMT.1060020204.

Juleff, N. *et al.* (2008) ‘Foot-and-Mouth Disease Virus Persists in the Light Zone of Germinal Centres’, *PLoS ONE*, 3(10), p. 3434. Available at: https://doi.org/10.1371/JOURNAL.PONE.0003434.

Kalynych, S., Pálková, L. and Plevka, P. (2016) ‘The Structure of Human Parechovirus 1 Reveals an Association of the RNA Genome with the Capsid’, *Journal of Virology*, 90(3), p. 1377. Available at: https://doi.org/10.1128/JVI.02346-15.

Kimanius, D. *et al.* (2021) ‘New tools for automated cryo-EM single-particle analysis in RELION-4.0’, *Biochemical Journal*, 478(24), pp. 4169–4185. Available at: https://doi.org/10.1042/BCJ20210708.

Kirkegaard, K. and Jackson, W.T. (2005) ‘Topology of Double-Membraned Vesicles and the Opportunity for Non-Lytic Release of Cytoplasm’, *http://dx.doi.org/10.4161/auto.1.3.2065*, 1(3), pp. 182–184. Available at: https://doi.org/10.4161/AUTO.1.3.2065.

Klein, M. *et al.* (2000) ‘Picornavirus replication inhibitors HBB and guanidine in the echovirus-9 system: The significance of viral protein 2C’, *Journal of General Virology*, 81(4), pp. 895–901. Available at: https://doi.org/10.1099/0022-1317-81-4-895/CITE/REFWORKS.

Kloc, A. *et al.* (2017) ‘Foot-and-mouth disease virus 5’-terminal S fragment is required for replication and modulation of the innate immune response in host cells’, *Virology*, 512, pp. 132–143. Available at: https://doi.org/10.1016/J.VIROL.2017.08.036.

Knoops, K. *et al.* (2008) ‘SARS-Coronavirus Replication Is Supported by a Reticulovesicular Network of Modified Endoplasmic Reticulum’, *PLOS Biology*, 6(9), p. e226. Available at: https://doi.org/10.1371/JOURNAL.PBIO.0060226.

Knox, C. *et al.* (2005) ‘Foot-and-mouth disease virus replication sites form next to the nucleus and close to the Golgi apparatus, but exclude marker proteins associated with host membrane compartments’, *Journal of General Virology*, 86(3), pp. 687–696. Available at: https://doi.org/10.1099/vir.0.80208-0.

Kremer, J.R., Mastronarde, D.N. and McIntosh, J.R. (1996) ‘Computer Visualization of Three-Dimensional Image Data Using IMOD’, *Journal of Structural Biology*, 116(1), pp. 71–76. Available at: https://doi.org/10.1006/JSBI.1996.0013.

Laufman, O., Perrino, J. and Andino, R. (2019) ‘Viral Generated Inter-Organelle Contacts Redirect Lipid Flux for Genome Replication’, *Cell*, 178(2), pp. 275-289.e16. Available at:

https://doi.org/10.1016/J.CELL.2019.05.030/ATTACHMENT/B404D1EC-4BBE-4183-AF77-0383F3498E46/MMC1.PDF.

Lawrence, P. and Rieder, E. (2009) ‘Identification of RNA Helicase A as a New Host Factor in the Replication Cycle of Foot-and-Mouth Disease Virus’, *Journal of Virology*, 83(21), pp. 11356–11366. Available at: https://doi.org/10.1128/JVI.02677-08/SUPPL_FILE/SUP_FIG1_REV072709.ZIP.

Lee, H.W. *et al.* (2022) ‘Foot-and-Mouth Disease Virus 3A Hijacks Sar1 and Sec12 for ER Remodeling in a COPII-Independent Manner’, *Viruses*, 14(4). Available at: https://doi.org/10.3390/V14040839/S1.

Lehtinen, J. *et al.* (2018) ‘Noise2Noise: Learning Image Restoration without Clean Data’, *35th International Conference on Machine Learning, ICML 2018*, 7, pp. 4620–4631. Available at: https://arxiv.org/abs/1803.04189v3 (Accessed: 10 April 2023).

Levin, A. *et al.* (2014) ‘Functional Characterization of Nuclear Localization and Export Signals in Hepatitis C Virus Proteins and Their Role in the Membranous Web’, *PLOS ONE*, 9(12), p. e114629. Available at: https://doi.org/10.1371/JOURNAL.PONE.0114629.

Li, P. *et al.* (2014) ‘Evaluation of a 3A-truncated foot-and-mouth disease virus in pigs for its potential as a marker vaccine.’, *Veterinary research*, 45(1), p. 51. Available at: https://doi.org/10.1186/1297-9716-45-51.

Li, Y. *et al.* (2010) ‘Genetically Engineered, Biarsenically Labeled Influenza Virus Allows Visualization of Viral NS1 Protein in Living Cells’, *Journal of Virology*, 84(14), p. 7204. Available at: https://doi.org/10.1128/JVI.00203-10.

Limpens, R.W.A.L. *et al.* (2011) ‘The Transformation of Enterovirus Replication Structures: a Three-Dimensional Study of Single- and Double-Membrane Compartments’, *mBio*. Edited by M.J. Buchmeier, 2(5). Available at: https://doi.org/10.1128/mBio.00166-11.

van der Linden, L., Wolthers, K.C. and van Kuppeveld, F.J.M. (2015) ‘Replication and Inhibitors of Enteroviruses and Parechoviruses’, *Viruses*, 7(8), p. 4529. Available at: https://doi.org/10.3390/V7082832.

Logan, D. *et al.* (1993) ‘Structure of a major immunogenic site on foot-and-mouth disease virus’, *Nature 1993 362:6420*, 362(6420), pp. 566–568. Available at: https://doi.org/10.1038/362566a0.

Logan, G. *et al.* (2018) ‘Deep Sequencing of Foot-and-Mouth Disease Virus Reveals RNA Sequences Involved in Genome Packaging’, *Journal of Virology*, 92(1). Available at: https://doi.org/10.1128/JVI.01159-17.

López De Quinto, S. *et al.* (2002) ‘IRES-driven translation is stimulated separately by the FMDV 3′-NCR and poly(A) sequences’, *Nucleic Acids Research*, 30(20), pp. 4398–4405. Available at: https://doi.org/10.1093/NAR/GKF569.

Lozano, G. and Martínez-Salas, E. (2015) 'Structural insights into viral IRES-dependent translation mechanisms', *Current Opinion in Virology*, 12, pp. 113–120. Available at: https://doi.org/10.1016/J.COVIRO.2015.04.008.

Mahajan, S. *et al.* (2013) 'Truncated recombinant non-structural protein 2C-based indirect ELISA for FMD sero-surveillance', *Journal of Virological Methods*, 193(2), pp. 405–414. Available at: https://doi.org/10.1016/J.JVIROMET.2013.07.003.

Mahapatra, M. and Parida, S. (2018) 'Foot and mouth disease vaccine strain selection: current approaches and future perspectives', *https://doi.org/10.1080/14760584.2018.1492378*, 17(7), pp. 577–591. Available at: https://doi.org/10.1080/14760584.2018.1492378.

Maier, H.J. *et al.* (2013) 'Infectious Bronchitis Virus Generates Spherules from Zippered Endoplasmic Reticulum Membranes', *mBio*, 4(5). Available at: https://doi.org/10.1128/MBIO.00801-13.

Maier, H.J. *et al.* (2014) 'Spherules and IBV', *Bioengineered*, 5(5), p. 288. Available at: https://doi.org/10.4161/BIOE.29323.

Malik, N. *et al.* (2017) 'Structures of foot and mouth disease virus pentamers: Insight into capsid dissociation and unexpected pentamer reassociation', *PLOS Pathogens*. Edited by Y.J. Tao, 13(9), p. e1006607. Available at: https://doi.org/10.1371/journal.ppat.1006607.

Martín-Acebes, M.A. *et al.* (2010) 'A Single Amino Acid Substitution in the Capsid of Foot-and-Mouth Disease Virus Can Increase Acid Lability and Confer

Resistance to Acid-Dependent Uncoating Inhibition’, *Journal of Virology*, 84(6), pp. 2902–2912. Available at: https://doi.org/10.1128/JVI.02311-09/ASSET/FDD1562D-EE4F-4066-9861-7297DABCE179/ASSETS/GRAPHIC/ZJV9990929940007.JPEG.

Mason, P.W., Bezborodova, S. v. and Henry, T.M. (2002) ‘ Identification and Characterization of a cis -Acting Replication Element (cre) Adjacent to the Internal Ribosome Entry Site of Foot-and-Mouth Disease Virus ’, *Journal of Virology*, 76(19), pp. 9686–9694. Available at: https://doi.org/10.1128/JVI.76.19.9686-9694.2002/ASSET/37F626FA-23D2-4939-BD15-D3BC61BA087B/ASSETS/GRAPHIC/JV1920534008.JPEG.

Mason, P.W., Bezborodova, S. V. and Henry, T.M. (2002) ‘Identification and Characterization of a cis-Acting Replication Element (cre) Adjacent to the Internal Ribosome Entry Site of Foot-and-Mouth Disease Virus’, *Journal of Virology*, 76(19), pp. 9686–9694. Available at: https://doi.org/10.1128/jvi.76.19.9686-9694.2002.

Mason, P.W., Grubman, M.J. and Baxt, B. (2003) ‘Molecular basis of pathogenesis of FMDV’, *Virus Research*, 91(1), pp. 9–32. Available at: https://doi.org/10.1016/S0168-1702(02)00257-5.

Maynell, L.A., Kirkegaard, K. and Klymkowsky2, M.W. (1992) ‘Inhibition of poliovirus RNA synthesis by brefeldin A’, *Journal of Virology*, 66(4), pp. 1985–1994. Available at: https://doi.org/10.1128/JVI.66.4.1985-1994.1992.

Mcknight, K.L. and Lemon, S.M. (1998) ‘The rhinovirus type 14 genome contains an internally located RNA structure that is required for viral replication.’, *RNA*, 4(12), p. 1569. Available at: https://doi.org/10.1017/S1355838298981006.

Melia, C.E. *et al.* (2019) ‘Origins of Enterovirus Replication Organelles Established by Whole-Cell Electron Microscopy’, *mBio*, 10(3), p. 2020. Available at: https://doi.org/10.1128/mbio.00951-19.

Mellor, E.J.C., Brown, F. and Harris, T.J.R. (1985) ‘Analysis of the secondary structure of the poly(C) tract in foot-and-mouth disease virus RNAs’, *Journal of General Virology*, 66(9), pp. 1919–1929. Available at: https://doi.org/10.1099/0022-1317-66-9-1919/CITE/REFWORKS.

Midgley, R. *et al.* (2013) ‘A role for endoplasmic reticulum exit sites in foot-and-mouth disease virus infection’, *Journal of General Virology*, 94(PART 12), pp. 2636–2646. Available at: https://doi.org/10.1099/vir.0.055442-0.

Mielanczyk, L. *et al.* (2014) ‘Closer to the native state. Critical evaluation of cryo-techniques for Transmission Electron Microscopy: preparation of biological samples’, *Folia Histochemica et Cytobiologica*, 52(1), pp. 1–17. Available at: https://doi.org/10.5603/FHC.2014.0001.

Miller, S.T., Hogle, J.M. and Filman, D.J. (2001) ‘Ab initio phasing of high-symmetry macromolecular complexes: successful phasing of authentic poliovirus data to 3.0 Å resolution’, *Journal of Molecular Biology*, 307(2), pp. 499–512. Available at: https://doi.org/10.1006/JMBI.2001.4485.

Miyanari, Y. *et al.* (2007) ‘The lipid droplet is an important organelle for hepatitis C virus production’, *Nature Cell Biology 2007 9:9*, 9(9), pp. 1089–1097. Available at: https://doi.org/10.1038/ncb1631.

Moffat, K. *et al.* (2005a) ‘Effects of Foot-and-Mouth Disease Virus Nonstructural Proteins on the Structure and Function of the Early Secretory Pathway: 2BC but Not 3A Blocks Endoplasmic Reticulum-to-Golgi Transport’, *Journal of Virology*, 79(7), pp. 4382–4395. Available at: https://doi.org/10.1128/JVI.79.7.4382-4395.2005/ASSET/37E27E11-BC3B-4E2D-AE89-21377721CCCF/ASSETS/GRAPHIC/ZJV0070560220009.JPEG.

Moffat, K. *et al.* (2005b) ‘Effects of Foot-and-Mouth Disease Virus Nonstructural Proteins on the Structure and Function of the Early Secretory Pathway: 2BC but Not 3A Blocks Endoplasmic Reticulum-to-Golgi Transport’, *Journal of Virology*, 79(7), pp. 4382–4395. Available at: https://doi.org/10.1128/jvi.79.7.4382-4395.2005.

Moffat, K. *et al.* (2007) ‘Inhibition of the Secretory Pathway by Foot-and-Mouth Disease Virus 2BC Protein Is Reproduced by Coexpression of 2B with 2C, and the Site of Inhibition Is Determined by the Subcellular Location of 2C’, *Journal of Virology*, 81(3), pp. 1129–1139. Available at: https://doi.org/10.1128/jvi.00393-06.

Monaghan, P. *et al.* (2004) ‘The ultrastructure of the developing replication site in foot-and-mouth disease virus-infected BHK-38 cells’, *Journal of General Virology*, 85(4), pp. 933–946. Available at: https://doi.org/10.1099/vir.0.19408-0.

Morphew, M.K. *et al.* (2015) ‘Metallothionein as a clonable tag for protein localization by electron microscopy of cells’, *Journal of microscopy*, 260(1), p. 20. Available at: https://doi.org/10.1111/JMI.12262.

Nayak, A. *et al.* (2006) ‘Role of RNA structure and RNA binding activity of foot-and-mouth disease virus 3C protein in VPg uridylylation and virus replication.’, *Journal of virology*, 80(19), pp. 9865–75. Available at: https://doi.org/10.1128/JVI.00561-06.

Nayak, A., Goodfellow, I.G. and Belsham, G.J. (2005) ‘Factors Required for the Uridylylation of the Foot-and-Mouth Disease Virus 3B1, 3B2, and 3B3 Peptides by the RNA-Dependent RNA Polymerase (3Dpol) In Vitro’, *Journal of Virology*, 79(12), p. 7698. Available at: https://doi.org/10.1128/JVI.79.12.7698-7706.2005.

Nettleton, P.F., Davies, M.J. and Rweyemamu, M.M. (1982) ‘Guanidine and heat sensitivity of foot-and-mouth disease virus (FMDV) strains.’, *The Journal of Hygiene*, 89(1), p. 129. Available at: https://doi.org/10.1017/S0022172400070625.

Neufeldt, C.J. *et al.* (2013) ‘Hepatitis C Virus-Induced Cytoplasmic Organelles Use the Nuclear Transport Machinery to Establish an Environment Conducive to Virus Replication’, *PLoS Pathogens*, 9(10). Available at: https://doi.org/10.1371/JOURNAL.PPAT.1003744.

Neufeldt, C.J. *et al.* (2016) ‘The Hepatitis C Virus-Induced Membranous Web and Associated Nuclear Transport Machinery Limit Access of Pattern Recognition Receptors to Viral Replication Sites’, *PLOS Pathogens*, 12(2), p. e1005428. Available at: https://doi.org/10.1371/JOURNAL.PPAT.1005428.

Neufeldt, C.J. and Cortese, M. (2022) ‘Membrane architects: how positive-strand RNA viruses restructure the cell’, *The Journal of general virology*, 103(8), p. 001773. Available at: https://doi.org/10.1099/JGV.0.001773/CITE/REFWORKS.

Newton, S.E. *et al.* (1985) ‘The sequence of foot-and-mouth disease virus RNA to the 5′ side of the poly(C) tract’, *Gene*, 40(2–3), pp. 331–336. Available at: https://doi.org/10.1016/0378-1119(85)90057-5.

Nguyen-Dinh, V. and Herker, E. (2021) ‘Ultrastructural Features of Membranous Replication Organelles Induced by Positive-Stranded RNA Viruses’, *Cells 2021, Vol. 10, Page 2407*, 10(9), p. 2407. Available at: https://doi.org/10.3390/CELLS10092407.

Novoa, R.R. *et al.* (2005) ‘Virus factories: associations of cell organelles for viral replication and morphogenesis’, *Biology of the Cell*, 97(2), p. 147. Available at: https://doi.org/10.1042/BC20040058.

O’Donnell, V. *et al.* (2011) ‘Foot-and-mouth disease virus utilizes an autophagic pathway during viral replication’, *Virology*, 410(1), pp. 142–150. Available at: https://doi.org/10.1016/J.VIROL.2010.10.042.

O’Donnell, V., Larocco, M. and Baxt, B. (2008) ‘Heparan sulfate-binding foot-and-mouth disease virus enters cells via caveola-mediated endocytosis.’, *Journal of virology*, 82(18), pp. 9075–85. Available at: https://doi.org/10.1128/JVI.00732-08.

O’Donnell, V.K. *et al.* (2001) ‘Subcellular Distribution of the Foot-and-Mouth Disease Virus 3A Protein in Cells Infected with Viruses Encoding Wild-Type and Bovine-Attenuated Forms of 3A’, *Virology*, 287(1), pp. 151–162. Available at: https://doi.org/10.1006/VIRO.2001.1035.

Pacheco, J.M. *et al.* (2003) ‘Role of Nonstructural Proteins 3A and 3B in Host Rangeand Pathogenicity of Foot-and-Mouth DiseaseVirus’, *Journal of Virology*, 77(24), pp. 13017–13027. Available at: https://doi.org/10.1128/jvi.77.24.13017-13027.2003.

Parida, S. (2014) ‘Vaccination against foot-and-mouth disease virus: strategies and effectiveness’, *http://dx.doi.org/10.1586/14760584.8.3.347*, 8(3), pp. 347–365. Available at: https://doi.org/10.1586/14760584.8.3.347.

Parsley, T.B., Cornell, C.T. and Semler, B.L. (1999) ‘Modulation of the RNA binding and protein processing activities of poliovirus polypeptide 3CD by the viral RNA polymerase domain’, *Journal of Biological Chemistry*, 274(18), pp. 12867–12876. Available at: https://doi.org/10.1074/jbc.274.18.12867.

Patarroyo, C., Laliberté, J.F. and Zheng, H. (2013) ‘Hijack it, change it: How do plant viruses utilize the host secretory pathway for efficient viral replication and spread?’, *Frontiers in Plant Science*, 3(JAN), p. 308. Available at: https://doi.org/10.3389/FPLS.2012.00308/BIBTEX.

Paul, A. V. *et al.* (2000) ‘Identification of an RNA Hairpin in Poliovirus RNA That Serves as the Primary Template in the In Vitro Uridylylation of VPg’, *Journal of Virology*, 74(22), pp. 10359–10370. Available at: https://doi.org/10.1128/JVI.74.22.10359-10370.2000/ASSET/1A9692C3-2F44-49F0-9F25-21FE245D8168/ASSETS/GRAPHIC/JV2200852009.JPEG.

Penza, V., Russell, S.J. and Schulze, A.J. (2021) ‘The long-lasting enigma of polycytidine (polyC) tract’, *PLOS Pathogens*, 17(8), p. e1009739. Available at: https://doi.org/10.1371/JOURNAL.PPAT.1009739.

Petherick, K.J. *et al.* (2015) ‘Pharmacological Inhibition of ULK1 Kinase Blocks Mammalian Target of Rapamycin (mTOR)-dependent Autophagy’, *The Journal of Biological Chemistry*, 290(18), p. 11376. Available at: https://doi.org/10.1074/JBC.C114.627778.

Pettersen, E.F. *et al.* (2021) ‘UCSF ChimeraX: Structure visualization for researchers, educators, and developers’, *Protein Science*, 30(1), pp. 70–82. Available at: https://doi.org/10.1002/PRO.3943.

Pfister, T. and Wimmer, E. (1999) ‘Characterization of the nucleoside triphosphatase activity of poliovirus protein 2C reveals a mechanism by which guanidine inhibits poliovirus replication’, *Journal of Biological Chemistry*, 274(11), pp. 6992–7001. Available at: https://doi.org/10.1074/jbc.274.11.6992.

Pilipenko, E. v. *et al.* (1989) ‘Conservation of the secondary structure elements of the 5’ untranslated region of cardio- and aphthovirus RNAs’, *Nucleic Acids Research*, 17(14), pp. 5701–5711. Available at: https://doi.org/10.1093/NAR/17.14.5701.

Pincus, S.E. *et al.* (1986) ‘Guanidine-selected mutants of poliovirus: mapping of point mutations to polypeptide 2C’, *Journal of Virology*, 57(2), pp. 638–646. Available at: https://doi.org/10.1128/JVI.57.2.638-646.1986.

Pringle, C.R. (1964) ‘Inhibition of Multiplication of Foot-and-Mouth Disease Virus by Guanidine Hydrochloride’, *Nature*, 204(4962), pp. 1012–1013. Available at: https://doi.org/10.1038/2041012a0.

Prinz, W.A. (2010) ‘Lipid trafficking sans Vesicles: where, why, how?’, *Cell*, 143(6), p. 870. Available at: https://doi.org/10.1016/J.CELL.2010.11.031.

‘Recognition of the Foot and Mouth Disease Status of Members’ (2020). Available at: https://www.woah.org/fileadmin/Home/eng/Animal_Health_in_the_World/docs/pdf/Resolutions/2020/A_RESO7_2020_FMD.pdf (Accessed: 5 April 2023).

Rieder, E. *et al.* (1993) ‘Genetically engineered foot-and-mouth disease viruses with poly(C) tracts of two nucleotides are virulent in mice’, *Journal of Virology*, 67(9), pp. 5139–5145. Available at: https://doi.org/10.1128/JVI.67.9.5139-5145.1993.

Rigort, A. *et al.* (2010) ‘Micromachining tools and correlative approaches for cellular cryo-electron tomography’, *Journal of Structural Biology*, 172(2), pp. 169–179. Available at: https://doi.org/10.1016/J.JSB.2010.02.011.

Rodriguez, L.L. and Grubman, M.J. (2009) ‘Foot and mouth disease virus vaccines’, *Vaccine*. Elsevier Ltd, pp. D90–D94. Available at: https://doi.org/10.1016/j.vaccine.2009.08.039.

Roingeard, P. *et al.* (2022) ‘The double-membrane vesicle (DMV): a virus-induced organelle dedicated to the replication of SARS-CoV-2 and other positive-sense single-stranded RNA viruses', *Cellular and Molecular Life Sciences*, 79, p. 425. Available at: https://doi.org/10.1007/s00018-022-04469-x.

Romei, M.G. and Boxer, S.G. (2019) 'Split Green Fluorescent Proteins: Scope, Limitations, and Outlook', *Annual review of biophysics*, 48, p. 19. Available at: https://doi.org/10.1146/ANNUREV-BIOPHYS-051013-022846.

Romero-Brey, I. *et al.* (2012) 'Three-Dimensional Architecture and Biogenesis of Membrane Structures Associated with Hepatitis C Virus Replication', *PLOS Pathogens*, 8(12), p. e1003056. Available at: https://doi.org/10.1371/JOURNAL.PPAT.1003056.

Romero-Brey, I. and Bartenschlager, R. (2014) 'Membranous Replication Factories Induced by Plus-Strand RNA Viruses', *Viruses 2014, Vol. 6, Pages 2826-2857*, 6(7), pp. 2826–2857. Available at: https://doi.org/10.3390/V6072826.

Romero-Brey, I. and Bartenschlager, R. (2016) 'Endoplasmic Reticulum: The Favorite Intracellular Niche for Viral Replication and Assembly', *Viruses 2016, Vol. 8, Page 160*, 8(6), p. 160. Available at: https://doi.org/10.3390/V8060160.

Rust, R.C. *et al.* (2001) 'Cellular COPII proteins are involved in production of the vesicles that form the poliovirus replication complex', *Journal of virology*, 75(20), pp. 9808–9818. Available at: https://doi.org/10.1128/JVI.75.20.9808-9818.2001.

Rweyemamu, M.M., Terry, G. and Pay, T.W.F. (1979) 'Stability and immunogenicity of empty particles of foot-and-mouth disease virus', *Archives of Virology*, 59(1–2), pp. 69–79. Available at: https://doi.org/10.1007/BF01317896.

Sáiz, M. *et al.* (2001) 'Deletion or substitution of the aphthovirus 3′ NCR abrogates infectivity and virus replication', *Journal of General Virology*, 82(1), pp. 93–101. Available at: https://doi.org/10.1099/0022-1317-82-1-93/CITE/REFWORKS.

Sandoval, I. V and Carrasco, L. (1997) 'Poliovirus infection and expression of the poliovirus protein 2B provoke the disassembly of the Golgi complex, the organelle target for the antipoliovirus drug Ro-090179', *Journal of Virology*, 71(6), pp. 4679–4693. Available at: https://doi.org/10.1128/JVI.71.6.4679-4693.1997.

Sangar, D. v *et al.* (1987) 'All foot and mouth disease virus serotypes initiate protein synthesis at two separate AUGs', *Nucleic Acids Research*, 15.

Saunders, K. and King, A.M.Q. (1982) 'Guanidine-resistant mutants of aphthovirus induce the synthesis of an altered nonstructural polypeptide, P34.', *Journal of Virology*, 42(2), p. 389. Available at: https://doi.org/10.1128/JVI.42.2.389-394.1982.

Schaar, H.M. van der *et al.* (2016a) 'Illuminating the Sites of Enterovirus Replication in Living Cells by Using a Split-GFP-Tagged Viral Protein', *mSphere*, 1(4). Available at: https://doi.org/10.1128/MSPHERE.00104-16.

Schaar, H.M. van der *et al.* (2016b) 'Illuminating the Sites of Enterovirus Replication in Living Cells by Using a Split-GFP-Tagged Viral Protein', *mSphere*, 1(4), pp. 104–120. Available at: https://doi.org/10.1128/MSPHERE.00104-16.

Scheres, S.H.W. (2012a) 'A Bayesian View on Cryo-EM Structure Determination', *Journal of Molecular Biology*, 415(2), pp. 406–418. Available at: https://doi.org/10.1016/J.JMB.2011.11.010.

Scheres, S.H.W. (2012b) ‘RELION: Implementation of a Bayesian approach to cryo-EM structure determination’, *Journal of Structural Biology*, 180(3), pp. 519–530. Available at: https://doi.org/10.1016/J.JSB.2012.09.006.

Schultz, R.L. and Karlsson, U. (1965) ‘Fixation of the central nervous system for electron microscopy by aldehyde perfusion: II. Effect of osmolarity, pH of perfusate, and fixative concentration’, *Journal of Ultrastructure Research*, 12(1–2), pp. 187–206. Available at: https://doi.org/10.1016/S0022-5320(65)80015-6.

Seago, J. *et al.* (2013) ‘An infectious recombinant foot-and-mouth disease virus expressing a fluorescent marker protein’, *The Journal of General Virology*, 94(Pt 7), p. 1517. Available at: https://doi.org/10.1099/VIR.0.052308-0.

Serrano, P. *et al.* (2006) ‘The 3′ end of the foot-and-mouth disease virus genome establishes two distinct long-range RNA-RNA interactions with the 5′ and region’, *Journal of General Virology*, 87(10), pp. 3013–3022. Available at: https://doi.org/10.1099/VIR.0.82059-0/CITE/REFWORKS.

Shah, P.N.M. *et al.* (2020) ‘Cryo-EM structures reveal two distinct conformational states in a picornavirus cell entry intermediate’, *PLOS Pathogens*, 16(9), p. e1008920. Available at: https://doi.org/10.1371/JOURNAL.PPAT.1008920.

Shakeel, S. *et al.* (2017) ‘Genomic RNA folding mediates assembly of human parechovirus’, *Nature Communications 2017 8:1*, 8(1), pp. 1–11. Available at: https://doi.org/10.1038/s41467-016-0011-z.

Shatkin, A.J. (1985) ‘mRNA cap binding proteins: essential factors for initiating translation’, *Cell*, 40(2), pp. 223–224. Available at: https://doi.org/10.1016/0092-8674(85)90132-1.

Shavinskaya, A. *et al.* (2007) ‘The lipid droplet binding domain of hepatitis C virus core protein is a major determinant for efficient virus assembly’, *Journal of Biological Chemistry*, 282(51), pp. 37158–37169. Available at: https://doi.org/10.1074/jbc.M707329200.

SHIMOMURA, O., JOHNSON, F.H. and SAIGA, Y. (1962) ‘Extraction, Purification and Properties of Aequorin, a Bioluminescent Protein from the Luminous Hydromedusan, Aequorea’, *Journal of Cellular and Comparative Physiology*, 59(3), pp. 223–239. Available at: https://doi.org/10.1002/JCP.1030590302.

Shingler, K.L. *et al.* (2013) ‘The Enterovirus 71 A-particle Forms a Gateway to Allow Genome Release: A CryoEM Study of Picornavirus Uncoating’, *PLOS Pathogens*, 9(3), p. e1003240. Available at: https://doi.org/10.1371/JOURNAL.PPAT.1003240.

Singh, G. *et al.* (2020) ‘The mRNA encoding the JUND tumor suppressor detains nuclear RNA-binding proteins to assemble polysomes that are unaffected by mTOR’, *Journal of Biological Chemistry*, 295(22), pp. 7763–7773. Available at: https://doi.org/10.1074/JBC.RA119.012005/ATTACHMENT/C52C3110-8B64-47D5-8AEB-F311CF9FC1FF/MMC1.ZIP.

Snijder, E.J. *et al.* (2020) 'A unifying structural and functional model of the coronavirus replication organelle: Tracking down RNA synthesis', *PLOS Biology*, 18(6), p. e3000715. Available at: https://doi.org/10.1371/JOURNAL.PBIO.3000715.

Solomon, M.J. and Varshavsky, A. (1985) 'Formaldehyde-mediated DNA-protein crosslinking: a probe for in vivo chromatin structures.', *Proceedings of the National Academy of Sciences of the United States of America*, 82(19), p. 6470. Available at: https://doi.org/10.1073/PNAS.82.19.6470.

Stanway, G. (1990) 'Structure, function and evolutiion of picornaviruses', *Journal of General Virology*, 71(11), pp. 2483–2501. Available at: https://doi.org/10.1099/0022-1317-71-11-2483/CITE/REFWORKS.

Stephens, D.J. *et al.* (2000) 'COPI-coated ER-to-Golgi transport complexes segregate from COPII in close proximity to ER exit sites', *Journal of Cell Science*, 113(12), pp. 2177–2185. Available at: https://doi.org/10.1242/JCS.113.12.2177.

Stockley, P.G. *et al.* (2013) 'Packaging signals in single-stranded RNA viruses: Nature's alternative to a purely electrostatic assembly mechanism', *Journal of Biological Physics*, 39(2), pp. 277–287. Available at: https://doi.org/10.1007/S10867-013-9313-0/FIGURES/3.

Suhy, D.A., Giddings, T.H. and Kirkegaard, K. (2000) 'Remodeling the Endoplasmic Reticulum by Poliovirus Infection and by Individual Viral Proteins: an Autophagy-Like Origin for Virus-Induced Vesicles', *Journal of Virology*, 74(19), pp. 8953–8965. Available at: https://doi.org/10.1128/JVI.74.19.8953-

8965.2000/ASSET/A85EE4D3-745F-4FC2-9B34-D2C0A08ABC6E/ASSETS/GRAPHIC/JV1900793009.JPEG.

Sun, P. *et al.* (2018) ‘Foot-and-mouth disease virus capsid protein VP2 activates the cellular EIF2S1-ATF4 pathway and induces autophagy via HSPB1’, *Autophagy*, 14(2), pp. 336–346. Available at: https://doi.org/10.1080/15548627.2017.1405187.

Sweeney, T.R. *et al.* (2010) ‘Foot-and-mouth disease virus 2C is a hexameric AAA+ protein with a coordinated ATP hydrolysis mechanism’, *Journal of Biological Chemistry*, 285(32), pp. 24347–24359. Available at: https://doi.org/10.1074/jbc.M110.129940.

Szul, T. and Sztul, E. (2011) ‘COPII and COPI traffic at the ER-Golgi interface’, *Physiology*, 26(5), pp. 348–364. Available at: https://doi.org/10.1152/PHYSIOL.00017.2011/ASSET/IMAGES/LARGE/PHY0051100850003.JPEG.

Tang, G. *et al.* (2007) ‘EMAN2: An extensible image processing suite for electron microscopy’, *Journal of Structural Biology*, 157(1), pp. 38–46. Available at: https://doi.org/10.1016/J.JSB.2006.05.009.

Tanida, I., Ueno, T. and Kominami, E. (2008) ‘LC3 and autophagy’, *Methods in Molecular Biology*, 445, pp. 77–88. Available at: https://doi.org/10.1007/978-1-59745-157-4_4/FIGURES/4_3_978-1-59745-157-4.

Tao, Y.J. and Ye, Q. (2010) ‘RNA Virus Replication Complexes’, *PLOS PATHOGENS*, 6(7). Available at: https://doi.org/10.1371/journal.ppat.1000943.

Taylor, M.P. and Kirkegaard, K. (2007) ‘Modification of Cellular Autophagy Protein LC3 by Poliovirus’, *Journal of Virology*, 81(22), p. 12543. Available at: https://doi.org/10.1128/JVI.00755-07.

Tegunov, D. *et al.* (2020) ‘Multi-particle cryo-EM refinement with M visualizes ribosome-antibiotic complex at 3.7 Å inside cells’, *bioRxiv*, p. 2020.06.05.136341. Available at: https://doi.org/10.1101/2020.06.05.136341.

Tegunov, D. and Cramer, P. (2019) ‘Real-time cryo-electron microscopy data preprocessing with Warp’, *Nature Methods 2019 16:11*, 16(11), pp. 1146–1152. Available at: https://doi.org/10.1038/s41592-019-0580-y.

Trahey, M. *et al.* (2012) ‘Poliovirus infection transiently increases COPII vesicle budding.’, *Journal of virology*, 86(18), pp. 9675–82. Available at: https://doi.org/10.1128/JVI.01159-12.

Tsien, R.Y. (1998) ‘THE GREEN FLUORESCENT PROTEIN’, *Annu. Rev. Biochem*, 67, pp. 509–553. Available at: www.annualreviews.org (Accessed: 9 October 2022).

Tuthill, T.J. *et al.* (2009) ‘Equine rhinitis A virus and its low pH empty particle: clues towards an aphthovirus entry mechanism?’, *PLoS pathogens*, 5(10). Available at: https://doi.org/10.1371/journal.ppat.1000620.

Tuthill, T.J. *et al.* (2010) ‘Picornaviruses’, pp. 43–89. Available at: https://doi.org/10.1007/82_2010_37.

Vázquez-Calvo, A. *et al.* (2014) ‘An Increase in Acid Resistance of Foot-and-Mouth Disease Virus Capsid Is Mediated by a Tyrosine Replacement of the VP2 Histidine

Previously Associated with VP0 Cleavage', *Journal of Virology*, 88(5), pp. 3039–3042. Available at: https://doi.org/10.1128/JVI.03222-13/ASSET/440DED23-DAD2-4AC5-BD44-0A6CB4694354/ASSETS/GRAPHIC/ZJV9990987140003.JPEG.

Wang, L. *et al.* (2017) 'HCV-induced autophagosomes are generated via homotypic fusion of phagophores that mediate HCV RNA replication', *PLOS Pathogens*, 13(9), p. e1006609. Available at: https://doi.org/10.1371/JOURNAL.PPAT.1006609.

Ward, J.C. *et al.* (2022) 'The RNA pseudoknots in foot-and-mouth disease virus are dispensable for genome replication, but essential for the production of infectious virus', *PLOS Pathogens*, 18(6), p. e1010589. Available at: https://doi.org/10.1371/JOURNAL.PPAT.1010589.

Weissenberger, G., Henderikx, R.J.M. and Peters, P.J. (2021) 'Understanding the invisible hands of sample preparation for cryo-EM', *Nature Methods 2021 18:5*, 18(5), pp. 463–471. Available at: https://doi.org/10.1038/s41592-021-01130-6.

WOAH - World Organisation for Animal Health (no date). Available at: https://www.woah.org/en/home/ (Accessed: 5 April 2023).

Wolff, G. *et al.* (2020) 'Double-Membrane Vesicles as Platforms for Viral Replication', *Trends in Microbiology*, 28(12), pp. 1022–1033. Available at: https://doi.org/10.1016/J.TIM.2020.05.009.

Wu, J. *et al.* (2021) 'Sec62 Regulates Endoplasmic Reticulum Stress and Autophagy Balance to Affect Foot-and-Mouth Disease Virus Replication', *Frontiers* *in Cellular and Infection Microbiology*, 11, p. 796. Available at: https://doi.org/10.3389/FCIMB.2021.707107/BIBTEX.

Wutz, G. *et al.* (1996) ‘Equine rhinovirus serotypes 1 and 2: Relationship to each other and to aphthoviruses and cardioviruses’, *Journal of General Virology*, 77(8), pp. 1719–1730. Available at: https://doi.org/10.1099/0022-1317-77-8-1719/CITE/REFWORKS.

Yang, W. *et al.* (2020) ‘Foot-and-Mouth Disease Virus 3A Protein Causes Upregulation of Autophagy-Related Protein LRRC25 To Inhibit the G3BP1-Mediated RIG-Like Helicase-Signaling Pathway’, *Journal of Virology*, 94(8). Available at: https://doi.org/10.1128/JVI.02086-19/ASSET/6622C1F1-CBC1-4353-ABFE-48727DF0AE96/ASSETS/GRAPHIC/JVI.02086-19-F0010.JPEG.

Yang, X. *et al.* (2022) ‘Enterovirus A71 utilizes host cell lipid β-oxidation to promote its replication’, *Frontiers in Microbiology*, 13, p. 3804. Available at: https://doi.org/10.3389/FMICB.2022.961942/BIBTEX.

Ypma-Wong, M.F. *et al.* (1988) ‘Protein 3CD is the major poliovirus proteinase responsible for cleavage of the p1 capsid precursor’, *Virology*, 166(1), pp. 265–270. Available at: https://doi.org/10.1016/0042-6822(88)90172-9.

Zhang, C. *et al.* (2022) ‘An anti-picornaviral strategy based on the crystal structure of foot-and-mouth disease virus 2C protein’, *Cell Reports*, 40(1), p. 111030. Available at: https://doi.org/10.1016/J.CELREP.2022.111030.

Zhang, P. (2019) ‘Advances in cryo-electron tomography and subtomogram averaging and classification’, *Current Opinion in Structural Biology*, 58, pp. 249–258. Available at: https://doi.org/10.1016/J.SBI.2019.05.021.

Zhang, X. *et al.* (2020) ‘Foot-and-Mouth Disease Virus 3B Protein Interacts with Pattern Recognition Receptor RIG-I to Block RIG-I–Mediated Immune Signaling and Inhibit Host Antiviral Response’, *The Journal of Immunology*, 205(8), pp. 2207–2221. Available at: https://doi.org/10.4049/JIMMUNOL.1901333/-/DCSUPPLEMENTAL.

Zhu, L. *et al.* (2015) ‘Structure of Ljungan virus provides insight into genome packaging of this picornavirus’, *Nature Communications 2015 6:1*, 6(1), pp. 1–9. Available at: https://doi.org/10.1038/ncomms9316.

Zhu, Z. *et al.* (2019) ‘The Pseudoknot Region of the 5′ Untranslated Region Is a Determinant of Viral Tropism and Virulence of Foot-and-Mouth Disease Virus’, *Journal of Virology*, 93(8), pp. 2039–2057. Available at: https://doi.org/10.1128/JVI.02039-18/ASSET/45650B25-1FEF-4F83-B7A3-AED798467F6B/ASSETS/GRAPHIC/JVI.02039-18-F006B.JPEG.

Zibert, A. *et al.* (1990) ‘Infectious foot-and-mouth disease virus derived from a cloned full-length cDNA.’, *Journal of Virology*, 64(6), p. 2467. Available at: https://doi.org/10.1128/JVI.64.6.2467-2473.1990.

Zivanov, J. *et al.* (2018) ‘New tools for automated high-resolution cryo-EM structure determination in RELION-3’, *eLife*, 7. Available at: https://doi.org/10.7554/ELIFE.42166.

Chapter 8 Appendix

Table 8.1 Tomograms used for reconstructing 3D model of intracellular ERAV

Session number	Tomogram	Cell type	Time post infection (hr)	Number of virus particles
NT26538-22	Tomo_G3_03	Vero	11hpi	112
NT26538-40	Tomo_G2_14		9hpi	109
NT26538-53	grid2602_1_lam2a_ts_004		11hpi	50
	grid2602_1_lam2a_ts_006			4
	grid2602_1_lam2a_ts_008			1
	grid6201_1_lam2_ts_002			29
	grid6201_1_lam2_ts_003			6
	grid6201_1_lam2_ts_006			3
	grid6201_1_lam2_ts_008			5
	grid6201_1_lam2_ts_009			48
	grid6201_1_lam2_ts_010			7
	grid6201_1_lam6a_ts_004			2
	grid6202_1_lam1a_ts_002			8
	grid6202_1_lam1a_ts_003			3

Movie 1: Soft X-ray tomogram of uninfected Vero.

Movie 2: Soft X-ray tomograms ERAV infected Vero cell fixed at 11hpi.

Movie 3: ERAV infected Vero cell fixed at 9hpi.

Movie 4: ERAV infected Vero cell fixed at 11hpi.

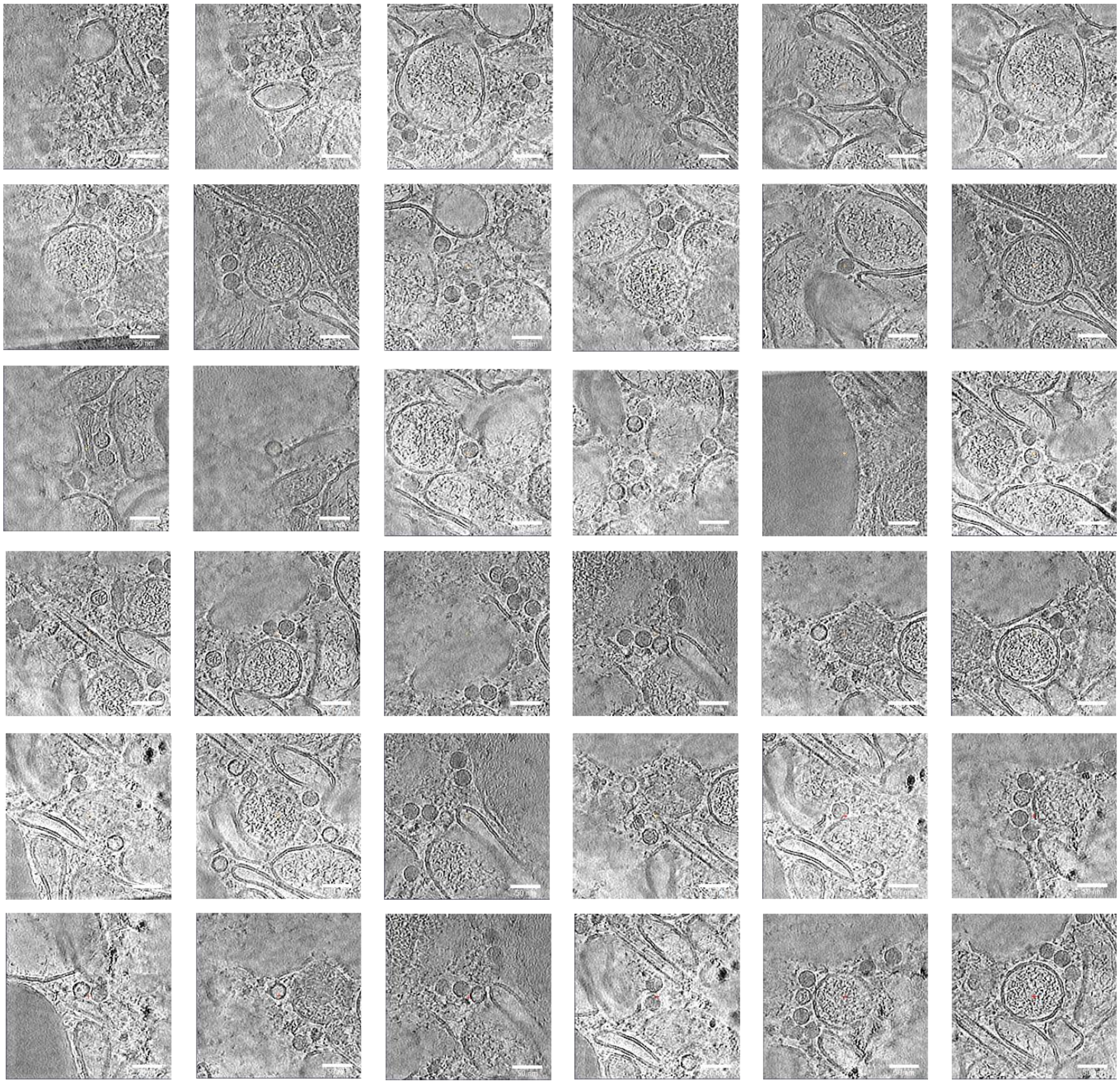

Figure 8.7.1 A gallery of virus tethered to membrane structures at 9 hours post ERAV infection. (All scale bar = 50 µm)

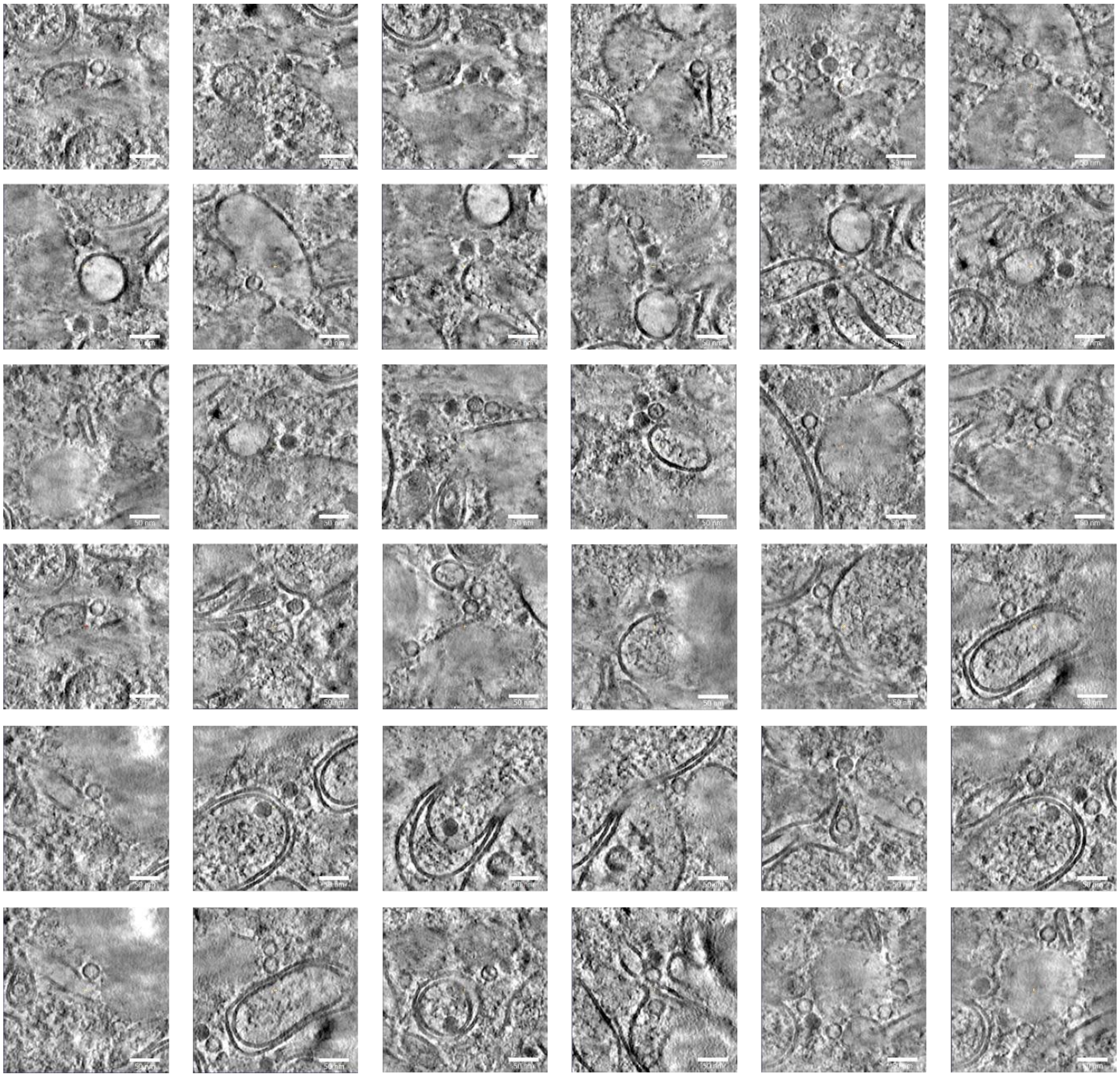

Figure 8.7.2 A gallery of examples of virus particles tethered to membrane structure at 11 hours post ERAV infection. (All scale bar = 50 µm)

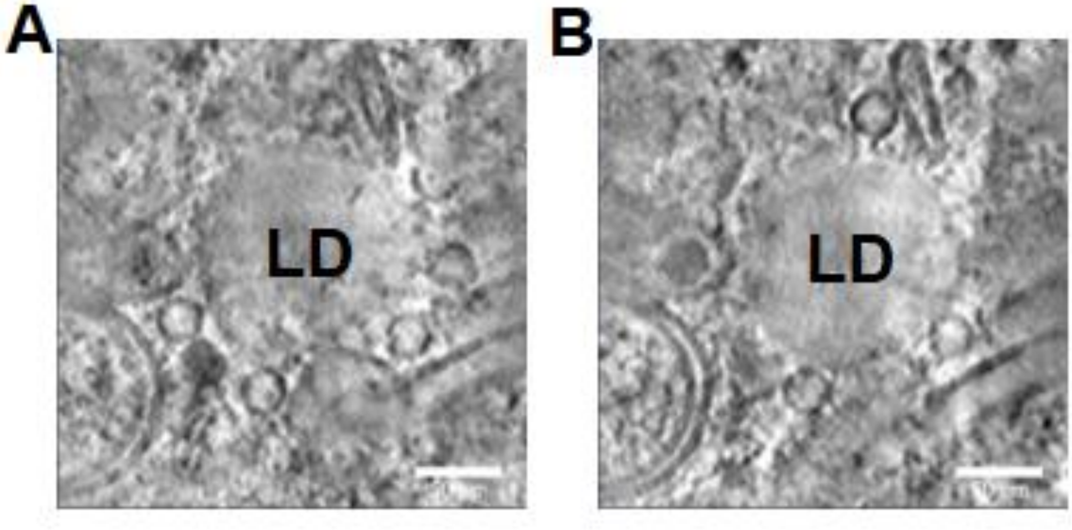

Figure 8.7.3 An example of virus particles tethered to a lipid droplet.

Both A and B panels showed the same lipid droplet (LD) at different Z-height. This lipid droplet was surrounded by viruses and some viruses showed that they are tethered to the LD. (Scale bar = 50 μm)

		Tomogram ID (Session number_Tomogram name)	Distance (angstrom)	
Empty	Min	NT26538-40_G2_14	100.957	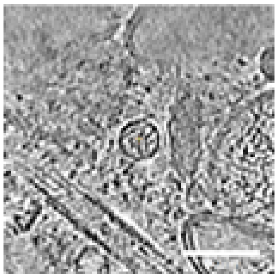
	Max	NT26538-53_G3_03	513.955	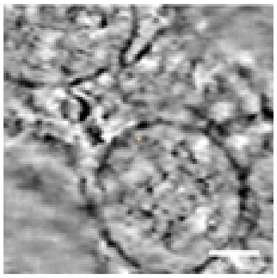
Full	Min	NT26538-40_G2_14	130.632	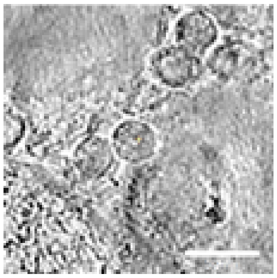
	Max	NT26538-53_G3_03	902.106	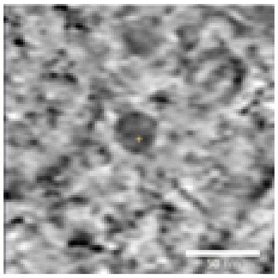

Figure 8.7.4 Minimum and maximum distances between ERAV full and empty particle and membrane structure from pooled particles analysis.

This figure shows a table recording the minimum and maximum distances and the relevant information such as session number and the tomogram name). (All scale bar = 50 μm)